

# **Thermal Control of Photovoltaic Panels under Desert Climates**

**Mayameen Naser Reda**

Vollständiger Abdruck der von der TUM School of Engineering and Design der Technischen Universität München zur Erlangung des akademischen Grades einer  
Doktorin der Ingenieurwissenschaften (Dr.-Ing.)  
genehmigten Dissertation.

Vorsitz:

Prof. Dr.-Ing. Katrin Wudy

Prüfer der Dissertation:

1. Prof. Dr.-Ing. Thomas Sattelmayer
2. Prof. Dr.-Ing. Hussain H. Al-Kayiem

Die Dissertation wurde am 20.02.2023 bei der Technischen Universität München eingereicht und durch die TUM School of Engineering and Design am 30.05.2023 angenommen.



---

## Acknowledgements

This work was done at Chair of Thermodynamics at the Technical University of Munich, TUM.

After thanking God, I would like to thank my country (Iraq) and Germany especially my university (TUM) who made this work possible.

Special thanks to Prof. Dr. Sattelmayer for the scientific supervision of my thesis. My special thanks also go to Prof. Dr. Al-Kayiem for being the second examiner and to Prof. Dr. Wudy for being the chairwoman of the examination. Many thanks also to Dr. Markus Spinnler for being my mentor with the scientific and writing work.

A special thanks to my colleagues at the Institute of Thermodynamics who have helped me with proofread or to me professionally advised. First, I want to thank Alexander Präps who encouraged me and supported me with his advice and scientific discussion to overcome the difficulties of my first months at the institute. Special thanks also to Mrs. Helga Bassett for the administrative and moral support, Dr. Nancy King, Florian Kiefer, Andreas Kastl and Bernd Heitorst. I would like also to thank all colleagues at the workshop especially Thomas Schleussner. Outside the institute, I would like to thank Dr. Rajib Mahamud for the contribution and scientific discussion of one of our publications.

I am especially grateful to my father, my mother and my close siblings and friends. Finally, I am grateful for the unconditional love and support that my husband Ali has shown me in the last months, which made the last phase of my thesis easier. I dedicate this work to all of you.

July 2023

Mayameen Reda

# Abstract

Photovoltaic (PV) panels are a promising technology to harness renewable energy using solar irradiation. PV power plants are more useful in regions with high solar irradiation, which mostly have arid and desert environments.

However, the performance of PV panels deteriorates primarily due to two problems. The first problem is high diurnal PV cell temperature. High PV cell temperatures have a negative impact on both the performance and durability of the PV panels. The second problem is nocturnal condensation (dew formation). Dew formation causes an accumulation of soil dust from the surrounding environment. Thus, mud is easily formed on the PV panels. Both dust accumulation and mud formation reduce the transparency of the PV panels' glass cover and further reduce the PV cell efficiency.

In the present study, a classical PV panel with a rear water pocket (PV/T) is integrated with a ground soil heat exchanger (GSHEX). The PV/T-GSHEX system is proposed as a collective solution to mitigate both problems by balancing the diurnal and nocturnal loads. The GSHEX allows to cool the PV panels during the day and heats them above the dew point temperature during the night. To investigate the increased efficiency potential of the proposed solution under real climatic conditions at different locations, a mathematical model for the PV/T-GSHEX system with an accuracy of  $> 96\%$  was developed. The model was applied to two locations (Qatar and Malaysia). It was shown that the proposed system is able to reduce the diurnal PV cell temperature by about 10 K and to keep nocturnal temperature above the dew point by about 2-5 K. This contributed to a 10% - 11% improvement in the system performance.

---

## Zusammenfassung

Photovoltaik(PV)-Module sind eine weit verbreitete Technologie zur Nutzung von Solarenergie. Besonders sinnvoll ist der Einsatz von PV-Anlagen in ariden, wüstenartigen Regionen mit hoher solarer Einstrahlung. Gerade in diesen Regionen unterliegt die Leistung von PV-Modulen jedoch zweierlei Einschränkungen.

Die erste Einschränkung entsteht tagsüber durch die hohe Temperatur der PV-Zellen. Hohe Zelltemperaturen haben negative Auswirkungen sowohl auf die Leistung als auch auf die Haltbarkeit der PV-Module. Die zweite Einschränkung entsteht durch nächtliche Kondensation bzw. Taubildung. Taubildung begünstigt die Anlagerung von Staub aus der Umgebung und kann sehr schnell zur Bildung einer Schlammschicht auf den PV-Modulen führen. Sowohl die Staubansammlung als auch die Schlammabildung verringern die Transparenz der Glasabdeckung der PV-Module und reduzieren somit deren Effizienz.

In der vorliegenden Arbeit wird ein konventionelles PV-Modul mit einem rückseitigen, wassergeführten Wärmetauscher (PV/T) und einem Erdregister (GSHEX) ausgestattet. Durch Ausgleich der tagsüber und nachts entstehenden Wärmelasten kann das PV/T-GSHEX-System somit beide Probleme abmildern. Das GSHEX ermöglicht es, die PV-Module tagsüber zu kühlen und nachts auf Temperaturen oberhalb des Taupunktes zu heizen. Um das Effizienzpotenzial der vorgeschlagenen Lösung unter realen Klimabedingungen an verschiedenen Standorten zu untersuchen, wurde ein mathematisches Modell für das PV/T-GSHEX-System mit einer Genauigkeit von  $> 96\%$  entwickelt. Das Modell wurde beispielhaft für zwei Standorte in Katar und in Malaysia angewendet. Es konnte gezeigt werden, dass das vorgeschlagene System in der Lage ist, tagsüber die Temperatur der PV-Zellen um bis zu 10 K zu senken und nachts die Temperatur um 2–5 K über dem Taupunkt zu halten. Dies resultiert in einer Steigerung der Systemleistung um etwa 10 %.

# Contents

<b>Abstract</b>	<b>ii</b>
<b>List of Figures</b>	<b>vi</b>
<b>List of Tables</b>	<b>x</b>
<b>1 Introduction</b>	<b>1</b>
1.1 Problem-Solving Approach . . . . .	5
1.2 Motivation . . . . .	7
1.2.1 PV Cell Efficiency Reduction Due to High Temperatures . . . . .	7
1.2.2 Condensation and Mud Formation . . . . .	10
1.2.3 PV Cleaning Methods . . . . .	15
1.3 Established PV Thermal Management Strategies . . . . .	16
1.3.1 Diurnal Cooling of the PV Modules . . . . .	16
1.3.2 The GSHEX System . . . . .	18
1.4 Study Objectives and Research Approach . . . . .	19
1.5 Thesis Overview . . . . .	21
<b>2 Experimental Investigation of the PV/T-GSHEX System</b>	<b>23</b>
2.1 Outdoor Experiment . . . . .	23
2.1.1 Experimental Setup . . . . .	23
2.1.2 Measurement Equipment . . . . .	27
2.1.3 Experimentation Environment . . . . .	28
2.2 Experimental Results . . . . .	28
2.2.1 Experiment Verification Test . . . . .	28
2.2.2 PV and PV/T Surface Temperatures . . . . .	30
2.2.3 Electrical Efficiency of PV and PV/T Panel . . . . .	31

---

2.2.4	GSHEX Results . . . . .	31
2.3	Summary . . . . .	33
<b>3</b>	<b>Analysis of the Soil Temperature Distribution</b>	<b>35</b>
3.1	Mathematical Modeling . . . . .	36
3.2	Experimental Validation . . . . .	41
3.2.1	Experimental Setup . . . . .	41
3.2.2	Model Validation . . . . .	43
3.3	Application of the Model . . . . .	44
3.3.1	Case Study 1: Tropical Climate (Malaysia) . . . . .	44
3.3.2	Case Study 2: Semi-desert Climate (Qatar) . . . . .	47
3.4	Advantages of the Model . . . . .	50
3.5	Summary . . . . .	51
<b>4</b>	<b>Modeling of the PV/T-GSHEX System</b>	<b>53</b>
4.1	Development of the Mathematical Model . . . . .	53
4.2	Modeling of the PV/T System: . . . . .	56
4.3	Ground Soil Heat Exchanger (GSHEX) . . . . .	59
4.4	Results and Discussion . . . . .	60
4.4.1	Validation of the PV/T-GSHEX Model . . . . .	60
4.4.2	Weather Scenarios with Dew Formation Propensity . . . . .	62
4.4.3	Annual Prediction of PV and PV/T Temperatures . . . . .	63
4.4.4	PV Performance Enhancement . . . . .	64
4.4.5	Meteorological Parameter Analysis . . . . .	65
4.5	Summary . . . . .	70
<b>5</b>	<b>Experimental and Theoretical Investigations on Condensation</b>	<b>71</b>
5.1	Experimental Investigation . . . . .	71
5.2	Mathematical Analysis . . . . .	75
5.2.1	Droplet Growth Under Free Convection . . . . .	75
5.2.2	Droplet Growth Under Forced Convection . . . . .	78
5.3	Results and Discussion . . . . .	81
5.4	Summary . . . . .	93
<b>6</b>	<b>Conclusions and Outlook</b>	<b>94</b>
6.1	Conclusions . . . . .	94

6.1.1	Experimental Studies . . . . .	94
6.1.2	Theoretical Modeling of the Soil Temperature Distribution	95
6.1.3	Numerical Simulation . . . . .	96
6.1.4	Parameters Influencing Dew Formation . . . . .	96
6.2	Outlook . . . . .	97
	<b>Bibliography</b>	<b>99</b>
	<b>A Appendix</b>	<b>117</b>

# List of Figures

1.1	Annual weather data for Qatar (a) air and dew point temperature as well as (b) irradiation flux. . . . .	2
1.2	Dust blowing across the Arabian Sea and the Middle East regions [9]. . . . .	3
1.3	Problem description and solution strategy. . . . .	4
1.4	Operational principle of the proposed system with the main heat transfer phenomena (a) diurnal cooling, and (b) nocturnal heating. . . . .	6
1.5	PV Panels in a solar power plant in Qatar [15]. Mud formation can be observed in the center and right photograph. . . . .	7
1.6	Temperature effect on the $I$ - $V$ characteristics of the PV cell [33].	9
1.7	Accumulated effect of dust deposition on PV performance under different weather conditions and inclination angles [26]. . . . .	11
1.8	Dust adhesion on PV panels due to dew formation and exposure to dusty winds [42]. . . . .	12
1.9	Transmittance of the as-received glass, glass after dry mud removal, and glass with the dried solution [28]. . . . .	13
1.10	A detailed description of the proposed research approach. . . . .	20
2.1	Schematic diagram of the PV-GSHEX system (left) and the system during the installation stage (right). . . . .	24
2.2	Rear cooling water pocket. . . . .	25
2.3	The GSHEX during the installation. . . . .	26
2.4	Measurement data of the condensation period (a) and photos of the dry PV/T surface and condensation on the PV surface (b) at the same time, 7:30 AM. . . . .	29

2.5	Measurement of the ambient, PV surface (PV), PV/T surface (PV/T), and dew point temperature and solar irradiation. . . . .	30
2.6	Comparison of the electrical efficiency of the PV/T-GSHEX system and the conventional PV system. . . . .	31
2.7	Heat storage for dry and wet soil, water volumetric flow rate 1.6 l/min. . . . .	33
3.1	Power balance on the soil surface. . . . .	36
3.2	Schematic experimental setup (left) and photo for the soil cylinder and the arrangement of the sensors in the experiment (right). . . . .	41
3.3	Results for long term heating and cooling experiments. . . . .	42
3.4	Comparison between experimental and simulation results after (a) 1.1 h and (b) 2.1 h test duration. . . . .	43
3.5	Meteorological data for Malaysia, (a) air and dew point temperatures, (b) solar irradiation flux in hourly values. . . . .	44
3.6	Annual STD at 0.01 m and 1 m depth for soil with high moisture content (24 %) and thermal conductivity 2 W/mK, Malaysia. . . . .	45
3.7	Annual STD at 1 m depth for high (2 W/mK) and low (0.2 W/mK) soil thermal conductivity, Malaysia. . . . .	46
3.8	Meteorological data for Qatar, (a) air and dew point temperatures, (b) solar irradiation flux in hourly values. . . . .	47
3.9	(a) Annual STD at 0.5 m and 2 m depth (b) STD fluctuation for two selected days in August, Qatar. . . . .	48
3.10	Annual STD for Malaysia at 0.5 m and 2 m depths. . . . .	49
3.11	CFD solution for the STD problem. . . . .	50
3.12	Computational time for the GF analytical model in comparison to numerical solutions (ANSYS and COMSOL). . . . .	51
4.1	Layout of the PV/T layers and heat flow through the PV/T-GSHEX system. . . . .	54
4.2	Validation of the PV/T-GSHEX model by comparison of measured and simulated surface temperatures of: (a) daytime and (b) nighttime. . . . .	61
4.3	Hourly simulated conventional PV surface and dew point temperature difference. . . . .	62

LIST OF FIGURES

---

4.4	Annual simulated PV and PV/T surface temperatures for Malaysia.	63
4.5	Annual simulated PV and PV/T surface temperatures for Qatar. .	64
4.6	Simulated PV/T surface temperature for different wind velocities.	66
4.7	Simulated PV/T surface temperature for different ambient temperatures. . . . .	66
4.8	Simulated PV/T surface temperature for soild and clean glass. .	67
4.9	Number of condensation/overheating hours for the annually simulated PV/T surface temperature. . . . .	68
4.10	Annual PV and PV/T-GSHEX average surface temperatures at 1 m and 4 m depth for Qatar. . . . .	69
5.1	Schematic of the test rig and data acquisition system. . . . .	72
5.2	The condensate droplet under airflow conditions subjected to convective heat and mass transfer. . . . .	78
5.3	Microscopic condensation images for clean glass ( $\delta = 0 \mu\text{m}$ ) and free convection ( $u_\infty = 0 \text{ m/s}$ ). . . . .	82
5.4	Microscopic condensation images for clean glass ( $\delta = 0 \mu\text{m}$ ) and forced convection ( $u_\infty = 8.58 \text{ m/s}$ ). . . . .	83
5.5	Microscopic condensation images for glass with dust layer thickness ( $\delta = 30 \mu\text{m}$ ) under forced convection ( $u_\infty = 8.58 \text{ m/s}$ ). . . .	84
5.6	Microscopic condensation images for glass with dust layer thickness ( $\delta = 56 \mu\text{m}$ ) under forced convection ( $u_\infty = 8.58 \text{ m/s}$ ). . . .	85
5.7	Visual and statistical profile of the experimentally determined droplet distribution patterns and corresponding histograms of droplet frequency at different times for clean glass ( $\delta = 0 \mu\text{m}$ ) and free convection ( $u_\infty = 0 \text{ m/s}$ ). . . . .	87
5.8	Time to detect condensation as a function of (a) $\delta = (0, 30, 56, 80) \mu\text{m}$ and (b) $u_\infty = (0, 1.63, 2.76, 8.58) \text{ m/s}$ . . . . .	88
5.9	Comparison of the experiment results and the model for droplet growth at air velocities (a) 0 m/s, (b) 1.63 m/s and (c) 8.58 m/s. .	89
5.10	Effect of relative humidity on the onset of condensation and droplet growth at airflow velocity 1.6 m/s. . . . .	91
5.11	Experimental data of droplet growth rate for different micro-dust layer thicknesses on the substrate surface, at airflow velocity (a) 1.6 m/s and (b) 8.58 m/s. . . . .	92

A.1 Oven-drying method procedure in UTP/Civil engineering Lab. . 117

# List of Tables

1.1	Overview on PV cleaning methods and their pros and cons. . . .	16
1.2	GSHEX system arrangements with their benefits and drawbacks.	19
2.1	PV module electricity performance parameters at (STC 1000 W/m <sup>2</sup> , AM 1.5 and 25°C). . . . .	25
2.2	Soil properties used in the experiment. . . . .	32
3.1	Soil properties used in the experiment and applied to the model.	43
3.2	Soil properties used in the model, Malaysia. . . . .	45
3.3	Soil properties used in the model. . . . .	48
5.1	Selected boundary conditions for the experimental investigations.	74

# Nomenclature

## Latin Characters

$A$	Area, Constant	$[\text{m}^2], [-]$
$a$	Diode constant	$[-]$
$B$	Constant	$[-]$
$C$	Constant of integration	$[-]$
$C_p$	Heat capacity	$[\text{kJ}/\text{kg K}]$
$d$	Diameter	$[\text{m}]$
$D$	Mass diffusion coefficient (air to droplet)	$[\text{m}^2/\text{s}]$
$D_0$	Mass diffusion coefficient (droplet to air)	$[\text{m}^2/\text{s}]$
$F$	Flow rate factor	$[-]$
$f_T$	Normalization factor for temperature difference	$[-]$
$f_\rho$	Normalization factor for density difference	$[-]$
$G$	Solar global irradiation	$[\text{W}/\text{m}^2]$
$GF$	Green's function	$[\text{m}^{-1}]$
$h$	Convective heat transfer coefficient	$[\text{W}/\text{m}^2 \text{K}]$
$h_m$	Mass transfer coefficient	$[\text{m}/\text{s}]$
$I$	Electric current	$[\text{A}]$
$K$	Heat conduction solution	$[-]$
$k$	Thermal conductivity	$[\text{W}/\text{m K}]$
$L$	Length, Thickness	$[\text{m}]$
$L_c$	Latent heat of condensation	$[\text{kJ}/\text{kg}]$
$m$	Mass	$[\text{kg}]$
$\dot{m}$	Mass flow rate	$[\text{kg}/\text{s}]$
$N$	Number of cells	$[-]$
$n$	Number of elements	$[-]$

$P$	Power	[W]
$p$	Pressure	[Pa]
$\dot{Q}$	Heat flow	[W]
$Q$	Energy	[J]
$\dot{q}$	Heat flux	[W/m <sup>2</sup> ]
$R$	Thermal resistance, Electrical resistance	[K/W],[ $\Omega$ ]
$R$	Ideal gas constant	[J/K mol]
$r$	Radius	[m]
$S$	Ambient-Saturation ratio	[-]
$T$	Temperature	[K],[ $^{\circ}$ C]
$t$	Time	[s]
$U$	Overall heat transfer coefficient	[W/m <sup>2</sup> K]
$u$	Velocity	[m/s]
$V$	Voltage	[V]
$W$	Width, Weight	[m],[kg]
$x$	Position	[m]

## Greek Characters

$\tau$	Transmissivity, Integration factor	[-]
$\infty$	Ambient	
$\alpha$	Thermal diffusivity, Accommodation coefficient	[m <sup>2</sup> /s], [-]
$\alpha_{ab}$	Absorptivity	[-]
$\rho$	Density	[kg/m <sup>3</sup> ]
$\rho_r$	Reflectivity	[-]
$\varepsilon$	Emissivity	[-]
$\nu$	Kinematic viscosity	[m <sup>2</sup> /s]
$\eta$	Efficiency	[%]
$\beta$	Temperature coefficient, Condensation coefficient	[-0.5 %/K],[ -]
$\delta$	Thickness, Dirac delta function	[m],[ -]
$\mu$	Dynamic viscosity	[kg/m s]
$\theta$	Tilt angle	[ $^{\circ}$ ]
$\gamma$	Azimuth angle	[ $^{\circ}$ ]
$\sigma$	Stefan-Boltzmann constant (= $5.67 \times 10^{-8}$ )	[W/m <sup>2</sup> K <sup>4</sup> ]

## Non-Dimensional Numbers

Gr	Grashof number
Nu	Nusselt number
Re	Reynolds number
Sc	Schmidt number
Sh	Sherwood number

## Abbreviations

AM	Air mass
CFD	Computational fluid dynamics
1-D	One dimension
2-D	Two dimensions
EVA	Ethylene vinyl acetate
EPS	Polystyrene insulation
FF	Fill factor
GSHEX	Ground soil heat exchanger
MC	Moisture content
MPP	Maximum power point
NOCT	Nominal operating cell temperature
PV	Photovoltaic
PV/T	Thermally controlled photovoltaic
GS	Ground soil
GF	Green's function
HEX	Heat exchanger
HSC	High speed camera
IR	Infrared
LWrad	Long wave radiation
RH	Relative humidity
STD	Soil temperature distribution
STC	Standard test conditions
SWrad	Short wave radiation

## Subscripts

0	Initial-point, Liquid phase
$\infty$	Ambient
a	Air
Al	Aluminium
avg	Average
bs	Backside
coil	Pipe coil of heat exchanger
cond	Conduction
conv	Convection
dew	Dew point
elc	Electrical
eq	Equivalent
evap	Evaporation
f	Fluid
gain	Thermal gain
glass	Glass
h	Hydraulic
HEX	Heat exchanger
in,out	Inlet, Outlet
i,k	Counter
LWrad	Long wave radiation
MPP	Maximum power point
max, min	Maximum, Minimum
mean	Mean
m	Mass transfer
o	Diode
OC, SC	Open circuit, Short circuit
p	Parallel
PV	Photovoltaic
pvn	Nominal light

r	Droplet
s	Series, Surface, Soil, Substrate
sat	Saturation
sky	Sky
SWrad	Short wave radiation
T	Tedlar
t	Thermal junction, Top
th	Thermal
w	Water
wind	Wind



# 1 Introduction

The application of photovoltaic (PV) panels is a promising technology to harness renewable energy using solar irradiation. PV power plants are more useful in regions with high solar irradiation, which mostly have arid and desert environments. Installing PV panels in these environments faces two major problems. The first and most important problem is high diurnal PV cell temperatures due to high solar irradiation and high ambient temperatures. High PV cell temperatures have a negative impact on both performance and durability of the PV panels [1, 2]. The second problem is the nocturnal condensation of air humidity on the panels or in other terms dew formation. Dew formation causes an accumulation of soil dust from the surrounding environment [127]. Thus, mud is easily formed on the PV panels. Both dust accumulation and mud formation reduce the transparency of the PV panels' glass cover and further reduce the PV cell efficiency [3, 4]. Besides, the maintenance cost is increasing due to cleaning requirements [3–5]. In this context, active thermal management of the PV panels can be a promising solution to overcome these two critical problems.

In the present study, the two locations of Doha city in Qatar and Ipoh city in Malaysia were chosen as two case studies for a systematic investigation of the above-mentioned phenomena. The first location of Doha in the Emirate of Qatar (latitude of  $25.28^{\circ}$  N and longitude of  $51.53^{\circ}$  E) is one of the desert regions in the Middle East, which is exposed to dusty winds. Furthermore, the present dissertation project is part of a project on PV-driven solar cooling in Qatar [7, 8].

Figure 1.1 shows the annual weather data of Qatar as an example for harsh climate conditions. In Figure 1.1a, it can be seen that both air and dew point temperatures are strongly fluctuating between summer and winter and between day and night.

The maximum air temperatures of about  $45^{\circ}\text{C}$  are occurring in July and August, while the maximum dew point temperatures of up to  $28^{\circ}\text{C}$  reach from July to September. In Figure 1.1b, the yearly distribution of the hourly solar irradiation curves is shown. The maximum solar irradiation reaches up to  $1080\text{ W/m}^2$ . Due to these high temperature and irradiation values, Qatar was chosen as a typical representative for harsh desert climates, where the addressed problems of diurnal overheating and nocturnal dew formation mainly occur. Therefore, in the present study, Qatar weather data was taken to conduct yearly performance simulations of PV systems with and without active thermal control.

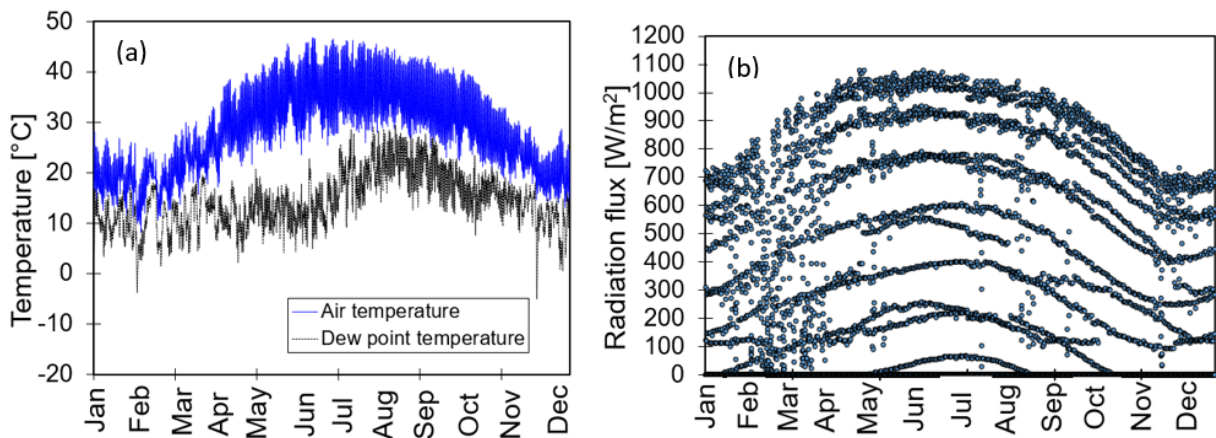


**Figure 1.1:** Annual weather data for Qatar (a) air and dew point temperature as well as (b) irradiation flux.

Figure 1.2 shows a satellite image of the Arabian Sea and the Middle East regions (e.g. Qatar) exposed to a dust storm. Here, it can be seen that the Middle East is prone to problems with developing mud layers on PV panels, especially with the background of occasionally high dew point temperatures. In the case of nocturnal dew formation, the exposure to dust and sandstorms leads to subsequent mud formation.

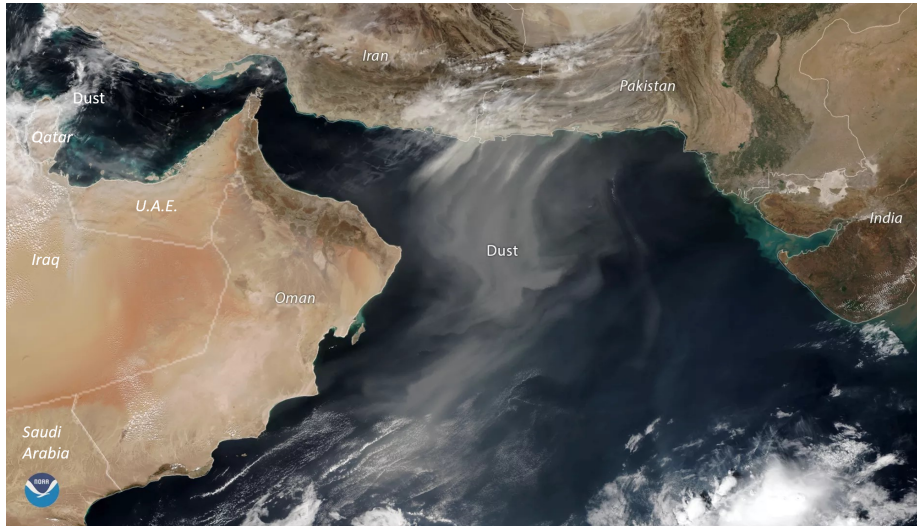


**Figure 1.2:** Dust blowing across the Arabian Sea and the Middle East regions [9].

The second location is Ipoh in Malaysia (latitude of  $4.39^\circ$  N and longitude of  $100.90^\circ$  E), which has a humid and warm climate. With its extremely high dew point temperatures, it is a suitable location to systematically study the effects of dew formation on the PV surface and to expose the proposed system to systematic efficiency tests. The four main factors reducing the performance of PV systems in desert areas can be summarized as:

- high diurnal PV cell temperature [1-6,11,16,17],
- nocturnal condensate formation [15,22],
- deposition of dust particles [12-14,18-27],
- subsequent mud formation [15,28-30].

In Figure 1.3, an overview of the problem scenario is given. The harsh climate conditions causing the problems of diurnal overheating and nocturnal mud formation are identified in the red box section. The major setbacks under a desert environment are the high ambient temperature during the day as well as the high relative humidity (%RH) at low ambient temperatures during the night in combination with exposure to dust-loaded winds.

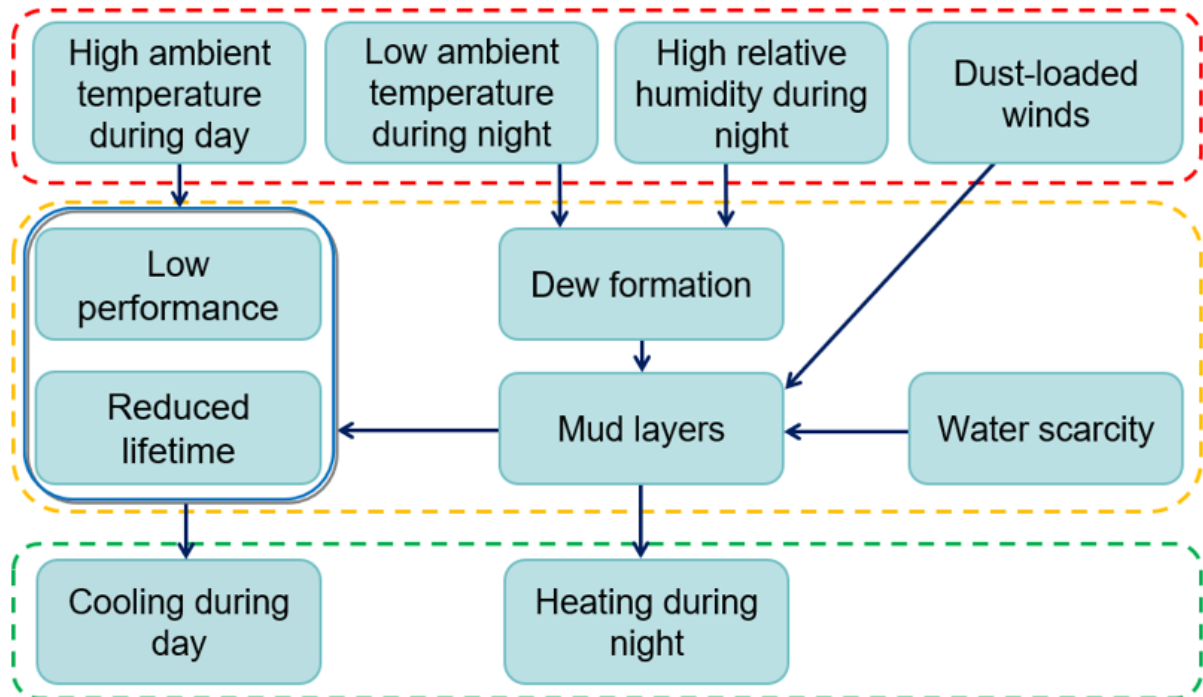


**Figure 1.3:** Problem description and solution strategy.

The problems resulting from these conditions are derived in the yellow box. The diurnal overheating leads to a reduction of the PV performance [11,16]. Additionally, it has been reported that the PV lifetime is reduced by elevated PV module temperatures [5,6]. During the night, the absolute humidity remains approximately constant, while the relative humidity rises due to the large drop in the ambient temperature between day and night. This can cause saturation. Together with a PV-surface exchanging radiation with the cold night sky, subcooling and finally dew formation occurs. Consequently, the exposure of a dew film to dust-loaded winds or sandstorms leads to mud layer formation on the PV surface. An accumulated mud layer effectively reduces the solar irradiation transmittance through the PV modules' glass cover. This again is causing a considerable reduction in the PV electrical efficiency [28-30]. Given this background, the problem solution lies on hand and is derived in the green box. Cooling the PV modules during the day helps to overcome the diurnal performance reduction. On the contrary, heating the modules to temperatures slightly above the nocturnal dew point is preventing condensation and subsequent mud formation.

In the present study, the novel approach is the introduction of an active thermal control system. This thermal control system includes a water bearing cooling and heating device on the backside of the PV panels together with a ground heat exchanger. Like this, the waste heat from cooling the PV panels during the day can be charged to the soil to provide thermal power for nocturnal heating.

### 1.1 Problem-Solving Approach

As was already described, diurnal overheating of the PV cells can be reduced by actively cooling the PV panels during the day. During the night, dew and mud formation can be prevented by heating the PV surface to temperatures above the dew point. For this purpose, an active thermal control system is needed for shifting the diurnal waste heat to the nocturnal heating application. As a heat transfer medium, water is a viable option because of its favorable thermal properties.

The proposed thermal control system is shown in Figure 1.4. It consists of a classical **PV** module with a rear water pocket filled with porous medium. In the further discussion, these two components will be addressed as so-called **PV/T**. It should be noted that the PV/T is not to harness both electrical and thermal energy as in conventional “PV/T hybrid collectors” but for providing an active cooling and heating system. The other main component of the thermal control system is the pipe loop heat exchanger (**HEX**). The HEX is buried in the ground soil (**GS**), which is used as thermal storage. The HEX transfers heat between the water flowing in the pipe and the GS. Thus, the two components can be called “ground soil heat exchanger” (**GSHEX**) and the overall system can be abbreviated as (**PV/T-GSHEX**). As was already indicated, the operation of the proposed system is divided into two phases: the diurnal cooling phase and the nocturnal heating phase. Figure 1.4 shows the operation of the proposed system during day (a) and night (b) with the main heat transfer phenomena.

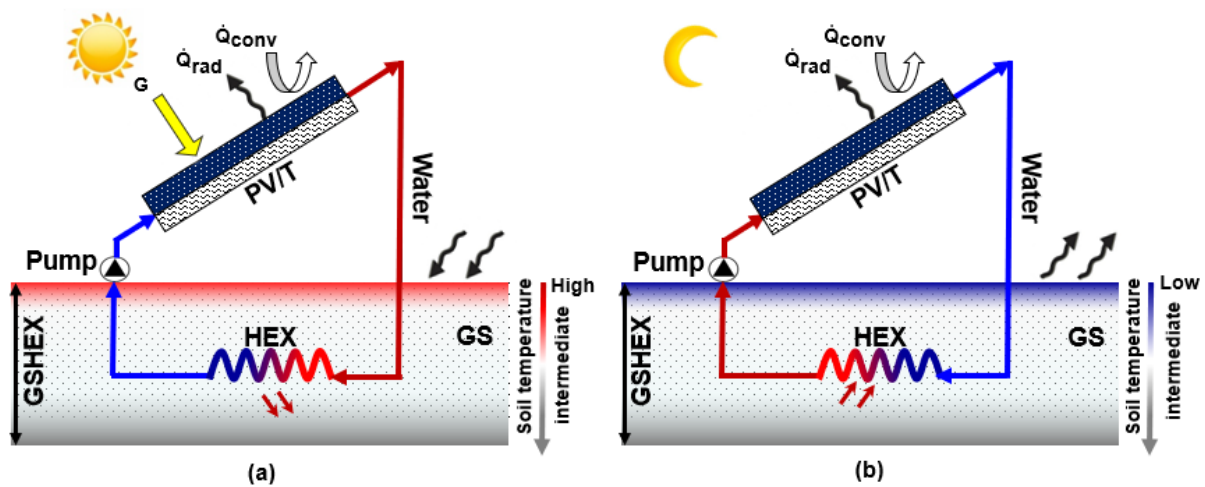


**Figure 1.4:** Operational principle of the proposed system with the main heat transfer phenomena (a) diurnal cooling, and (b) nocturnal heating.

**Diurnal operation:** The proposed system absorbs one portion of the incident solar irradiation ( $G$ ) and converts a part of it into electric power. Another portion of the absorbed irradiation is wasted as heat losses by convection and by radiation to the environment. The larger part of the absorbed irradiation is removed convectively by the cooling water mass flow. The removed heat is charged to the GS by the HEX and stored there. Later, the stored heat is used for the nocturnal heating process. During diurnal operation, the GS acts as a heat sink, see Figure 1.4a.

**Nocturnal operation:** During the night, the GS acts as heat source. Thus, the heat transfer process is reversed (from soil to water) and the heating water temperature is increased. Like this, the stored heat is used to keep the PV module temperature at values higher than the dew point temperature. As a result, both condensation and mud formation are prevented (Figure 1.4b) and the GS is regenerated for diurnal operation.

## 1.2 Motivation

The challenges for a good PV performance under harsh desert conditions or in arid regions are characterized by very high environmental temperatures together with high solar irradiation during the day. Under these conditions, the module temperatures are rising to 70°C or higher [8]. This does not only reduce the efficiency of the PV cells but also causes thermal stress to the modules, which significantly reduces their lifetime [5,6 - 13].

As can be seen in Figure 1.5, the issue of nocturnal dew formation under exposure to dusty winds is a real threat to the reliable operation of PV installations. The resulting mud layers are no theoretical issue but occur in daily practice.



**Figure 1.5:** PV Panels in a solar power plant in Qatar [15]. Mud formation can be observed in the center and right photograph.

### 1.2.1 PV Cell Efficiency Reduction Due to High Temperatures

Compared to the nominal Standard Test Conditions (STC) for PV panels ( $T_{PV} = 25^{\circ}\text{C}$ ,  $G = 1000 \text{ W/m}^2$  and AM 1.5) [32], elevated temperatures reduce the electrical efficiency of the cells. This reduction is described by a temperature coefficient  $\beta_{\text{MPP}}$  ranging from  $-0.5 \text{ \%}/\text{K}$  to  $-0.2 \text{ \%}/\text{K}$ , depending on the applied PV cell and module types [33]. This means that for instance in polycrystalline PV panels, every 1 K increase in PV temperature leads to a decrease in the electrical efficiency by up to 0.5 % [16,31]. The main influence is due to the cell types and to a lower extent also to the module design.

The PV system must be engineered not only according to the maximum, minimum, and average environmental temperatures at each location, but also with an understanding of the materials used in the PV panel. The effect of temperature on the electrical power  $P$  of a PV module can be traced to its influence on the current  $I$  and the voltage  $V$  as  $P$  is given by [32]:

$$P_{\text{MPP}} = V_{\text{MPP}} I_{\text{MPP}} = (FF) V_{\text{OC}} I_{\text{SC}} \quad (1.1)$$

In this fundamental expression, which also serves as a definition of the fill factor  $FF$ , subscripts MPP, OC and SC denote the Maximum Power Point, Open Circuit, and Short Circuit values, respectively, where:

$$I_{\text{SC}} = I_{\text{SC(STC)}} \frac{G}{1000} [1 + \beta_{\text{SC}} (T_{\text{PV}} - 25)] \quad (1.2)$$

and

$$V_{\text{OC}} = V_{\text{OC(STC)}} \frac{G}{1000} [1 + \beta_{\text{OC}} (T_{\text{PV}} - 25)]. \quad (1.3)$$

$\beta_{\text{SC}}$  and  $\beta_{\text{OC}}$  are the temperature coefficients of short-circuit current and open-circuit voltage, respectively.  $T_{\text{PV}}$  is the PV temperature at real conditions and the fill factor  $FF$  describes the non-ideality of the real  $I$ - $V$  curve.

It turns out that  $V_{\text{OC}}$  decreases substantially with temperature. Even though  $I_{\text{SC}}$  is slightly increasing, the substantial decrease in  $V_{\text{OC}}$  leads to a reduced power output  $P_{\text{MPP}}$ . Figure 1.6 shows the effect of temperature elevation on the PV cell characteristics [33]. As mentioned before, the output of a PV module is evaluated according to STC [32]. However, due to varying weather conditions, the actual PV output strongly differs from STC conditions.

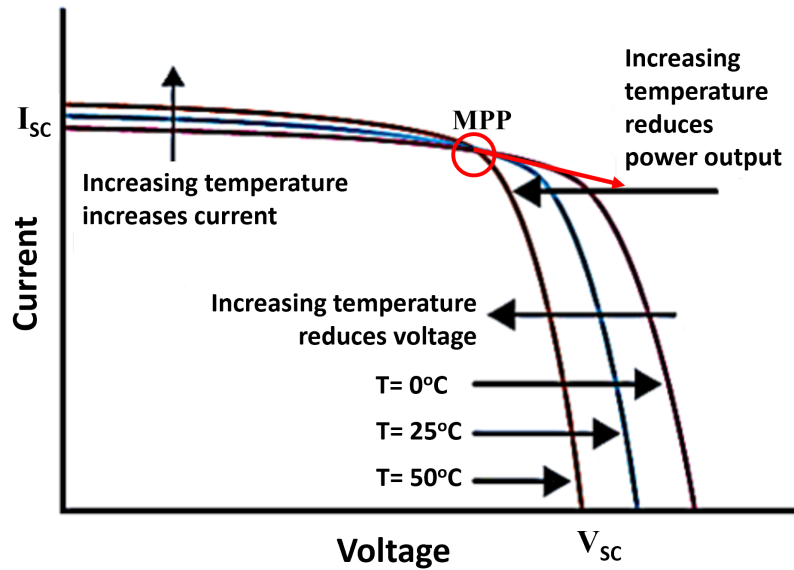


**Figure 1.6:** Temperature effect on the  $I$ - $V$  characteristics of the PV cell [33].

Another issue is the negative influence of high PV module temperatures on their durability [13-15]. Regarding the degradation of PV modules under fluctuating ambient temperature and solar irradiation, Dhimish and Alrashidi [39] conducted a study on solar panels in two regions with hot (Australia) and cold (UK) climate. The results showed that the degradation rate in the hot region is higher than in the cold region with degradation rates  $-1.35\%/a$  to  $-1.46\%/a$  in Australia and  $-1.05\%/a$  to  $-1.16\%/a$  in the UK. Another crucial problem concerning the PV cell temperatures is the mud formation itself. The mud causes a glass transmittance reduction and absorption increment, which leads to a further decreasing performance of the PV panel. Furthermore, nonuniform dust accumulation causes partially shaded areas on the PV module. In case of severe partial shading, the voltage in the shaded cell becomes negative, and a hot-spot can emerge. In case of minor partial shading, the  $I$ - $V$  curves of the cells differ. This leads to efficiency reductions due to the mismatches [83]. Thus, diurnal cooling of the PV modules together with a mitigation strategy for mud formation is a beneficial approach for the reliable operation of PV systems under desert or humid conditions. The mechanisms of condensation and mud formation will be described in the next section.

### 1.2.2 Condensation and Mud Formation

Sandstorms are a frequent and challenging weather phenomenon in deserts that can even be witnessed in large urban areas such as Doha and Baghdad [15,17]. Combined with the possibility of dew formation due to the prevailing high ambient air humidity, the dust particles are accumulated and stick on the PV glass surface.

#### Soil Dust Deposition on PV Glass Cover

Even though the phenomenon of dust accumulation is crucial for the operation of PV systems in desert areas, the current knowledge on characterizing the deposition of dust and its impact on PV system performance is limited. This is because dust deposition is a complex phenomenon, which is influenced by diverse site-specific environmental conditions [18, 19]. Hamdy et al. [20] investigated dust formation after thunderstorms using an experimental test rig with different tilt ( $\theta$ ) and azimuth angles ( $\gamma$ ). The glass transmittance was evaluated over seven months. The results revealed a reduction in glass transmittance, being a function of the dust deposition density [ $\text{g}/\text{mm}^2$ ] in conjunction with the inclination angle, the surface orientation, and the wind direction. A reduction in solar transmittance by 5 % over 10 days was observed in the study of Malizia et al. [21], using pyranometers. Despite instances of rain, less than 1 % decrease in this value was observed for unclean pyranometers. Some other studies [18,22-24] investigated dust accumulation using varying parameters (e.g. environmental conditions, dust characteristics, surface characteristics). The soiling effect is of high concern for areas with high dust deposition, condensation, and low rainfall. An outdoor installation showed a reduction of PV efficiency by 30 % for 150 days [26,27], see Figure 1.7. However, the mechanisms and effects of dust accumulation and mud formation were not adequately investigated and described yet.

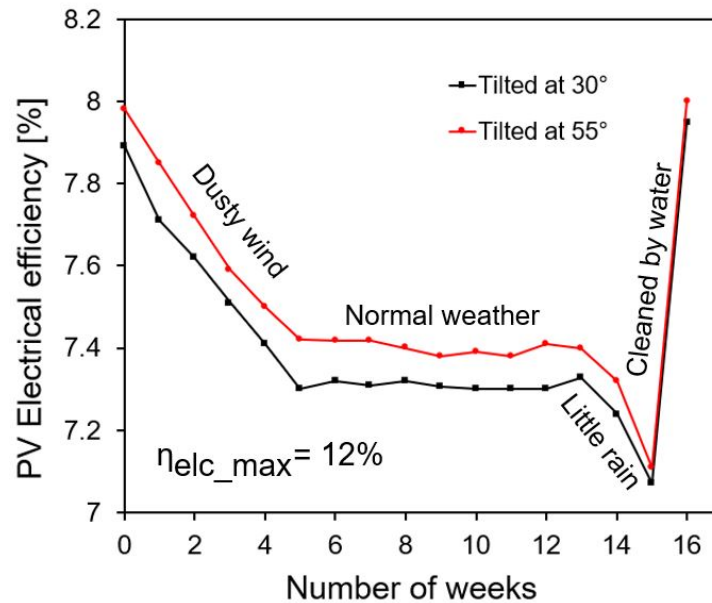


**Figure 1.7:** Accumulated effect of dust deposition on PV performance under different weather conditions and inclination angles [26].

### Effects of Water Vapor Condensation on PV Glass Covers

Generally, if humid air is cooled below the so-called dew point temperature, air humidity reaches saturation and condensation is setting in [35]. In the present application, this is happening at the surface of the PV glass cover. Due to the high spectral emissivity of glass in the long-wavelength region of thermal radiation and the low nocturnal sky temperatures, radiative heat losses from the PV glass cover lead to low surface temperatures of the PV modules. The onset of condensation is a function of relative humidity, the air temperature at the boundary to the solid surface, and the presence of condensation nuclei [127, 128]. In real PV applications, stronger cooling might occur. However, it is reported by both Bing et al. [37] and Figgis et al. [38] that condensation set in even at glass temperatures that were by 2 K higher than the dew point temperature. The reasons were not discussed in their report, but it was recommended for a future study to investigate this phenomenon. Dew formation enhances dust settling on the modules' flat surfaces, while evaporation, on the other hand, reinforces dust adhesion to these surfaces as shown in Figure 1.8 [42]. Here, the removal of the mud layer is shown.



**Figure 1.8:** Dust adhesion on PV panels due to dew formation and exposure to dusty winds [42].

Some studies were conducted on the effect of condensation and dust on light transmissivity as well as on the related measurement methods [59-64]. Most of the investigations were focusing on the effect of condensation on greenhouse applications [109,117-127]. A few publications [38,39,66] were dealing with the effect of condensation on the performance of PV panels. However, the adhesion of dust particles and mud formation on the PV protective glass was barely covered.

The transmittance and the reflectance of the glass surface change according to the current state of the surface (e.g. wetness). Graefe et al. [60] revealed that the measured difference of hemispherical transmittance between a dry and wet surface for an incidence angle of  $5^\circ$  were  $\Delta\tau = 4.31\%$ . In another study, the average loss in transmission due to dust accumulation and condensation was approximately 9% - 15% [61]. A transmittance reduction of up to 23% in greenhouse cladding (with / without condensation) was observed by Pollet et al. [62]. Transmission properties of dry and wet greenhouse cladding materials showed a maximum degradation of 4% in glass transmittance for  $90^\circ$  tilt angle [63]. Dew formation was also identified as a promotor of dust deposition on the surfaces of solar thermal collectors [158].

## Mud on PV Glass Covers

As already mentioned, the combination of sand or dust storms and dew formation on the PV surface can cause mud formation. This could damage the PV modules and the antireflective coating on the front glass. Moreover, due to heavy losses in transmittance, mud layers on the PV modules must be removed. This adds to the need for efficient maintenance planning [27]. The mud formed on the glass surface significantly influences the glass properties, including reflectance due to changes in microhardness and surface texture as well as absorbance of the glass [27]. The dust particles were found to be composed of a non-uniform distribution of alkali and alkaline earth metals, oxygen, silicon, sulfur, iron, etc. The average size of the particles is in the order of  $1.2 \mu\text{m}$  [28,29]. Due to the dissolving of the ground composites (alkali and alkaline) in the mud, a reactive solution between mud and glass is formed. This solution alters the texture of the surface. Furthermore, potassium increases the surface hardness, which finally results in a slight difference in absorbance and reflectance. Figure 1.9 shows that the light transmittance was reduced even after the glass was cleaned [28].

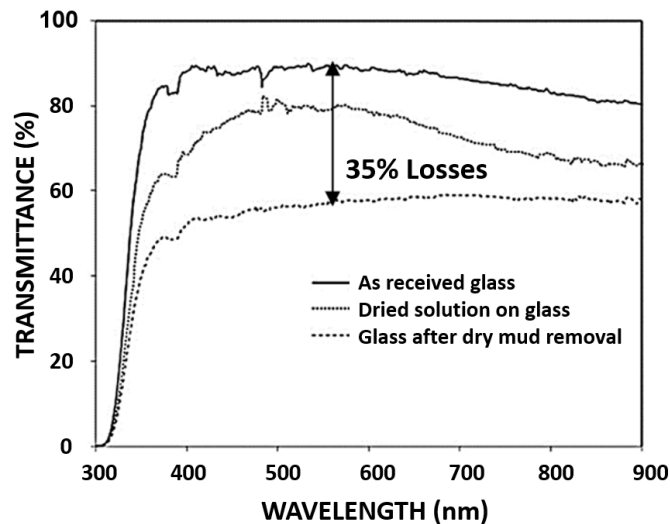


**Figure 1.9:** Transmittance of the as-received glass, glass after dry mud removal, and glass with the dried solution [28].

This reduction is associated with:

- mud residues that remain after cleaning the glass surface and
- chemical changes in the glass surface due to chemical reactions with alkaline and alkaline earth hydroxide.

Yilbas et al. [28] conducted a chemo-mechanical study of mud formed from environmental dust particles in humid air. They suggested that the adhesion work should be higher than the frictional work performed on the glass surface during the mechanical removal of dry mud from the glass surface. In addition, mud formed from dust particles on a polycarbonate surface was experimentally investigated [29]. The quasi-crystalline structure results in a surface made up of pyramids to reduce the light reflection losses. However, mud residues on the surface could cover the micro/nano texture and lower the surface hydrophobicity. Mud residues, remaining on the surface after water cleaning, can also increase the friction coefficient between the mud residues and the PV surface, which increase the sediment accumulation on the PV panels and lower the optical transmittance [28,30]. In addition to scratching the glass cover [120], this leads to a decrease in PV efficiency and life time. Few investigations [35-37] were conducted on the nature and the characteristics of the dust particle itself like its composition, size (coarse or fine), and accumulation rate during the mud formation.

The influence of varying wind regimes on dust deposition was investigated by Goossens and Van Kerschaever [23]. The results of their investigations indicated that high wind speeds promote dust accumulation on surfaces. A comprehensive study on the impact of dust accumulation on the PV panels has been conducted by El-Shobokshy and Hussein [37]. This study includes investigations on the physical properties of dust accumulation and deposition density and their impact on parameters degrading the PV efficiency. The results showed increasing deterioration of PV performance for all investigated dust types.

### 1.2.3 PV Cleaning Methods

As was already concluded, proper cleaning methods are required to maintain the original performance of the PV panels. The most common methods that have been established for the cleaning of the PV panels are:

- (1) Mechanical methods such as manual and robot cleaning [69,71,72,75]. The manual method requires handwork, which exposes workers to risks, while the robot method requires special cleaning materials, periodic maintenance, and energy for operation.
- (2) Electrostatic method. In this method, the dust particles are ionized on the surface, attracted by the positively charged electrode, and collected there [73,74]. Particles attached to positively charged plates should be expelled or periodically removed either manually or automatically to keep the electrode dust-free. However, both energetic effort and cost are high.
- (3) Standing wave electric curtain. Although this method needs only a single phase current rather than three phases like the previous one, dust particles residue on the surface is high [71,72,79].
- (4) PV coating. This method assists the cleaning process and could be in the wet or dry state [70,76]. In the case of wet cleaning, droplets of water of 20  $\mu\text{m}$  are used to roll onto the glass surface, carrying away the dust particles. However, dry cleaning needs a vibrational excitation to ensure the movement of the particles. In both cases, dust residues were observed on the surface after the cleaning procedure [72,75,79]. This phenomenon becomes more significant in wet cleaning when using large droplets. Large droplets will stably attach to the surface, promoting mud formation instead of removing the dust.

Table 1.1 shows an overview of PV cleaning methods and their advantages and disadvantages, which are summarized from relevant publications in this field [68-79]. Some of these methods, such as electrostatic cleaning, standing wave electric curtain, and the coating method become ineffective when there is already a condensation layer on the PV surface [68,72]. Other methods clean

the glass surface after the mud is already formed [28,71].

**Table 1.1:** Overview on PV cleaning methods and their pros and cons [68-79].  
(↑ [high], ↓ [low], – [zero])

Cleaning method	Cost	Energy consuming	Time and effort	Efficiency deterioration	Risk for workers	Particles residue
Mechanical cleaning (Manual cleaning)	↓	↓	↑	↑	↑	↑
Mechanical cleaning (Robot cleaning)	↑	↑	↓	↓	–	↓
Electrostatic cleaning	↑	↑	↓	↓	–	↑
Standing Wave Electric Curtain	↓	↑	–	↓	–	↑
Hydrophobic/philic coating	↓	↓	–	↓	–	↑

It can be concluded that cleaning methods are either expensive (installation/energy cost) or cannot guarantee dust removal before or when condensation occurs. Besides, none of the discussed cleaning methods restores the glass to its original state before mud formation [28-30]. None of the proposed methods can get to the root of the problem, which is to avoid mud formation in the first place. Therefore, an effective method to prevent condensation, which in turn mitigates mud formation shall be developed in the present project.

## 1.3 Established PV Thermal Management Strategies

### 1.3.1 Diurnal Cooling of the PV Modules

Generally, cooling management of PV modules in hot climates can be achieved by either passive or active cooling strategies:

**Passive Cooling:** here, no additional power is required. Passive Cooling can be achieved by natural (air) convection [49], radiation, or by any other

natural sources. Radiative cooling promotes heat exchange with the cold sky in the infrared (IR) wavelength range [79-82]. Sun et al. [82] suggested using some materials that promote radiative cooling, such as soda-lime glass to cool a single PV cell. The study applied two panes of soda-lime glass at the front and rear sides of the PV cell for more cooling. Soda-lime glass has a high emissivity, which is close to unity in the medium IR wavelength region. Although the rear side did not face the sky, both sides contributed a significant amount of cooling. An improvement in module's efficiency around 18 % can be achieved compared to conventional setups without radiative cooling [80,82]. However, radiative cooling also promotes condensation. Thus, the problem of mud formation is even intensified. Therefore, this method is not feasible for the present application.

**Active Cooling:** here, artificially forced convection by air or water cooling is applied. Air cooling methods were found to decrease the temperature of the solar cell by 4.7 K, which corresponds to an increase in solar panel efficiency by 2.6 % [48]. However, at high ambient temperatures of up to 50°C, air cooling is less effective compared to water cooling [50]. In this case, water cooling techniques are widely used. Front water film cooling is one of these techniques. It can achieve a reduction in PV module temperature in the range of 20 %–26 % with an improvement in electrical efficiency up to 15.5 % maximum [41,42,44-46]. Water spray is another PV cooling technique that can achieve an increment in the maximum PV module efficiency of up to 12.1 % [47,48]. Hence, water cooling becomes a necessity for efficient PV temperature reduction. However, these cooling systems are economically and practically not feasible in desert climate conditions due to water scarcity. In many ways, the performance of active cooling systems with a rear heat exchanger is much better. The setup of these PV modules with integrated heat exchanger is quasi similar to hybrid PV/T collectors. Rear heat exchangers achieve a reduction in the PV cell temperature as high as 30 K with an improvement in electrical efficiency of up to 22 % [42,49-58]. PV/T collectors have been established in a wide range of applications such as domestic water heating, space heating and cooling. They have the flexibility to connect to close or open fluid circulation systems [51-55].

In the present study, a PV module setup similar to PV/T collectors was applied in order to achieve active thermal control of the PV cells. Active thermal control means both diurnal cooling and nocturnal heating.

### 1.3.2 The GSHEX System

As was already described, the proposed active thermal control system can be used for both cooling during daytime and heating during nighttime. Therefore, it would be beneficial to shift the waste heat from diurnal cooling to the nocturnal heating process. Thus, the system shall be equipped with an underground heat storage, which has two main components. As thermal storage medium, simply the ground soil storage (GS) is used. In order to enable heat exchange between cooling/heating water and the storage medium, the GS is equipped with a water-soil heat exchanger (HEX), which can consist of a water pipe buried below ground level.

**Ground Soil GS:** In general, the GS is suitable for thermal energy storage because, in most cases, the ground soil has a high heat capacity and a low thermal conductivity (which reduces the heat losses). Therefore, it can act as a heat source/sink. Moreover, heat storage is possible on a short-term or seasonal basis [85-87]. Such systems can provide largescale storage of cold and heat in natural underground sites [88,89]. Without any external disturbances (e.g. aquifer water flow), they are barely affected by local climate variations above ground and maintain a stable soil temperature [90,91]. Hence, they provide a low-effort possibility for storing thermal energy from solar collectors or, as discussed in the present study, from the active cooling of PV panels. To determine the optimal depth of the HEX is one of the tasks in the present work. During the daytime, the waste heat from the PV modules can be stored for around 12 hours or less. In the diurnal operation mode, the soil serves as a heat sink. Removing the heat for nocturnal heating purposes means cooling down the thermal storage and regenerating it as a heat sink for the following day.

**Heat Exchanger HEX:** The HEX can be of various designs, with pipes or tubes that can be aligned in the ground either vertically or horizontally [92-96]. Both variants have their benefits and drawbacks, which are briefly summarized in Table 1.2. A horizontal HEX is designed for relatively small heat loads [100]. For small heat load applications, like the thermal management of PV modules in the present study, horizontal heat exchangers shallowly situated underground are more cost-effective than vertical arrangements. It has to be pointed out that, preferably, this type of HEX is located where the surrounding soil temperature is more or less uniform [92]. Compared to vertical HEX, where the soil temperature varies with depth [93], heat transfer in the horizontal HEX arrangement is more effective [88]. Considering all factors, a horizontally aligned HEX with GS as thermal storage is applied in the present study.

**Table 1.2:** GSHEX system arrangements with their benefits and drawbacks [85-96]. (↑ [high], ↓ [low], – [zero])

GSHEX systems	Cost	Space flexibility	Arrangement flexibility	Effective heat transfer	Small applications
Vertical	↑	–	↓	↓	–
Horizontal	↓	↑	↑	↑	↑

## 1.4 Study Objectives and Research Approach

As was discussed in the previous sections, the application of an active thermal control system for PV modules in desert regions seems to be a viable option for tackling the addressed problems. The primary goal of a thermal control strategy is to avoid diurnal overheating and nocturnal dew formation with the subsequent build-up of mud layers. These are crucial factors to improve the efficiency and prolong the lifetime of PV systems under harsh desert conditions. This objective is supposed to be fulfilled by cooling the PV panels during the day and heating them to temperatures above the dew point during

the night. To avoid additional energy consumption and thus low PV net efficiency, the stored waste heat from daytime operation can be used as a heat source during nighttime. A detailed description of the research approach is outlined in Figure 1.10.

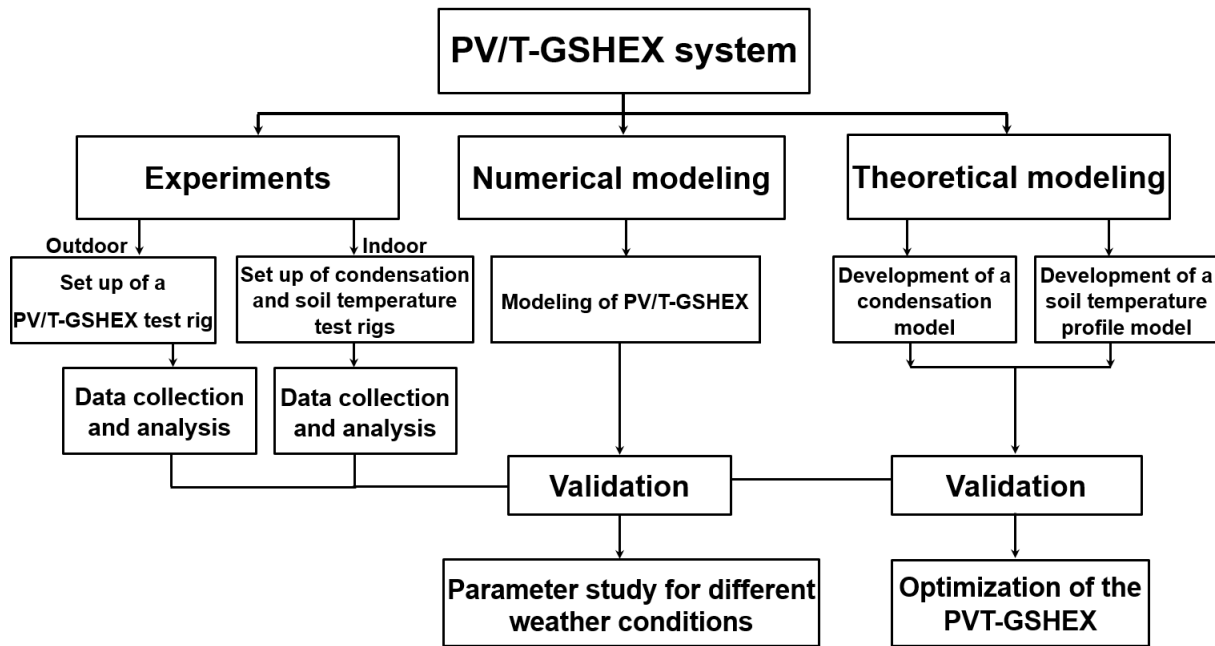


**Figure 1.10:** A detailed description of the proposed research approach.

Firstly, an experiment is carried out to investigate the performance of the proposed system. In this experiment, two distinct cases of indoor and outdoor experiments are involved:

The **outdoor experiments** are including comparative measurements on a conventional PV module and on a structurally identical, but improved PV module with thermal control system (PV/T with GSHEX).

In the **indoor experiments**, condensation phenomena on the PV modules' glass cover are studied. Here, the impact of varying ambient conditions together with dust accumulation on the onset and characteristics of condensation are of particular interest.

Secondly, a **numerical model** for the proposed system using the Matlab/Simulink platform is developed. The model is designed to predict the

electrical performance of the PV modules with and without active thermal control. The results are validated using the experimental data.

The knowledge of the yearly soil temperature distribution is crucial for the optimum placement of the HEX, which consequentially has an impact on the efficiency of the proposed system. Therefore, a one-dimensional theoretical **model for computing soil temperatures** at different depths is included in the study. Another **theoretical model** to investigate the effect of different conditions on the **onset of condensation** on the PV surface is also developed. Subsequently, the two models are validated with indoor experiments and applied to optimize the proposed PV/T-GSHEX system.

## 1.5 Thesis Overview

The present study is organized into six chapters with the following content:

**Chapter 1 - Introduction:** The study background, problem statements, study objectives, and the research approach were presented in the current chapter. A novel thermal control approach was developed in order to mitigate the main problems of applying PV in desert conditions. The state of the art for different types of PV cooling systems was described and a comprehensive overview of their performance was given. Different techniques for enhancing PV performance were discussed. Furthermore, the effects of condensation, dust and mud formation on the PV performance were presented.

**Chapter 2 - Experimental Investigation of the PV/T-GSHEX System:** The experimental investigation on PV/T panels with coupled GS and HEX will be discussed in this chapter. The test results will be compared with results from parallel measurements on a structurally identical, but conventional PV panel.

**Chapter 3 - Analysis of the Soil Temperature Distribution (STD):** In this chapter, an analytical model of the vertical STD with experimental validation will be presented. In the calculations, the meteorological data as well as the thermophysical properties of the soil were considered. Based on the assump-

tion that a quasi-constant temperature is favorable for the HEX installation, the model can predict the optimum installation depth under different climate conditions.

**Chapter 4 - Modeling of the PV/T-GSHEX System:** In this chapter, the mathematical model of the proposed PV/T-GSHEX system will be presented. The mathematical model was implemented in Matlab/Simulink and validated with the outdoor experiments during both day and night. The model will be used to conduct a parametric study to verify the performance of the system under different weather conditions.

**Chapter 5 - Experimental and Theoretical Investigations of the Condensation Phenomena:** In this chapter, experimental and theoretical investigations on the effect of environmental parameters such as the air velocity and the micro-dust layer thickness on the onset of condensation and on the droplet growth will be presented. The results will be used to verify the PV/T-GSHEX model, which is assuming a clean PV surface. It will be investigated, whether the assumption of a clean PV surface is strongly deviating from real-life behavior in the field.

**Chapter 6 - Conclusion and Outlook:** In this chapter, the main findings and their relevance for further work will be presented.

## **2 Experimental Investigation of the PV/T-GSHEX System**

In the present chapter, an outdoor test series with the PV/T-GSHEX system was carried out. A comparative experimental study on PV with/without thermal control was performed. Malaysia with its harsh, hot and humid climate was chosen for the outdoor test series. Malaysia is a location, where condensation phenomena are likely to appear frequently, which serves experimental studies on the topic. The developed technique will be proven to be highly efficient as PV thermal control method [101].

### **2.1 Outdoor Experiment**

In the following sections, the test equipment will be described. The ground soil heat exchanger GSHEX system was designed and integrated with a PV/T panel. Measured parameters of each test were the PV surface temperature, cooling water and soil temperatures and the electrical power output of the PV panel. Later, a mathematical model was developed and validated with the experimental results.

#### **2.1.1 Experimental Setup**

The experimental setup was installed at the solar test site at University Technology Petronas (UTP). The setup consists of four primary components: the PV/T panel, the GSHEX, the water circulation pump, and the measurement devices. Figure 2.1 shows the experimental setup in a flow diagram (left) and in the constructive implementation (right).

The figure shows the arrangement of the GSHEX unit with the PV/T panel and the location of the water flow meter, the pump and the thermocouples. During the daytime tests, the water is heated up inside the PV/T panel and then passes through the GSHEX pipe, where the heat is discharged to the soil and the water is cooled back.

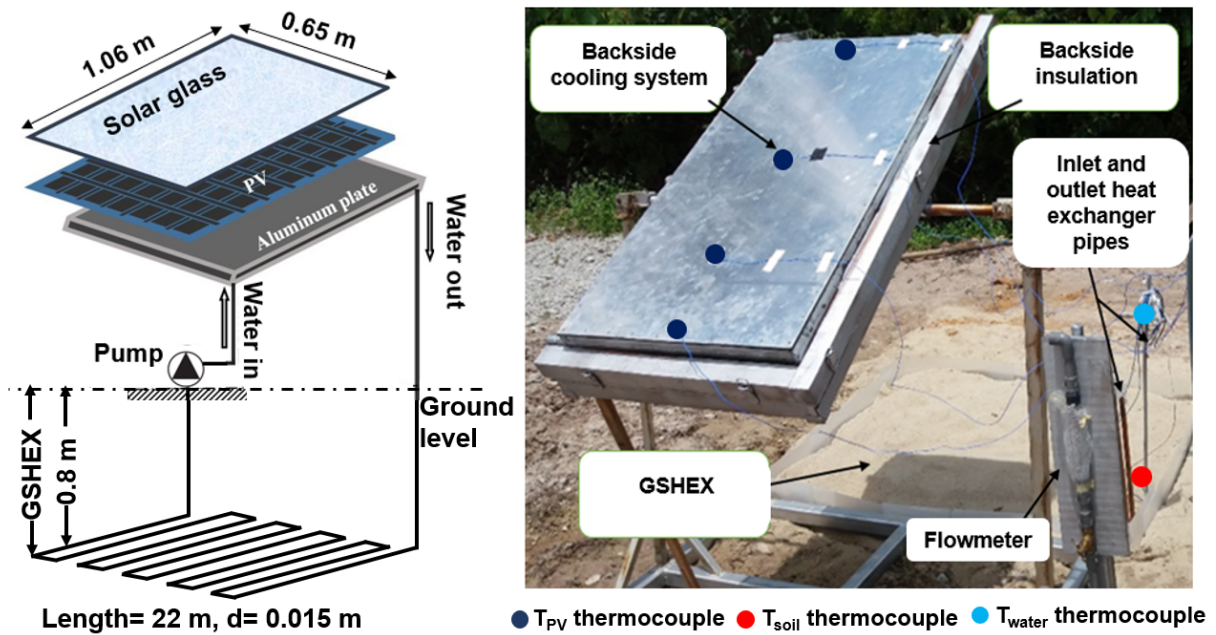


**Figure 2.1:** Schematic diagram of the PV-GSHEX system (left) and the system during the installation stage (right).

## PV Panel

The PV panels used in the present study are Solarland SLP100-12 with Polycrystalline silicon cells consisting of 36 cells in 4 strings. The module dimensions are 106.2 cm × 65 cm × 3.0 cm, and the weight is 8.9 kg [145]. The PV cells are covered with a 4 mm thick protective solar glass. The material of the frame is anodized aluminum. Detailed specifications of the PV panels are listed in Table 2.1.

**Table 2.1:** PV module electricity performance parameters at Standard Test Conditions (STC  $1000 \text{ W/m}^2$ , AM 1.5 and  $T_{PV} = 25^\circ\text{C}$ ).

Model	SLP100-12, Polycrystalline
Rated Power [W]	100
Rated voltage [V]	17.2
Rated current [A]	5.81
Open circuit voltage [V]	21.6
Short circuit current [A]	6.46
Temperature coefficient [%/K]	$-(0.5 \pm 0.05)$
Reference electrical efficiency [%]	14

### PV Rear Cooling System

One PV panel was modified with a rear cooling water pocket with dimensions  $1.04 \text{ m} \times 0.61 \text{ m} \times 0.02 \text{ m}$ , as shown in Figure 2.2.

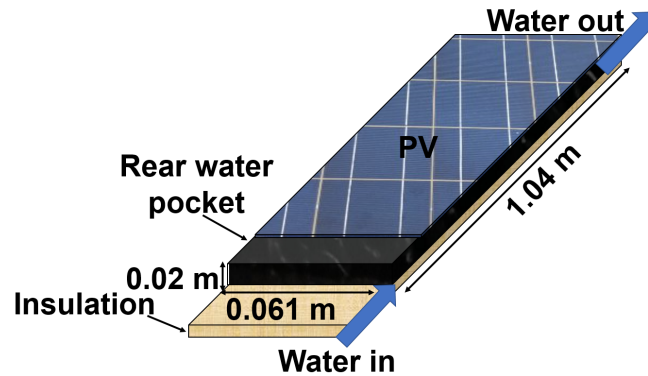


**Figure 2.2:** Rear cooling water pocket.

The water pocket was equipped with a porous media packing to guarantee a uniform water flow distribution and to enhance heat transfer from the PV backside. The dimensions of the packing material are  $0.94 \text{ m} \times 0.61 \text{ m}$ . It was made of Polyethylene with a thermal conductivity of  $0.86 \text{ W/mK}$  and a maximum applicable temperature of  $115^\circ\text{C}$ . The PV/T system was insulated from

the backside by 4 cm glass wool insulation with a density of  $55 \text{ kg/m}^3$ , thermal conductivity of  $0.032 \text{ W/mK}$  and a maximum operation temperature of  $400^\circ\text{C}$ . A DC water pump (4.2 W, 240 l/hour, and 300 cm head) is used to continually circulate the water between the water pocket and GSHEX unit. The PV/T panel was mounted on a metal frame with an angle of inclination of  $27^\circ$ . The hydraulic connection to the GSHEX was insulated with a standard pipe insulator with thermal conductivity of  $0.32 \text{ W/mK}$ , density  $55 \text{ kg/m}^3$  and maximum applicable temperature between  $50^\circ\text{C} - 110^\circ\text{C}$ .

### Ground Soil Heat Exchanger GSHEX

The HEX was made of a copper pipe loop. The copper pipe had a diameter of 15 mm, 3 mm thickness and a total length of 22 m. The HEX was located at 0.8 m depth, which was determined by preliminary calculations with ANSYS Fluent platform. Figure 2.3 shows the arrangement of the HEX unit during the installation process.

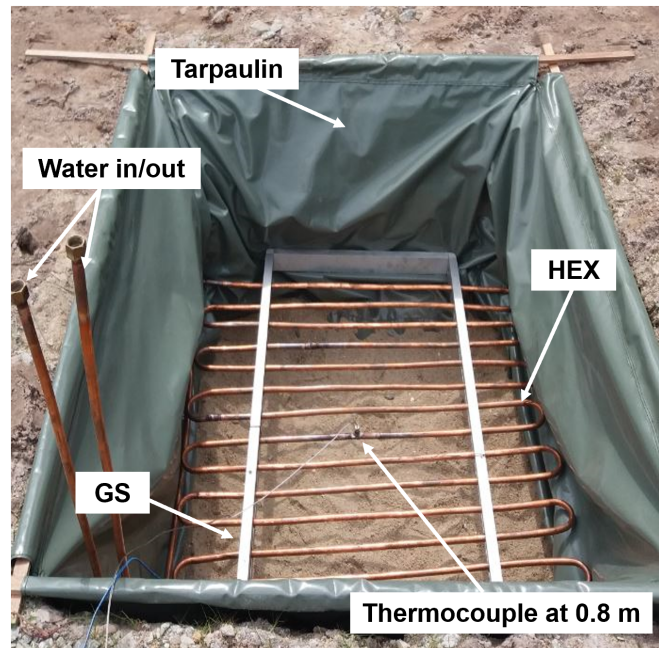


**Figure 2.3:** The GSHEX during the installation.

The location of the soil thermocouple at 0.8 m is also shown in the figure. Two thermocouples were used to measure the soil temperature at different depths: 0.5 m and 0.8 m. A tarpaulin was used during the installation of the HEX to prevent the potential impact of water flow.

For the GS, two soil types were used: dry soil (low thermal conductivity) with low moisture content of 0.06 % to simulate the dry soil in semi-arid regions or arid zones and wet soil (high thermal conductivity) with a high moisture content of 24.62 % for tropical areas, see appendix A. The thermal conductivity of both types of soil has been measured by using a thermal properties analyzer model KD2 Pro. The different moisture contents were used to investigate the effects of different thermal conductivity and heat capacity of the soil on the heat exchanger efficiency.

### 2.1.2 Measurement Equipment

All thermocouples used in the present study were Type-K. The temperature measurement ranges of Type-K thermocouples are  $-270^{\circ}\text{C}$  to  $1260^{\circ}\text{C}$  with a systematic uncertainty of  $\pm 0.75\%$ . All thermocouples were calibrated with the temperature calibrator DRUCK DBC650. Special care has been taken to account for the solar irradiation effect on the thermocouples by using radiation shields placed around them. All the thermocouples were connected to a Multi-Channel GRAPHTECH Data logger, for instant temperature data collection and storage. A Multifunction KIMO AMI 300 hygrometry probe with a measurement range from 3 % RH to 98 % RH and 0.1 % resolution was used to measure the relative air humidity and the dew point temperature. Measurement accuracy was  $\pm 0.3\%$  for the instrument,  $\pm 0.6\%$  for the dew point, and  $\pm 0.1\%$  for the relative humidity. A rotameter type MBLD was used to control and measure the water flow rate with a maximum flow rate of 4.0 l/min and operating temperature between  $0^{\circ}\text{C}$  and  $65^{\circ}\text{C}$ . The global solar irradiation was measured at the module level using a solar meter KIMO SL200 with a measurement accuracy  $\pm 5\%$ . The output parameters, voltage and current for the two 100 Wp solar PV modules are measured using a voltmeter and amperemeter, respectively.

The maximum output power (MPP) for every hour during the day, is measured by using a rheostat (10  $\Omega$ , 120 W). By collecting the MPP for every hour, a MPP-Power output over the day of both PV and PV/T-GSHEX system can be obtained.

### **2.1.3 Experimentation Environment**

The system was run for five days with two types of soil (high and low moisture content) for three water flow rates. During the five experimentation days, only the fair days with no clouds were considered. The thermal performance of all system components was determined using temperature data and water mass flow rate with a temporal resolution of 5 minutes. Then, average values were calculated then for every 30 minutes. The results presented in the following sections were obtained by comparing the efficiency and temperature of the PV/T panel with the data of the conventional PV module. Both PV panels had the same measurement specifications.

## **2.2 Experimental Results**

In the following subsections, the experimental results will be analyzed in detail. In particular, the PV surface temperature, the electrical efficiency, and the heat flow (charge and discharge) between GS and HEX for soil with high and low thermal conductivity will be discussed.

### **2.2.1 Experiment Verification Test**

Interesting facts can be observed from the measurement of the PV and PV/T surface temperature and the dew point, see Figure 2.4a. The red and the blue curves represent the PV and the PV/T surface temperatures while the black and the green curves represent the air and dew point temperatures. To verify the practicability of the proposed method, comparative dew formation tests

## 2.2 Experimental Results

on a PV system without a thermal control system were performed. Condensation was found on the PV solar glass surface from 3:30 AM until 7:30 AM on the experimentation day, while no condensation built up on the PV/T surface at the same time and under the same weather conditions.

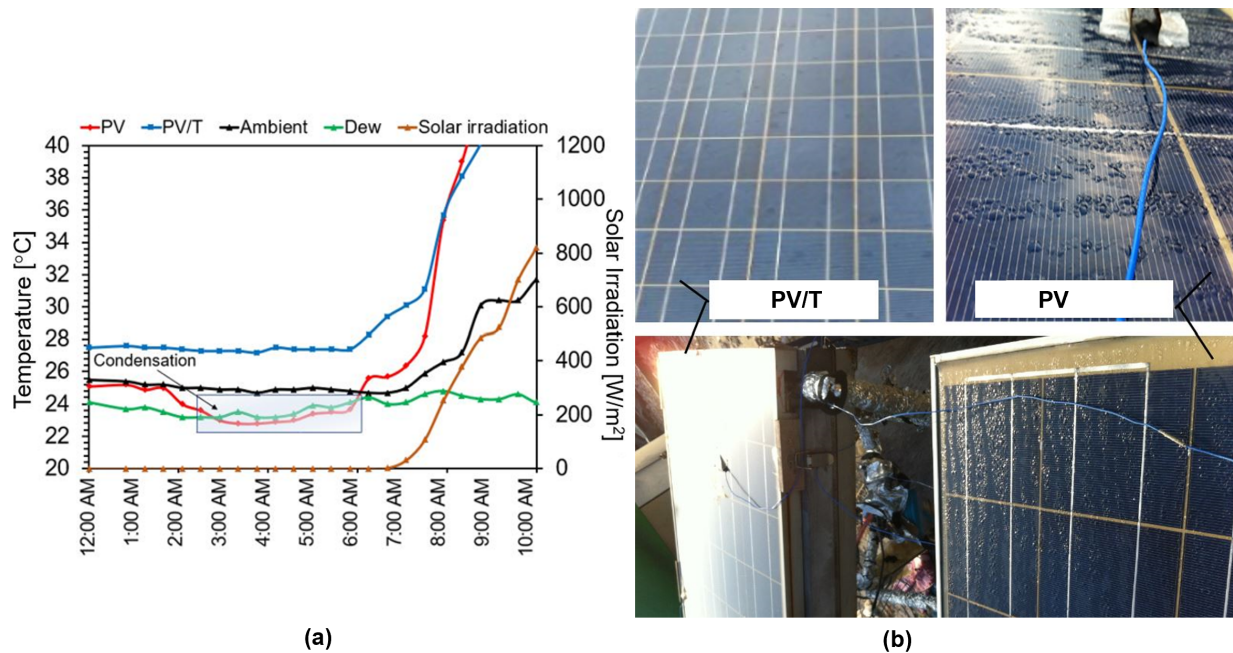


**Figure 2.4:** Measurement data of the condensation period (a) and photos of the dry PV/T surface and condensation on the PV surface (b) at the same time, 7:30 AM.

This phenomenon is represented by the rectangular area on Figure 2.4a where the PV surface temperature is lower than the dew point temperature. This phenomenon is also observed in another study by Al-Kayiem et al. [158]. This can be also visualized as clearly seen in Figure 2.4b, as was theoretically expected. Condensation phenomena could be observed on different days during the test period. Therefore, dew formation on conventional PV panels, even during early daylight, can be confirmed. It could also be shown that no condensation appears on the PV/T-GSHEX system.

## 2.2.2 PV and PV/T Surface Temperatures

Figure 2.5 shows the effect of the thermal control system on the PV/T surface temperatures. The blue line shows the surface temperature of the modified PV/T system with GSHEX, the red curve that of the conventional PV system.

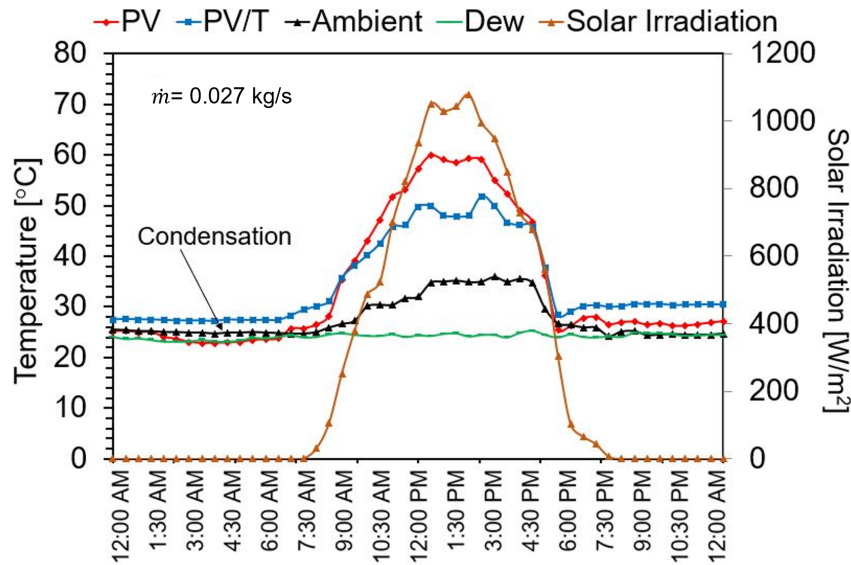


**Figure 2.5:** Measurement of the ambient, PV surface (PV), PV/T surface (PV/T), and dew point temperature and solar irradiation.

It can be seen that at noon time, the surface temperature of the actively cooled system is by 8-10 K lower than that of the PV panel. This is enough to keep the PV cell temperature close to the nominal operating cell temperature NOCT, around 47°C [145]. During the condensation period from 3:30 AM to 7:30 AM, the GSHEX can keep the PV/T surface temperature 2-4 K above the dew point temperature. This can be seen more clearly in Figure 2.4a with  $T_{\text{dew}} \approx 24^\circ\text{C}$  and  $T_{\text{PV/T}} \approx 28^\circ\text{C}$ .  $T_{\text{PV}}$  lies below the dew point at around 23°C. As can be seen, the temperature profiles of PV and PV/T clearly show the dew mitigation potential of the proposed system.

### 2.2.3 Electrical Efficiency of PV and PV/T Panel

A comparison of the PV/T electrical efficiency with the conventional PV system is presented in Figure 2.6. It can be observed that the PV/T panel significantly improves the electrical efficiency for the maximum solar irradiation of up to  $1000 \text{ W/m}^2$ . Due to the already described PV cell temperature reduction of 8-10 K, the electrical efficiency increased from 10.9 % to 12 %. This result is equivalent to an improvement of 10.1 %, which matches the data from previous studies [1-7].

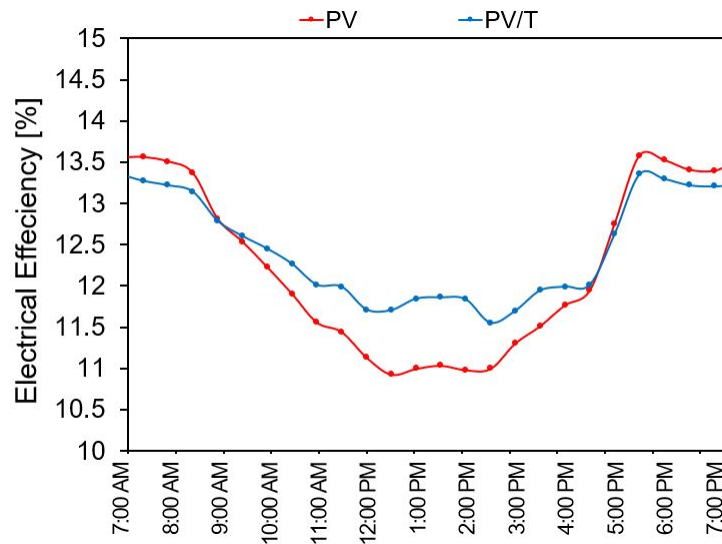


**Figure 2.6:** Comparison of the electrical efficiency of the PV/T-GSHEX system and the conventional PV system.

However, in the early hours of sunrise and sunset, the rear cooling water pocket and the insulation increase the PV surface temperature, which leads to a slight decrease in the efficiency. Anyway, in these minimum output hours, this problem isn't really severe.

### 2.2.4 GSHEX Results

The soil types considered for the present study (dry and wet) have a moisture content of 0.06 % and 24.62 %, respectively. The thermal properties of the wet

and the dry soil samples are listed in Table 2.2. Depending on the moisture content and density, the specific heat capacity was estimated following the procedures reported by Abu-Hamdeh et al. [133]. The moisture content and the thermal conductivity for both types of soil were measured by the Civil Engineering Department’s Lab in UTP.

**Table 2.2:** Soil properties used in the experiment.

Soil Properties	Wet soil	Dry soil
Density [kg/m <sup>3</sup> ]	1905	1555
Moisture Content [%]	24.62	0.06
Thermal Conductivity [W/mK]	2.08	0.21
Heat Capacity [kJ/kg K]	1.8	0.64

Based on the temperature drop of the PV/T cooling water pumped through the HEX, the heat flow transferred to the soil thermal storage is estimated by;

$$\dot{Q} = \dot{m}_w C p_w (T_{\text{HEX,in}} - T_{\text{HEX,out}}) \quad (2.1)$$

The time-dependent, stored heat flow for these two soil types is presented in Figure 2.7. From these results, the heat storage efficiency can be estimated by integrating the heat flow curves. The ratios between charge and discharge heat (the efficiency of the heat storage) for low soil thermal conductivity ( $k = 0.21$  W/mK) and high soil thermal conductivity ( $k = 2.08$  W/mK) were 40 % and 70 %, respectively. The charging and discharging rate were estimated based on the area under the curve for the daytime ( $G > 0$ ) and nighttime ( $G = 0$ ) as the following:

Energy charged to soil = Heat flow to the soil × hours of the day.

Energy discharged from soil = Heat flow from the soil × hours of the night.

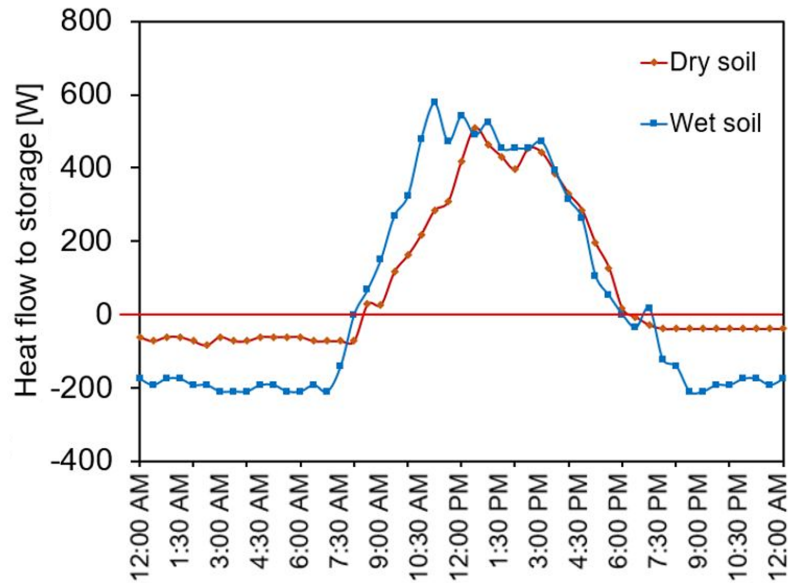


**Figure 2.7:** Heat storage for dry and wet soil, water volumetric flow rate 1.6 l/min.

Therefore it can be confirmed that the soil with high moisture content is a more suitable storage material for the task of shifting thermal energy from diurnal to nocturnal operation. Due to the much higher thermal conductivity and heat capacity this was to be expected.

## 2.3 Summary

Comparative measurements on a conventional PV and the proposed PV/T-GSHEX system have been performed. The experiments show significant benefits of the proposed system both during day and night. At noon time, the difference between the conventional PV and the thermally controlled PV/T surface temperatures was between 8 K and 10 K due to the active cooling effect of the GSHEX. In the early morning hours, the proposed PV/T-GSHEX system successfully prevented condensation. As a result, the PV/T efficiency was higher than that of the conventional PV panel. The electrical efficiency increased by 10.1 % only due to the diurnal active cooling. According to literature, the losses due to mud formation can be up to 35 % of the glass transmissivity [28].

The results also reveal that due to higher thermal conductivity and heat capacity, soil with high moisture content is much more suitable as a filling material for the GSHEX than low moisture content soil. However, both types of soil were suitable for both daytime cooling and nocturnal heating. Hence, the proposed PV/T-GSHEX system has a high potential to increase diurnal efficiency and to mitigate nocturnal dew formation.

### **3 Analysis of the Soil Temperature Distribution**

The evaluation of thermal performance in many applications connected to ground heat exchangers requires the estimation of the ground temperature, which is affected by the location, the climatic conditions and the depth [161,162]. The Soil Temperature Distribution (STD) greatly impacts the heat transfer for ground storage applications [97,98,102,104]. The higher the temperature difference between the heat transfer fluid and the soil, the higher the efficiency of the heat storage. Therefore, the estimation of STD and the depth at which the Ground Soil Heat Exchanger GSHEX should be installed are crucial to modeling and designing the PV/T-GSHEX system. Usually, numerical techniques are used to solve this kind of problems. However, they are computationally expensive and take hours of calculation time [112-116].

In the present study, an analytical model based on the Green's function method (GF) is proposed to solve the complex thermodynamic problem of STD [157]. The GF method is a basic solution of a specific differential equation with homogeneous boundary conditions [159]. The proposed analytical method can estimate a 1-D STD in a few minutes. Moreover, it can be extended to a 2-D geometry with similar computational efficiency by multiplication of the 1-D case. The convergence of series can be improved by partitioning time. The problem at hand incorporates meteorological data and the thermophysical properties of the soil. The model and the results have been published in [102]. Compared to the usual analytical methods [108-111], the GF method requires a lower level of mathematical complexity for the solution of partial differential equations. The proposed analytical model is validated with experimental data and tested for different weather conditions of two locations (Malaysia and Qatar).

### 3.1 Mathematical Modeling

Different thermal boundary conditions are applied to the ground surface (e.g. short/long wave radiation, convection and conduction through the soil layers). The ground heat transfer mechanisms are described in Figure 3.1. The formal solutions of the GF method can be written directly in terms of integrals, which can be calculated using a numerical integration method.

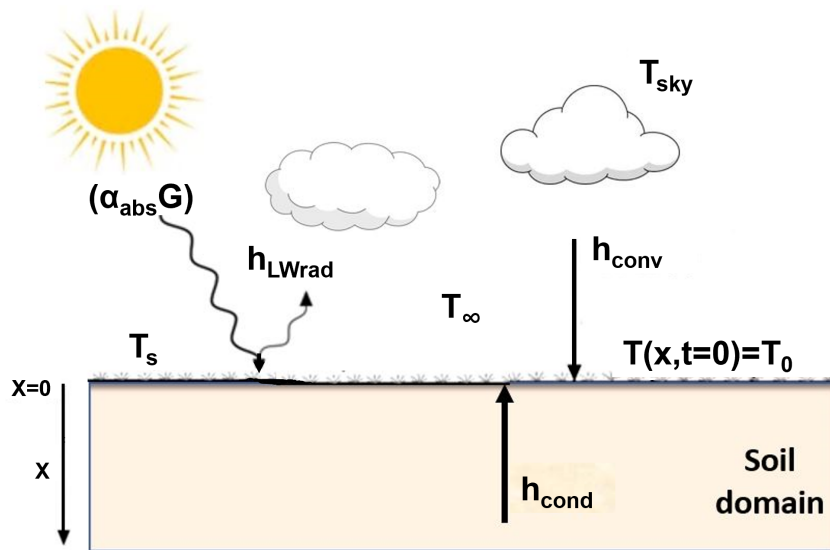


**Figure 3.1:** Power balance on the soil surface.

The STD depends on the ratio of energy absorbed during the day to energy lost at night. This is affected by the time-dependent weather conditions and the thermodynamic properties of the soil. The soil properties like thermal conductivity and heat capacity vary with the temperature and moisture content [93,105,148]. The time-dependent boundary conditions (e.g. ambient temperature  $T_\infty(t)$  and solar irradiation  $G(t)$ ) make the problem inhomogeneous. Thus, it cannot be solved using the conventional analytical methods, (e.g. the method of separation of variables).

In the present section, the GF method is applied to obtain a standard solution for such problems. It also allows considering the soil thermophysical properties.

The energy conservation equation and boundary conditions are given by [150] with

$$\rho_s(T)Cp_s(T)\frac{\partial T}{\partial t} = \frac{\partial}{\partial x} \left[ \frac{k_s(T)\partial T}{\partial x} \right], \quad (3.1)$$

the initial condition

$$T(x, t = 0) = T_0 \quad (3.2)$$

and the following boundary conditions.

For the convective heat flux, the heat transfer coefficient  $k_i$  can be determined as

$$k_i \frac{\partial T}{\partial n_i} \Big|_{x_i} = h_{\text{conv}}(T|_{x_i}(t) - T_{\infty}(t)), \quad (3.3)$$

whereas the absorption of solar irradiation is

$$k_i \frac{\partial T}{\partial n_i} \Big|_{x_i} = \alpha_{\text{ab}} G(t) \quad (3.4)$$

and the long wave-length thermal radiation heat flux is

$$k_i \frac{\partial T}{\partial n_i} \Big|_{x_i} = \varepsilon h_{\text{LWrad}}(T|_{x_i}(t) - T_{\text{sky}}(t)). \quad (3.5)$$

In the aforementioned description, the shortwave solar irradiation heat flux  $G(t)$  is obtained from the yearly weather data. For the long wave-length radiation, the heat transfer coefficient is obtained according to Larwa et al. [162] with  $h_{\text{LWrad}} = 4.83 \text{ W/m}^2\text{K}$ . Surface temperature of the soil  $T_s$  is defined at  $x_i = 0$ . For the long wave-length heat transfer,  $T_{\text{sky}}$  must be calculated.  $T_{\text{sky}}$  usually depends on the ambient temperature  $T_{\infty}$  and the dew point temperature  $T_{\text{dew}}$  and can be obtained from the following empirical correlation [156],

$$T_{\text{sky}} = T_{\infty} \left[ 0.711 + 0.0056 T_{\text{dew}} + 0.000073 T_{\text{dew}}^2 + 0.013 \cos(0.15 t) \right]^{\frac{1}{4}} \quad (3.6)$$

where  $t$  is the time since midnight expressed in hours.

In a first step, the homogeneous solution of the problem in terms of GF is obtained. Then, the problem is made homogeneous by applying an instantaneous delta source at location  $x_0$  and at time  $t_0$ . The problem is assumed to be a one-dimensional semi-infinite problem as the primary heat flux (e.g. solar irradiation) acts along the vertical direction. Heat losses in a horizontal direction are assumed to be negligible. The resultant temperature can then be expressed in terms of a homogeneous solution.

The homogeneous governing equation in terms of a GF can be written as [155]

$$\frac{\partial^2 GF}{\partial x^2} + \frac{1}{\alpha} \delta(t - t_0) = \frac{1}{\alpha} \frac{\partial GF}{\partial t}; \quad 0 < x < \infty; \quad t > 0 \quad (3.7)$$

with initial condition

$$GF(0, t | \hat{x}, \tau) = 0; \quad GF(\infty, t | \hat{x}, \tau) = 0 \cdot \quad (3.8)$$

The boundary conditions for convection and radiation on the ground surface are

$$\begin{aligned} k_i \frac{\partial GF}{\partial n_i} \Big|_{x_i} + h_{\text{conv}} GF \Big|_{x_i} &= 0 \quad \text{and} \\ k_i \frac{\partial GF}{\partial n_i} \Big|_{x_i} + h_{\text{rad}} GF \Big|_{x_i} &= 0 \cdot \end{aligned} \quad (3.9)$$

The solution of the problem on hand is the GF of this boundary value problem:

$$GF(x, t | \hat{x}, \tau) = \frac{1}{[4\pi\alpha(t-\tau)]^{\frac{1}{2}}} \left\{ \exp \left[ \frac{-(x-\hat{x})^2}{4\alpha(t-\tau)} \right] - \exp \left[ \frac{-(x+\hat{x})^2}{4\alpha(t-\tau)} \right] \right\}, \quad (3.10)$$

and

$$\frac{\partial GF}{\partial \hat{x}} \Big|_{\hat{x}} = 0 = \frac{x}{(4\pi)^{\frac{1}{2}} [\alpha(t-\tau)]^{\frac{3}{2}}} \exp \left[ \frac{x^2}{4\alpha(t-\tau)} \right] = \frac{x}{\alpha(t-\tau)} K(x, t-\tau). \quad (3.11)$$

Here, the particular form of GF for an infinite one-dimensional body, which is the fundamental heat conduction solution by Cannon [163],  $K(x - \acute{x}, t - \tau)$  is used. Two different methods can be applied to the STD problem [117-119]. In the first approach, the ground surface temperature can be applied as a boundary condition. In such cases, it is assumed that the surface temperature is a result of the power balance on the ground surface. Though this method is simplified, it requires actual measured data of the soil surface temperatures, which is not always available.

In the second approach, the surface heat fluxes can be applied as boundary conditions. The surface heat fluxes are a result of conduction, convection and radiation. Therefore, the actual weather data (air and dew point temperatures, air velocity, and solar global irradiation) is needed. This method is more accurate and easier to implement, as the actual climate data can be utilized. For the present analysis, the spatio-temporal STD was estimated based on the second approach. The STD can be obtained as a superposition of all boundary conditions as follows:

$$T(x, t) = T_0(x, t) + T_{\text{conv}}(x, t) + T_{\text{LWrad}}(\acute{x} = 0, t) + T_{\text{SWrad}}(\acute{x} = 0, t), \quad (3.12)$$

where the contribution from the initial temperature distribution of the soil is given by

$$T_0(x, t) = T_0 \int_{\acute{x}=0}^L [GF(x, t/\acute{x}, \tau)]_{\tau=0} d\acute{x}. \quad (3.13)$$

Here,  $L$  is the depth of the soil domain where the temperature profile is obtained. The contribution of the solar irradiation(short wave) is given by

$$T_{\text{SWrad}}(x, t) = \int_{\tau=0}^t \alpha_{\text{ab}} G(\tau) \frac{\alpha(\tau)}{k(\tau)} [G(x, t/\acute{x}, \tau)]_{\tau=0} d\tau, \quad (3.14)$$

while the contribution of the sky radiation (longwave) is

$$T_{\text{LWrad}}(x, t) = \int_{\tau=0}^t \varepsilon h_{\text{LWrad}} T_{\text{sky}}(\tau) \frac{\alpha(\tau)}{k(\tau)} [GF(x, t/\acute{x}, \tau)]_{\tau=0} d\tau. \quad (3.15)$$

Convection is described as

$$T_{\text{conv}}(x, t) = \int_{\tau=0}^t h_{\text{conv}} T_{\infty}(\tau) \frac{\alpha(\tau)}{k(\tau)} [GF(x, t/\acute{x}, \tau)]_{\tau=0} d\tau . \quad (3.16)$$

The resulting temperature distribution can be written in terms of initial conditions, convection and radiation:

$$\begin{aligned} T(x, t) = T_0 \int_{\acute{x}=0}^L [GF(x, t/\acute{x}, \tau)]_{\tau=0} d\acute{x} \\ + \int_{\tau=0}^t \alpha_{\text{ab}} G(\tau) \frac{\alpha(\tau)}{k(\tau)} [GF(x, t/\acute{x}, \tau)]_{\tau=0} d\tau \\ + \int_{\tau=0}^t h_{\text{conv}} T_{\infty} \frac{\alpha(\tau)}{k(\tau)} [GF(x, t/\acute{x}, \tau)]_{\tau=0} d\tau \\ - \int_{\tau=0}^t h_{\text{LWrad}} T_{\text{sky}} \frac{\alpha(\tau)}{k(\tau)} [GF(x, t/\acute{x}, \tau)]_{\tau=0} d\tau \end{aligned} \quad (3.17)$$

The integral term in the resulting solution can be numerically solved. The forced convective heat transfer coefficient is difficult to determine accurately due to fluctuating wind speed values. For this reason, an empirical correlation proposed by Kumar et al. [159] was used,

$$h_{\text{conv}} = 5.7 + 3.8 u_{\text{wind}} \quad (3.18)$$

for  $u_{\text{wind}} < 4.88$  m/s , and

$$h_{\text{conv}} = 7.2 u_{\text{wind}}^{0.78} \quad (3.19)$$

for  $u_{\text{wind}} \geq 4.88$  m/s.

## 3.2 Experimental Validation

### 3.2.1 Experimental Setup

To validate the mathematical model, an experiment was conducted to simulate a transient soil temperature profile as it can be expected in real soil conditions. The setup consisted of a cylindrical container (0.5 m height), which was insulated with Armaflex thermal insulation material and 0.4 m of the container was filled with soil. Additionally, there was an outer radiation shield to protect the insulated sidewalls of the soil container from radiation influences. For the top part of the shield, a polystyrene insulation (EPS) was used, while for the outer lateral part, extruded Polystyrene was applied. Artificial solar lamps were installed on the upper frame of the test rig. With these lamps, an irradiation heat flux of up to  $800 \text{ W/m}^2$  was applied to the soil surface at the top of the container. This value was measured with a pyranometer. Figure 3.2 shows a schematic diagram (left) and a photo (right) of the experimental setup.

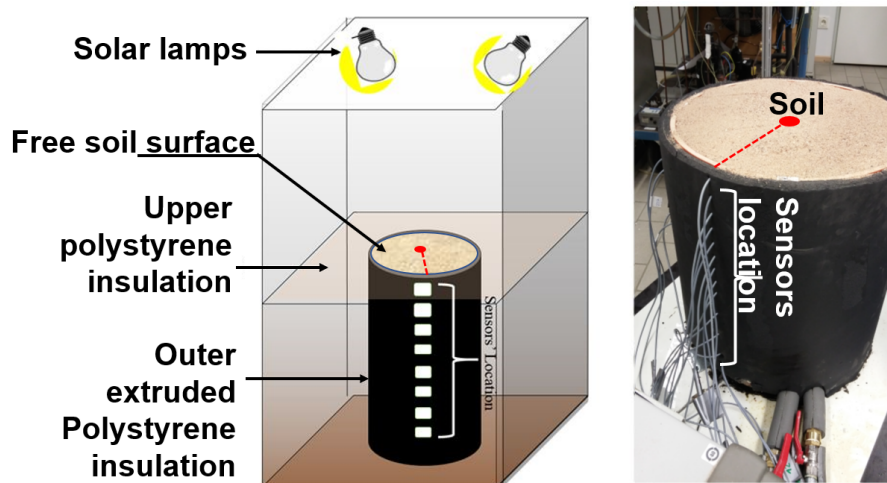


**Figure 3.2:** Schematic experimental setup (left) and photo for the soil cylinder and the arrangement of the sensors in the experiment (right).

The wall thickness of the container was 1 cm and the diameter was 41 cm. Temperature sensors were placed at the cylindrical axis of the container. For the main experiments, a laboratory thermostat was used to keep the temperature of the sand at the bottom of the container at  $\approx 26^\circ\text{C}$  constantly.

The tests were conducted as long-term heating with subsequent cooling experiments as is shown in Figure 3.3. Therefore, the lamps were turned on for eight hours. After that time, the data logger continued recording until the soil sample had almost completely cooled.

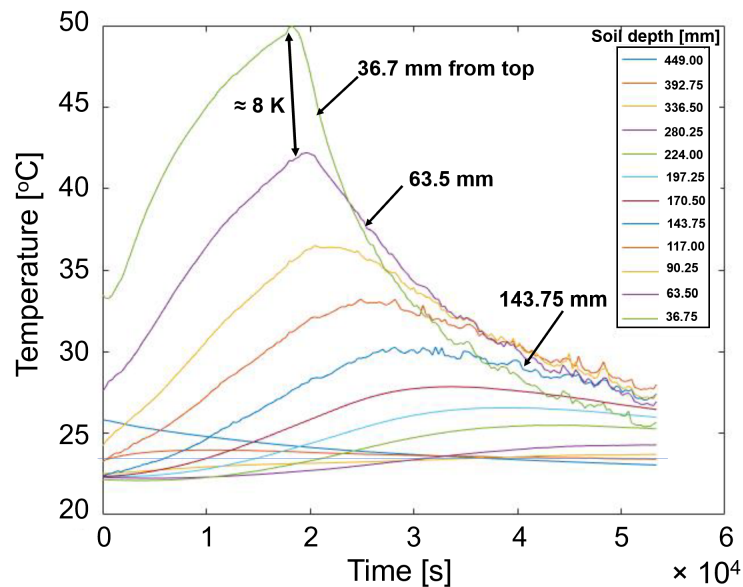


**Figure 3.3:** Results for long term heating and cooling experiments.

The temperature profile reveals that the temperature fluctuation decreases strongly with increasing depth. At a depth of 63.50 mm, the maximum temperature was around 8 K lower than that at 36.75 mm. Even though strongly damped, an increase in the temperature, which is induced by the lamps, is still measurable at a depth of 143.75 mm. After turning off the lamps, all temperatures that were influenced by the lamps decreased, and after a certain time reached an equilibrium. For the recorded time that value amounts to  $\approx 26^\circ\text{C}$ , which corresponds to the set bottom temperature. At a depth of 449 mm, the curve takes a different shape. This is due to a malfunction of the temperature sensor at this depth.

### 3.2.2 Model Validation

Figures 3.4 (a and b) show the validation of the model by experimental data at two different time steps. The abscissa represents the soil depth ( $x$ ) and the ordinate represents the soil temperature.

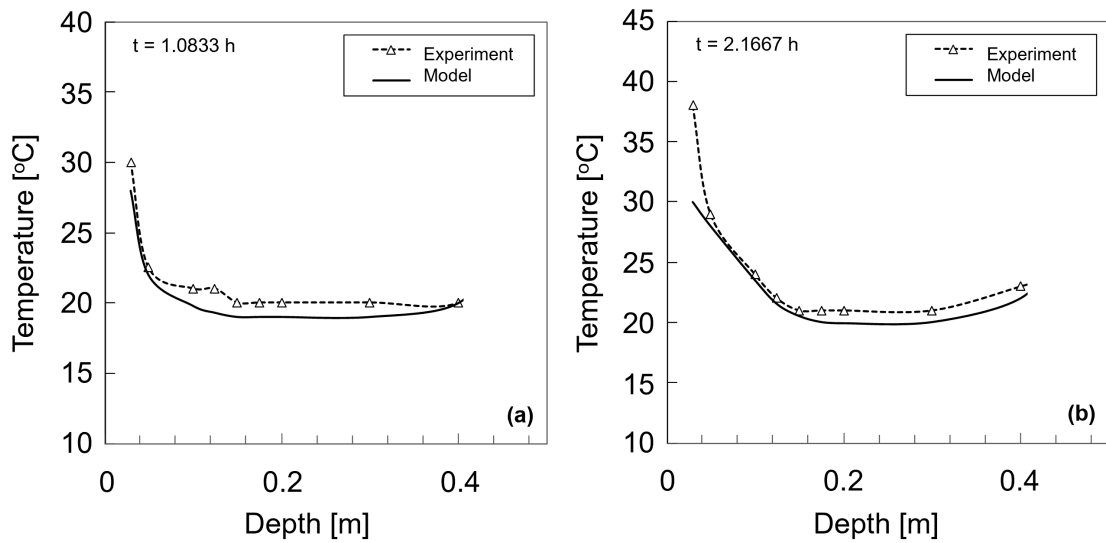


**Figure 3.4:** Comparison between experimental and simulation results after (a) 1.1 h and (b) 2.1 h test duration.

The soil physical properties used in the validation are tabulated in Table 3.1.

**Table 3.1:** Soil properties used in the experiment and applied to the model.

Soil Properties	Value
Density [ $\text{kg}/\text{m}^3$ ]	1650
Thermal conductivity [ $\text{W}/\text{mK}$ ]	0.585
Heat capacity [ $\text{kJ}/\text{kg K}$ ]	0.691

The soil temperature values at the center area ( $x = 0.2$  m) of the sample started to be stable (close to the lab ambient temperature  $\approx 22^\circ\text{C}$ ), Figure 3.4a. After around 2 hours, the temperature profile showed a similar trend as in the first operation hour. However, the experimentally determined soil temperature value at the top position of the cylinder (at  $x = 0$ ) started to increase with

increasing irradiation time, see Figure 3.4b. This can be attributed to the direct irradiation effect of the solar lamps on the thermocouples (2nd type thermocouple error) [164]. Therefore,  $T(x = 0)$  was not considered for the validation. The experimental temperature data showed some fluctuation in comparison to the model data. Even though there are some minor deviations between model and experimental results, which can be attributed to sensor calibration errors, the model shows a good agreement with the measurement data with a deviation of 4 %.

### 3.3 Application of the Model

#### 3.3.1 Case Study 1: Tropical Climate (Malaysia)

As a first case study, the STD in a tropical climate (Malaysia) was simulated. The soil properties were obtained by the laboratory facilities at UTP. Figure 3.5a shows the air and dew point temperature over a year in Ipoh, Malaysia. There are relatively small seasonal variations. The hourly global solar irradiation plotted over the year as can be seen in Figure 3.5b.

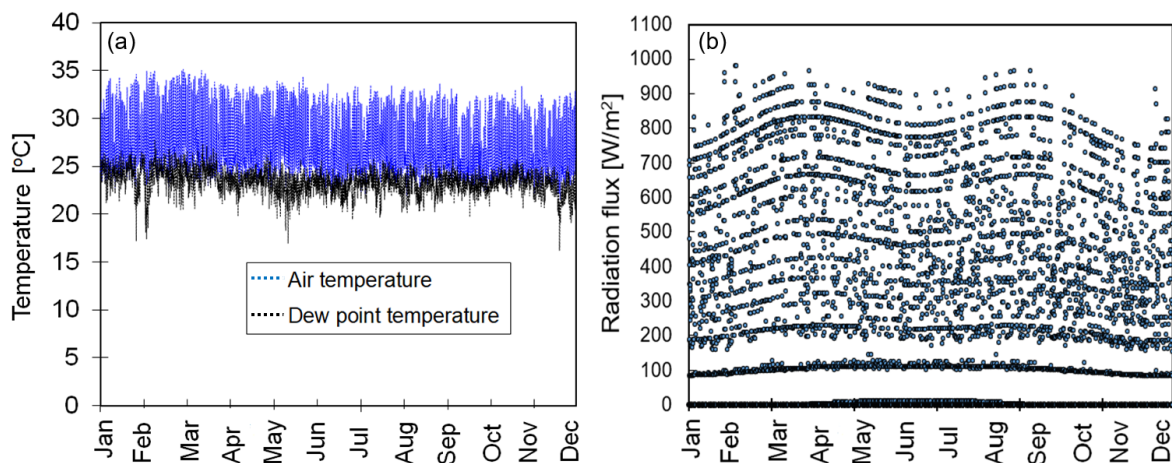


**Figure 3.5:** Meteorological data for Malaysia, (a) air and dew point temperatures, (b) solar irradiation flux in hourly values.

The solar irradiation flux fluctuates along the year with a maximum of  $900 \text{ W/m}^2$  -  $950 \text{ W/m}^2$ . This value is slightly lower than the irradiation in Qatar. However, in Malaysia, both temperature and solar irradiation are much more stable due to the tropical climate conditions. Based on the weather conditions, the soil temperature was plotted at different depths over the time span of a year. The soil properties used in the model are shown in Table 3.2.

**Table 3.2:** Soil properties used in the model, Malaysia.

Soil Properties	Value (wet,dry)
Density [ $\text{kg/m}^3$ ]	1905, 1550
Thermal conductivity [ $\text{W/mK}$ ]	2.2, 0.2
Heat capacity [ $\text{kJ/kg K}$ ]	1.8, 0.640

From the model results, the following observations can be made:

The STD for soil with high thermal conductivity,  $2.2 \text{ W/mK}$  (high moisture content 24 %) is fluctuating by 4-5 K at 1 m depth as can be seen in Figure 3.6.

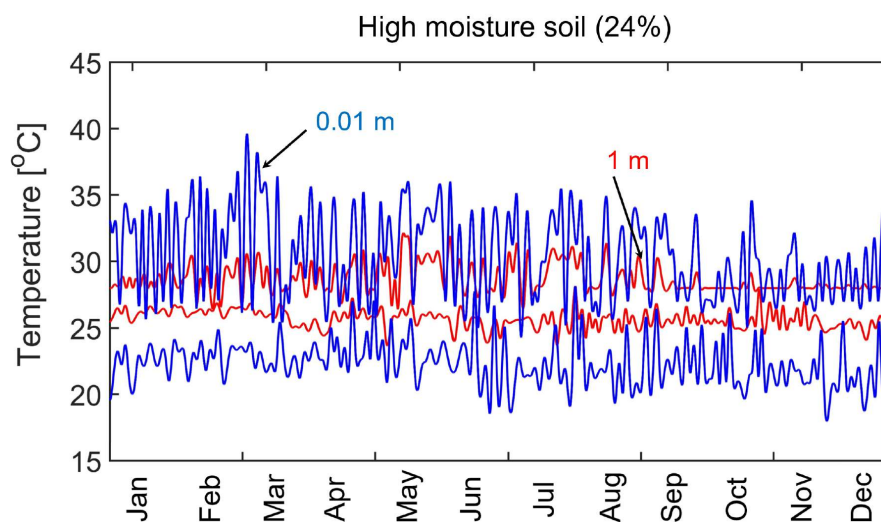


**Figure 3.6:** Annual STD at 0.01 m and 1 m depth for soil with high moisture content (24 %) and thermal conductivity  $2 \text{ W/mK}$ , Malaysia.

The STD is shown by an envelope function encompassing daily maximum and minimum temperatures. However, for a depth of 0.01 m, the soil temperature fluctuates by 13-14 K during the summer season. During the winter season, the soil temperature fluctuates by 10-11 K.

In Figure 3.7, the annual STD was again plotted. Now, soil with low thermal conductivity 0.2 W/mK (dry soil), see Table 3.2, was compared to the STD of the soil with high thermal conductivity 2 W/mK (wet soil) at 1 m depth. The black lines represent the STD for the dry soil while the red lines represent the STD for the wet soil.

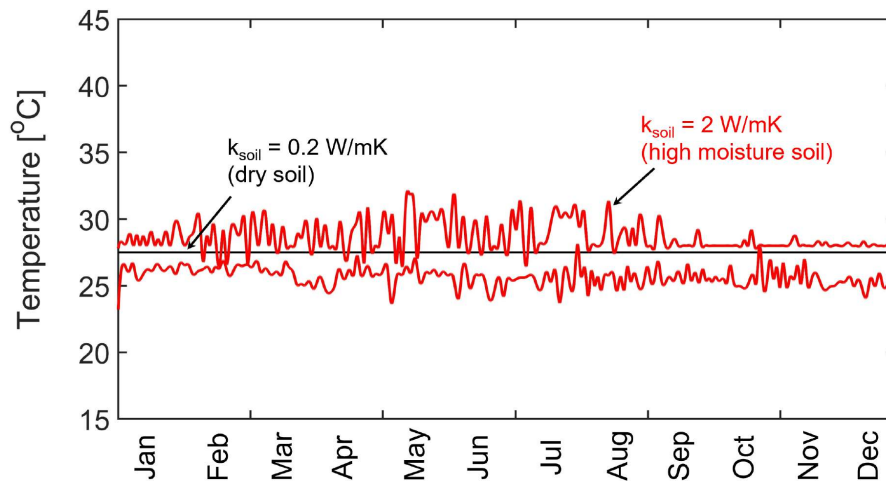


**Figure 3.7:** Annual STD at 1 m depth for high (2 W/mK) and low (0.2 W/mK) soil thermal conductivity, Malaysia.

It can be observed that the average temperature of the soil with low thermal conductivity 0.2 W/mK (dry soil) is almost constant after 1 m for all time. Therefore, it can not be distinguished between the two black lines, as the fluctuations are very low. However, the soil temperature fluctuates at the same depth for soil with high thermal conductivity 2 W/mK (wet soil) what was to be expected. It can be concluded that both soil properties and weather conditions significantly affect the STD over the year.

### 3.3.2 Case Study 2: Semi-desert Climate (Qatar)

For the second case study, the model is applied to investigate the yearly STD in semi-desert climate conditions, e.g. Qatar. The corresponding weather data was obtained from the Qatar Environmental and Energy Research Institute (QEERI) in Doha [8], see Figure 3.8.

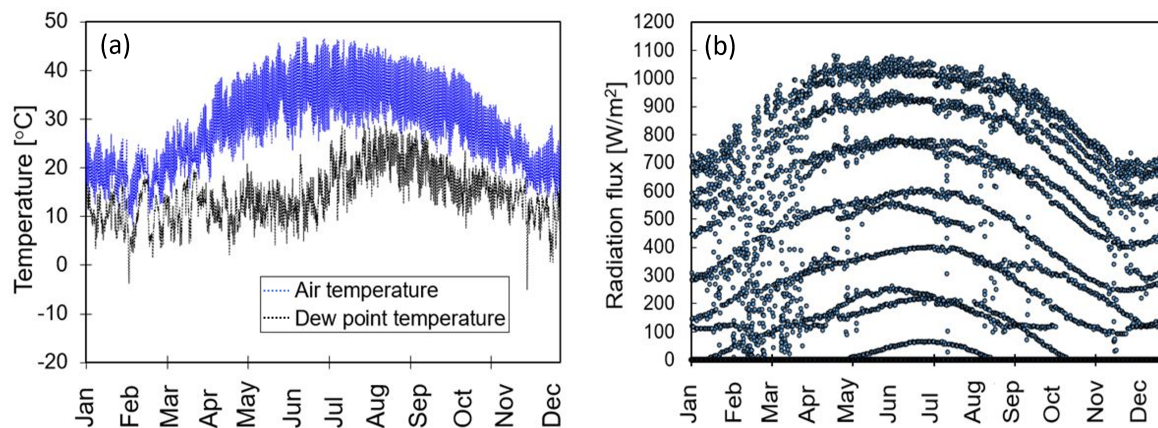


**Figure 3.8:** Meteorological data for Qatar, (a) air and dew point temperatures, (b) solar irradiation flux in hourly values.

As is shown in Figure 3.8a, the air dry and dew point temperatures are increasing during the summer season. The temperature of the air is maximal during July and August where it is as high as 45°C. The dry and dew point temperatures are important to estimate the sky temperature. The solar irradiation (short wave radiation) is shown in Figure 3.8b. It shows hourly values, which in turn form curves. This is due to the daily and seasonal fluctuation of the solar irradiation. The yearly ambient temperature and wind velocity are the input for the convection heat transfer part of the model, see equations (3.3), (3.18) and (3.19). The irradiation flux and the dew point temperature are necessary to estimate the short/long wave-length radiation gain and losses. The soil physical properties used in the model are given in Table 3.3.

**Table 3.3:** Soil properties used in the model, Qatar.

Soil Properties	Value
Density [kg/m <sup>3</sup> ]	1400
Thermal conductivity [W/mK]	0.8
Specific heat [kJ/kg K]	0.820

Figure 3.9a shows the annual simulation of the transient soil temperature at different depths for Qatar.

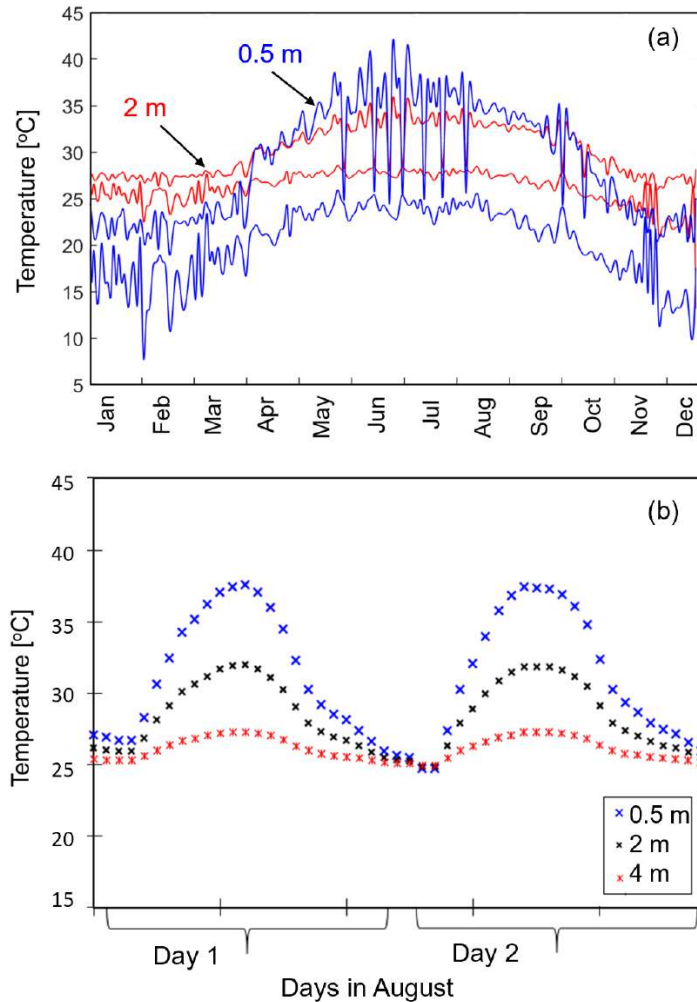


**Figure 3.9:** (a) Annual STD at 0.5 m and 2 m depth (b) STD fluctuation for two selected days in August, Qatar.

The results are shown by an envelope function, which encompasses daily maximum and minimum temperatures. The soil temperature fluctuates significantly ( $\approx 7$  K) near the surface (at 0.5 m) and begins to stabilize ( $\approx 1$  K fluctuation) at a depth of 2 m in the winter season (from December to February). However, greater depth that may reach 4 m is needed during the summer season (from May to October). For further clarification, two days of August were chosen and are presented in Figure 3.9b, to illustrate the results during the summer period at different depths (0.5 m, 2 m and 4 m), which show soil temperature fluctuations around  $\approx 10$  K, 5 K, 1 K respectively.

The model was applied for Malaysia at the same depths (0.5 m and 2 m) which are previously used for Qatar to compare the annual simulation of the STD for tropical and desert climates at the same depths as can be seen in Figure 3.10. In contrast to Qatar, soil temperature fluctuates much less ( $\approx 1$  K) at a depth of 0.5 m, and it stabilizes ( $\approx 0$  K) at a depth of 2 m throughout the year.

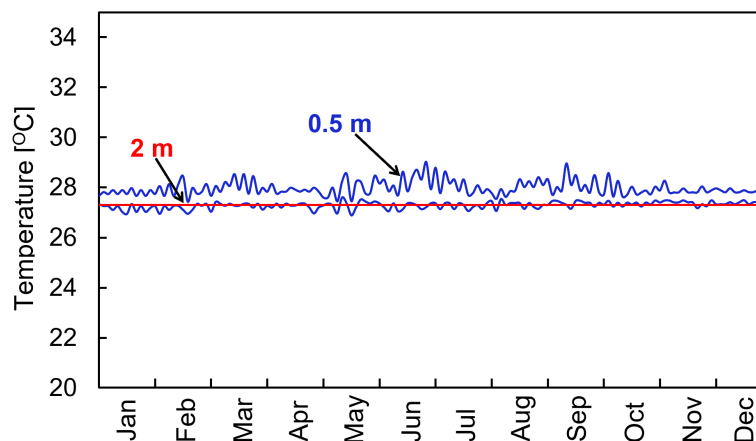


**Figure 3.10:** Annual STD for Malaysia at 0.5 m and 2 m depths.

From these results, the following observations can be made:

- The depth at which the soil reaches thermal equilibrium depends on the climate and the thermophysical properties of the soil. Both depend on the geographic location.
- The soil temperature over the year follows two trends. Firstly, the soil

temperature increases and decreases over the year according to seasonal variations. Secondly, the temperature of the soil is also fluctuating in correspondence to daily air temperature and irradiation fluctuations.

- Irradiation heat flux is the main heat transfer mechanism affecting the soil temperature. This can be inferred from the similarity of the annual curve trend for solar irradiation and soil temperature (Figures 3.8b and 3.9a).

Under tropical weather conditions, a constant soil temperature can be found at a depth closer to the surface than under extreme weather locations. Therefore, the weather conditions and the soil properties should be taken into consideration to evaluate the installation depth of the ground heat exchanger.

### 3.4 Advantages of the Model

The GF-based method provides a much more straight forward way to solve the problem considering all weather parameters. Figure 3.11 shows the numerical solution obtained with ANSYS Fluent for a 7-days STD.

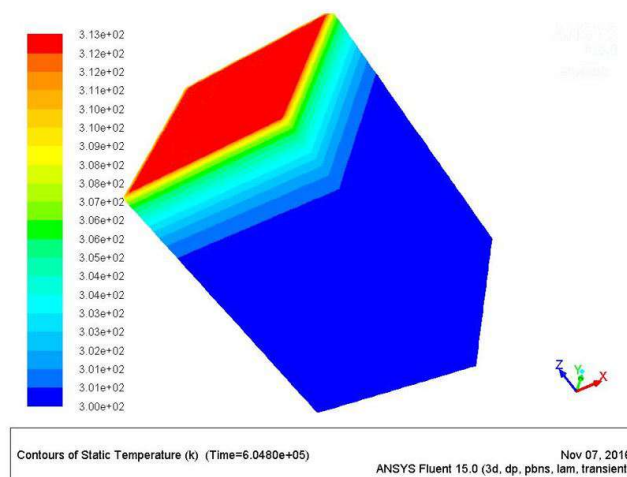


**Figure 3.11:** CFD solution for the STD problem.

Running this case took a few hours, which means it will need approximately one week to run an annual case. Using to the GF model, the annual case needs much less time to get the results. A comparison of the computational time needed for an annual run is displayed for standard numerical solutions (obtained with ANSYS Fluent and COMSOL Multiphysics) and the GF solution in Figure 3.12. It can be seen that the presented GF model is more efficient as it can solve for the particular point of interest, while the numerical models require meshing and have to reach steady state conditions. Considering computational time, the GF model is a hundred times faster than the numerical models.

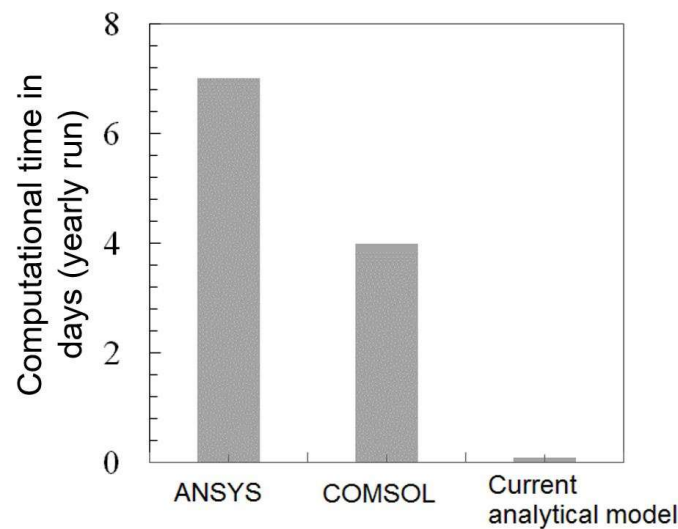


**Figure 3.12:** Computational time for the GF analytical model in comparison to numerical solutions (ANSYS and COMSOL).

### 3.5 Summary

In the present study, a Green's function method (GF) is presented to solve the soil temperature distribution (STD) problem. From real-time meteorological data sets, the model can estimate the daily and annual STD at different depths.

The model is also allowing for time-dependent thermophysical soil properties, e.g. due to varying moisture content.

The modeled soil temperature (in°C) was compared with the experimentally determined values and showed a deviation of only 4 %. It was found that the soil temperature is almost constant close to the surface under tropical weather conditions in contrast to desert weather conditions, where a depth of  $\approx 4$  m is required. The depth at which the soil temperature starts to stabilize also depends on the soil thermal properties (moisture content, thermal conductivity and heat capacity). The significant advantage of the presented analytical model is the computational cost, which is a hundred times lower than that of numerical models. The obtained soil temperature is an input parameter to the PV/T-GSHEX model.

## **4 Modeling of the PV/T-GSHEX System**

In the present chapter, a mathematical model of the PV/T-GSHEX system is presented. The model was built up using the MATLAB/Simulink platform to investigate the diurnal and nocturnal performance of the PV/T-GSHEX system for different weather and operational conditions. The model and the results were published in [102,103]. Two real-time weather data sets were applied: firstly, tropical climate as in Malaysia and secondly, semi-desert climate as in Qatar. The mathematical model was experimentally validated with the outdoor experiment results, which were presented in Chapter 2. Then, a parametric analysis on the PV/T-GSHEX system was performed.

### **4.1 Development of the Mathematical Model**

As a reference, an individual PV panel and the integrated PV/T-GSHEX systems were modeled. The model was based on the actual size and parameters of the PV/T-GSHEX in the experimental setup. The layout of the PV/T-GSHEX system and the incorporated heat fluxes are shown in Figure 4.1. The PV/T was modeled as a compound consisting of several layers including: glass, EVA foil (an Ethylene Vinyl Acetate film used to encapsulate the PV cells), PV cells, Tedlar foil (a composite layer film used as water-vapor tight cover on the back of the encapsulated PV cells), and a water layer as a heat transfer fluid. The water is flowing inside an aluminum pocket, which was connected to the backside of the PV panel. The aluminum water pocket was filled with a porous material to improve the heat transfer and it was insulated from the backside to reduce the heat losses from the water pocket to the environment.

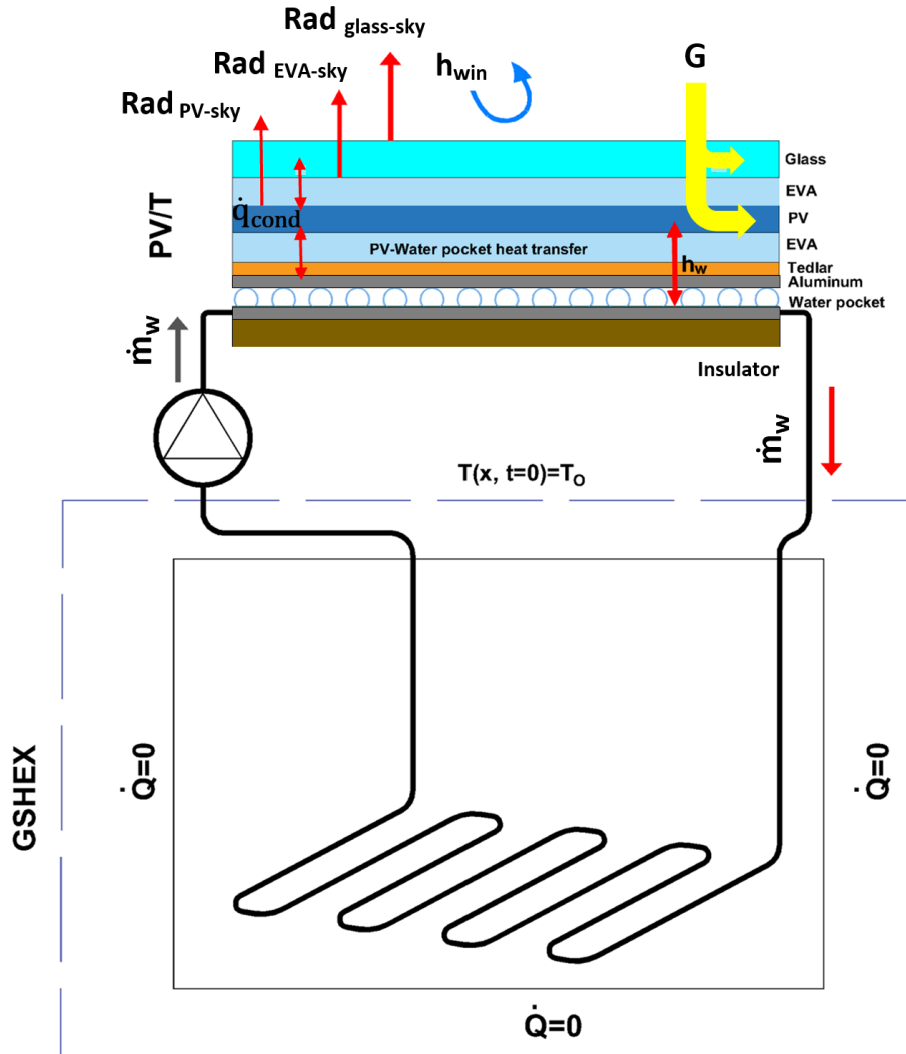


**Figure 4.1:** Layout of the PV/T layers and heat flow through the PV/T-GSHEX system.

For Malaysia, the GSHEX was installed at a depth of 0.8 m. Taking into account the results from the STD model (see section 3.3), the temperature of the soil around the pipe at this depth was assumed to be constant.

According to the experimental results, the highest temperature difference between the water and the ambient air was obtained. Then, the value of the heat conduction through the insulation layer was calculated and compared to the value of the maximum heat load inside the water pocket. The ratio of these two values was small  $\approx 0.36\%$ . Therefore, the small temperature gradient through the insulation layer can be neglected.

### Modeling Assumptions:

The assumptions used to simplify the mathematical model are as follows:

1. The thermal properties of materials are independent of temperature.
2. The fluid properties are calculated from the previous iteration as a function of the fluid temperature.
3. The PV and PV/T panels are assumed to be clean.
4. At all given weather conditions, the PV and PV/T panels operate at their maximum power point (MPP).

### Modeling the PV Panel

A PV panel is composed of many electrically connected solar cells. The solar cells are connected in a specific configuration, where the number of solar cells consists of the number of cells connected in series to a cell string multiplied with the number of strings. The  $I$ - $V$  curve of the PV panel is given by the superposition of the PV cells' diode curves generated by the incident solar irradiation. The power can be calculated from the  $I$  -  $V$  equation, e.g. Duffie et al. [32],

$$P = \left( I_{pvn} - I_0 \cdot \left( \exp \left( \frac{(V + I \cdot R_s)}{\frac{V_t}{\frac{N_s}{a}}} \right) - 1 \right) - \frac{V + I \cdot R_s}{R_p} \right) \cdot V \quad (4.1)$$

where  $I_{pvn}$ ,  $I_0$ ,  $R_s$ ,  $R_p$ ,  $V_t$  and  $a$  are nominal light-generated current, diode saturation current (nominal), series resistance, parallel resistance, thermal junction voltage (nominal) and diode constant, respectively. As a result, the electrical efficiency can be obtained by

$$\eta_e = \frac{P}{A_{pV} G} \quad (4.2)$$

Where,  $A_{PV}$  and  $G$  are the surface area of the PV panel and the global solar irradiation respectively.

## 4.2 Modeling of the PV/T System:

Modeling of the PV/T panel include the electrical properties and the heat transfer within the PV/T module including the PV panel, the backside cooling pocket and the GSHEX. The thermal model evaluates thermal parameters such as the PV surface temperature  $T_{PV}$ , mean water temperature in the pocket  $T_{w,mean}$ , and thermal gain  $\dot{Q}_{gain}$ . The thermal simulation of the PV/T is based on [41, 55, 56]. The net thermal gain can be obtained as a result of the absorbed solar irradiation by the PV cells  $\dot{Q}_{PV}$ , the convective heat losses  $\dot{Q}_{conv}$ , the long wave heat losses  $\dot{Q}_{LWrad}$  and the electrical power  $P$  as the following,

$$\dot{Q}_{gain} = \dot{Q}_{PV} - \dot{Q}_{conv} - \dot{Q}_{LWrad} - P \cdot \quad (4.3)$$

The input variables to the simulation (which are used in the validation) are the measured values in the experiment, including the global irradiance  $G$ , water mass flow rate  $\dot{m}_w$  ambient temperature  $T_\infty$  and wind velocity  $u_{wind}$ . For the annual run and parametric study, these variables are taken from the weather data.

The incident solar irradiation on the PV module is transmitted through the PV glass cover. Part of it is absorbed by the glass. The remaining radiation is transmitted to the PV cell, where it is partially absorbed. Reflection on the glass and the solar cell, as well as absorption and reflection on the front EVA layer were negligible as the refractive index is similar and the EVA layer is very thin [56]. With this assumption, the solar irradiation absorbed by the PV cells,  $\dot{Q}_{PV}$  is:

$$\dot{Q}_{PV} = A_{PV} G (\alpha_{ab} \tau_{glass}). \quad (4.4)$$

Part of the absorbed solar irradiation is converted into electrical power  $P$ .

Since the temperature of the glass cover is higher than the ambient temperature for  $G > 0$ , re-emission is occurring. Equation (4.5) describes the radiative heat transfer between the sky at a temperature  $T_{\text{sky}}$  and the glass surface at a temperature  $T_{\text{glass}}$ .

$$\dot{Q}_{\text{LWrad}} = \sigma \varepsilon_{\text{glass}} A_{\text{PV}} (T_{\text{PV}}^4 - T_{\text{glass}}^4). \quad (4.5)$$

$T_{\text{sky}}$  can be predicted by the correlation listed in Duffie et al. [157],

$$T_{\text{sky}} = T_{\infty} (0.711 + 0.0056 T_{\text{dew}} + 0.000073 T_{\text{dew}}^2 + 0.013 \cos(15 t))^{1/4}. \quad (4.6)$$

Where  $t$  is the hour of the day, after midnight. According to Spinnler et al. [165], this correlation gives accurate results.

The expressions for calculating the PV temperature  $T_{\text{PV}}$ , backside temperature  $T_{\text{bs}}$  and the mean water temperature  $T_{\text{w,mean}}$  are obtained from the energy balance [41,56] given by equations (4.7), (4.8) and (4.10), respectively.

$T_{\text{PV,mean}}$  is calculated by

$$T_{\text{PV,mean}} = \frac{(\alpha_{\text{ab}}\tau) + U_{\text{T}}T_{\infty} + T_{\text{bs}}}{U_{\text{t}} + U_{\text{T}}}, \quad (4.7)$$

where  $U_{\text{T}}$  and  $U_{\text{t}}$  are the overall heat transfer coefficient from Tedlar to water and from cell to ambient through glass respectively.

$T_{\text{bs}}$  is calculated by

$$T_{\text{bs}} = \frac{(\alpha_{\text{ab}}\tau)G + U_{\text{T}}T_{\infty} + h_{\text{w}}T_{\text{w}}}{U_{\text{t}} + h_{\text{w}}}, \quad (4.8)$$

where  $h_{\text{w}}$  is the convective heat transfer between water in the pocket and the module backside plate. The conductive resistance from the cell back side to the flowing water in the pocket, through the Tedlar foil,  $U_{\text{T}}$  is given by:

$$U_{\text{T}} = \frac{1}{\frac{L_{\text{Al}}}{k_{\text{Al}}} + \frac{L_{\text{T}}}{k_{\text{T}}}} \quad (4.9)$$

where,  $L_{Al}$  is the thickness ( $1 \times 10^{-3}$  m) and  $k_{Al}$  is the thermal conductivity of aluminum (236 W/mK).  $L_T$  and  $k_T$  are the Tedlar thickness and thermal conductivity ( $0.38 \text{ m} \times 10^{-3}$  and 0.24 W/mK) respectively.

The mean water temperature,  $T_{w,\text{mean}}$  in the pocket is predicted using equation (4.10),

$$T_{w,\text{mean}} = \left( T_{\infty} + \frac{(\alpha_{ab}\tau) G}{U_{\text{glass},T}} \right) \left\{ 1 - \exp \left[ \frac{1 - \left( \frac{-FU_{\text{glass},T}A_{PV}}{\dot{m}Cp} \right)}{A_{PV}U_{\text{glass},T}/\dot{m}Cp} \right] \right\} + T_w \left[ \frac{1 - \left( \frac{-FU_{\text{glass},T}A_{PV}}{\dot{m}Cp} \right)}{U_{\text{glass},T}A_{PV}/\dot{m}Cp} \right], \quad (4.10)$$

where  $U_{\text{glass},T}$  is the overall heat transfer coefficient from glass to Tedlar through the cell installation [41].

The convective heat transfer coefficient  $h_{\text{wind}}$  between the glass surface and the ambient due to wind can be estimated by a correlation recommended by Geoola et al. [35],

$$h_{\text{wind}} = \frac{0.86 \cdot \rho_a \cdot Cp_a \cdot u_{\text{wind}}}{\sqrt{(u_{\text{wind}} \cdot 2 \cdot A_{PV} \cdot \frac{\rho_a}{\mu_a})}}. \quad (4.11)$$

The values of the wind speed,  $u_{\text{wind}}$  are adopted from the experimental measurements and from the annual weather data and used as an input to the validation and the annual simulation. Then, the heat loss from the PV surface to the ambient, by forced convection,  $\dot{Q}_{\text{conv}}$  is:

$$\dot{Q}_{\text{conv}} = A_{PV} h_{\text{wind}} (T_{PV,\text{mean}} - T_{\infty}). \quad (4.12)$$

The thermal simulation of the water pocket, which is similar to a heat exchanger, is carried out considering the porous filling material. The heat exchange between the PV backside and the water pocket  $\dot{Q}_w$  is given in equation 4.13:

$$\dot{Q}_w = A_{PV} h_w (T_{w,\text{mean}} - T_{PV,\text{mean}}) \cdot \quad (4.13)$$

Where,  $h_w$  is the convective heat transfer coefficient of the water inside the pocket as a function of the Nusselt number (Nu).

$$h_w = \frac{\text{Nu } k_w}{d_h}, \quad (4.14)$$

where  $d_h$  is the hydraulic diameter of the water pocket. Nu for water flow through a porous material, as a function of Re, is suggested by Dukhan et al. [147], as

$$\text{Nu} = 5.91 \text{Re}^{0.53}, \quad (4.15)$$

where

$$\text{Re} = \frac{u_w d_h \rho_w}{\mu_w}. \quad (4.16)$$

$T_{PV,\text{mean}}$  and  $T_{w,\text{mean}}$  can be determined from equations (4.7) and (4.10), respectively.

### 4.3 Ground Soil Heat Exchanger (GSHEX)

On a daily basis, the heat flux from the soil to the HEX  $\dot{q}_{s\text{-HEX}}$  is negative during the day time (charging) and positive during the night time (discharging). On an annual basis, generally it is negative during the summer season and positive during the winter season. The soil heat flux is calculated as

$$\dot{q}_{s\text{-HEX}} = h_w(T_s - T_{w,\text{mean}}) = \frac{1}{A_{\text{coil}}} \dot{m}_w C p_w (T_{w,\text{out}} - T_{w,\text{in}}). \quad (4.17)$$

Where  $T_{w,\text{out}}$  and  $T_{w,\text{in}}$  are the water inlet and outlet temperatures of the heat exchanger and  $h_w$  is the reciprocal of the total thermal resistance between the water in the heat exchanger coil and the soil,  $R_w$ ,

$$h_w = \frac{1}{R_w}. \quad (4.18)$$

With the assumption that  $T_{w,\text{mean}} = (T_{w,\text{out}} + T_{w,\text{in}})/2$ , equation (4.17) permits the prediction of the water outlet temperature from the GSHEX, as

$$T_{w,\text{out}} = \frac{1}{\dot{m}_w C p_w + \frac{1}{2R_w}} \cdot \left[ T_s \left( \frac{1}{R_w} \right) - T_{w,\text{in}} \left( \frac{1}{2R_w} - \dot{m}_w C p_w \right) \right]. \quad (4.19)$$

## 4.4 Results and Discussion

In the present section, the results of the simulation are discussed. The simulation was performed to investigate diurnal cooling and nocturnal dew mitigation on the solar glass surface by the PV/T-GSHEX system. In the first subsection, the model is validated with the outdoor experimental data. In the second subsection, the annual performance of the proposed system is investigated. Therefore, a parametric analysis for different sets of weather data for different locations and different soil types is performed.

### 4.4.1 Validation of the PV/T-GSHEX Model

In order to validate the developed mathematical simulation model, the predicted panel temperatures were compared to the measured temperatures, as shown in Figure 4.2, where (a) is the day time and (b) is the night time.

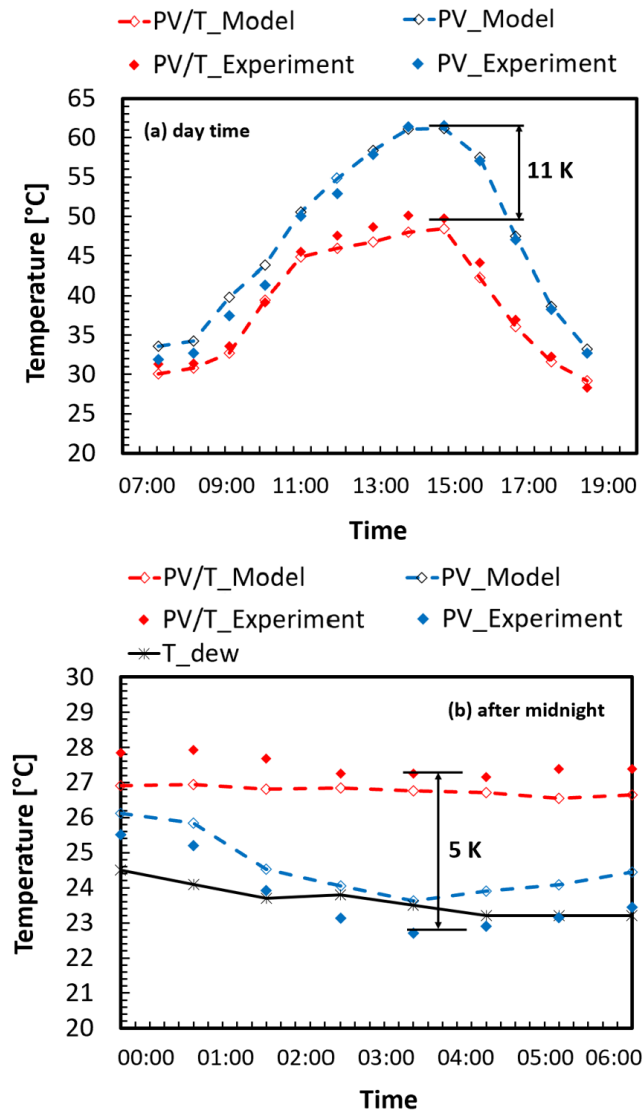


**Figure 4.2:** Validation of the PV/T-GSHEX model by comparison of measured and simulated surface temperatures of: (a) daytime and (b) night-time.

Compared to the measurement values, the maximum relative error for the simulated temperature is 5.7 % for the conventional PV and 4.5 % for the PV/T in terms of °C. The simulation slightly overestimates the PV surface temperature, with a mean relative error of 2.6 %. On the other hand, the simulation is underestimating the PV/T surface temperature with a mean relative error of 3.2 %. This is due to neglecting natural convection at the rear side of the PV/T panel, which also slightly influences the calculated surface temperatures.

However, in general, the margin of error is acceptable and thus the simulation model is considered to be of sufficient accuracy for the further considerations.

#### 4.4.2 Weather Scenarios with Dew Formation Propensity

The simulation was conducted using weather data collected from the Solar Research Site at UTP and from Doha, Qatar. Figure 4.3 shows the calculated yearly temperature differences between the conventional PV modules' surface temperature  $T_{PV}$  and the dew point temperature  $T_{dew}$  for both locations. Since the condensation occurs when the PV surface temperature is lower than the dew point temperature, the negative values of the temperature difference ( $T_{PV} - T_{dew}$ ) in Figure 4.3 are representing the conditions favorable for the onset of condensation. These are the values below the horizontal red line.

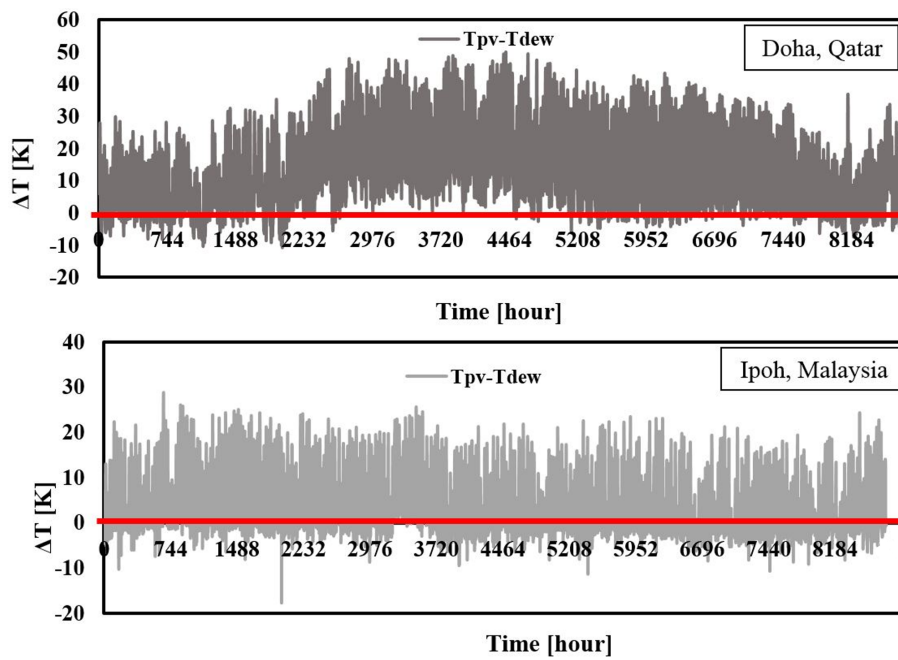


**Figure 4.3:** Hourly simulated conventional PV surface and dew point temperature difference.

It can be seen that the probability of daily occurrence of condensation is higher in Malaysia ( $\approx 1500$  hours) than in Qatar ( $\approx 500$  hours) due to more nights with  $T_{dew} > T_{PV}$ .

### 4.4.3 Annual Prediction of PV and PV/T Temperatures

Annual simulation results of the PV and the PV/T temperatures for both locations (Malaysia and Qatar) are shown in Figures 4.4 and 4.5, respectively. The results in Figure 4.4 show a good performance of the proposed PV/T-GSHEX system for Malaysia's weather conditions. The PV cells are protected from overheating by reducing the diurnal PV/T surface temperature. Looking at the noontime behavior throughout the year, a maximum reduction of surface temperature by up to 15 K can be achieved by the PV/T-GSHEX system.

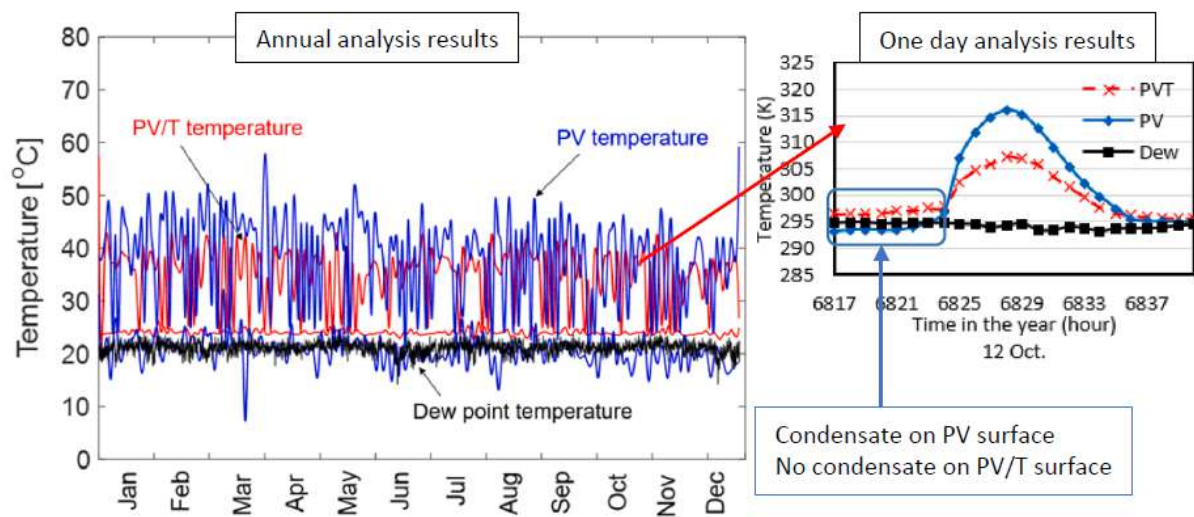


**Figure 4.4:** Annual simulated PV and PV/T surface temperatures for Malaysia.

However, the results show that the PV/T surface temperature becomes higher than the PV temperature in some hours in the second half of the year. The reason could be attributed to the higher temperature of the soil than the temperature of the ambient air due to storage effects. It could be also due to fluctuating cloud index, which makes the GSHEX operate as a heating instead of a cooling system. This counterproductive behavior is even more distinct in the annual results of Qatar during some early days in November and December. Figure 4.5 shows the annual performance of the PV/T-GSHEX system for Qatar's weather conditions.

Nevertheless, as the ambient temperature is low at this time of the year, the PV/T temperature will not exceed  $35^{\circ}\text{C}$ , which is in the range of the  $\text{NOCT} \approx 47^{\circ}\text{C}$ . Therefore, the performance of the system will not be severely affected.

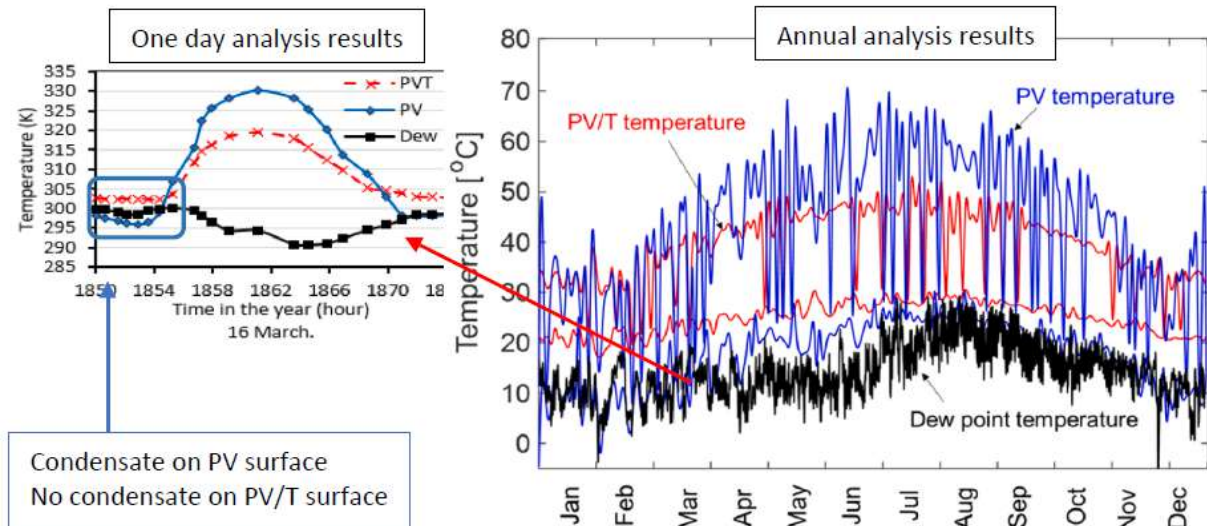


**Figure 4.5:** Annual simulated PV and PV/T surface temperatures for Qatar.

Interestingly, sometimes, the GSHEX cools the PV/T solar panel below the dew point temperature. Having analyzed this behavior, a controlled water flow rate in the system is strongly recommended.

#### 4.4.4 PV Performance Enhancement

##### Diurnal Temperature Management

Surface temperature results from simulation and measurement are presented in Figures 4.2a, 4.4 and 4.5 for both PV and PV/T modules. The results show a good performance for the cooling effect with a surface temperature difference of  $\Delta T \approx 11 \text{ K}$  during the day between PV and PV/T.

### **Nocturnal Condensation Management**

During the condensation period, 3:30 AM to around 7:30 AM, the proposed system demonstrates its ability to retain the PV/T panel surface temperature 2-5 K above the dew point temperature. This temperature difference is sufficient to prevent dew formation. In contrast, the PV surface temperature is lower than the dew point temperature over the same period of time. Hence, water vapor from the air is likely to condense on the surface of the conventional PV panel. This was already presented in Figures 4.2b, 4.4 and 4.5.

The system can reduce the annual overheating hours of the PV panel by  $\approx 98\%$ , which enhances the system performance by  $\approx 10\%$ - $11\%$ . The system can also reduce the annual condensation hours by  $93\%$ , which avoids solar glass transmittance losses that can be as high as  $35\%$  [28]. The number of hours of overheating and condensation will be shown in section 4.4.4. The secondary enhancement is to reduce the degradation of the PV panel and increase its lifespan, which can not be quantified in the present study.

#### **4.4.5 Meteorological Parameter Analysis**

The PV/T-GSHEX performance is examined for different cases; in every case, one of the weather parameters is changed while the other parameters remain constant.

#### **Effect of Wind Speed**

Figure 4.6 shows the effect of wind velocity on the PV/T-GSHEX panel surface temperature. When the wind velocity is increasing from 2 to 12 m/s, PV glass temperature is cooling down from  $31.6^{\circ}\text{C}$  to  $28.7^{\circ}\text{C}$  during the day and from  $19.6^{\circ}\text{C}$  to  $19.2^{\circ}\text{C}$  during the night. For every 4 m/s rise in wind velocity, the PV glass temperature is reduced by 1.2 K during daytime.

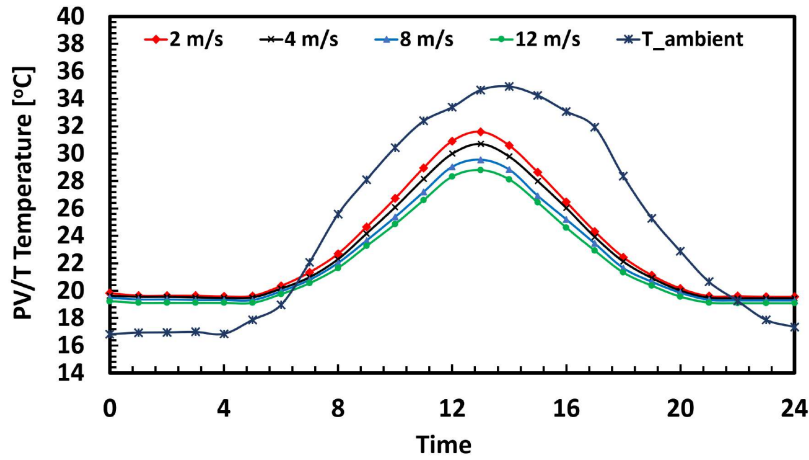


**Figure 4.6:** Simulated PV/T surface temperature for different wind velocities.

For every 4 m/s rise in wind velocity, the glass temperature is reduced by 0.3 K during the night-time. This indicates that the influence of the wind velocity is limited and the effect of longwave radiative cooling is dominating the PV temperature during this time.

### Effect of Ambient Temperature

In Figure 4.7, the effect of ambient air temperature  $T_{\infty}$  on the system surface temperature is presented.

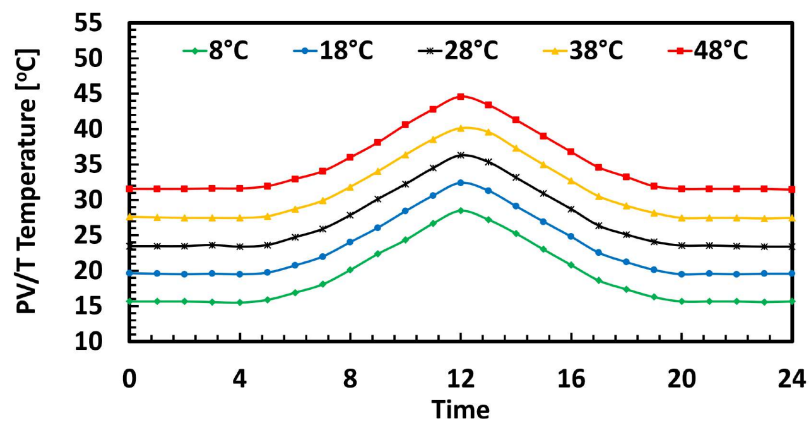


**Figure 4.7:** Simulated PV/T surface temperature for different ambient temperatures.

For air temperatures increasing from 8°C to 48°C, the nocturnal glass surface temperature  $T_{\text{glass}}$ , is increasing from 15.7°C to 31.8°C and the PV glass temperature increasing from 28.4°C to 44.6°C. For every 10 K rise in  $T_{\infty}$ ,  $T_{\text{glass}}$  increases by 4 K. This increment in the PV glass surface temperature is due to the heat exchange of the glass with the surroundings through convection as well as radiation from and to the atmosphere with  $T_{\text{sky}} = f(T_{\infty})$  [82].

### Effect of Dust Layers

A layer of dust was added to the surface of the PV glass to investigate the effect of soiling glass on the PV surface temperature. The thickness of the dust is assumed as 1 mm with thermal conductivity 0.2 W/mK, and emissivity 0.8 [76]. The results indicate that the temperature of the PV surface is slightly higher than that of the clean PV panel by maximum increment 0.9 K during the day as can be shown in Figure 4.8. This increment is due to conductive thermal resistance of the dust layer and the lower longwave radiation with  $\varepsilon \approx 0.8$  in comparison to that of the clean glass  $\varepsilon \approx 0.95$ . This indicates that the PV/T-GSHEX can also sufficiently work under the soiling conditions and no additional heat storage is needed to prevent the condensation.

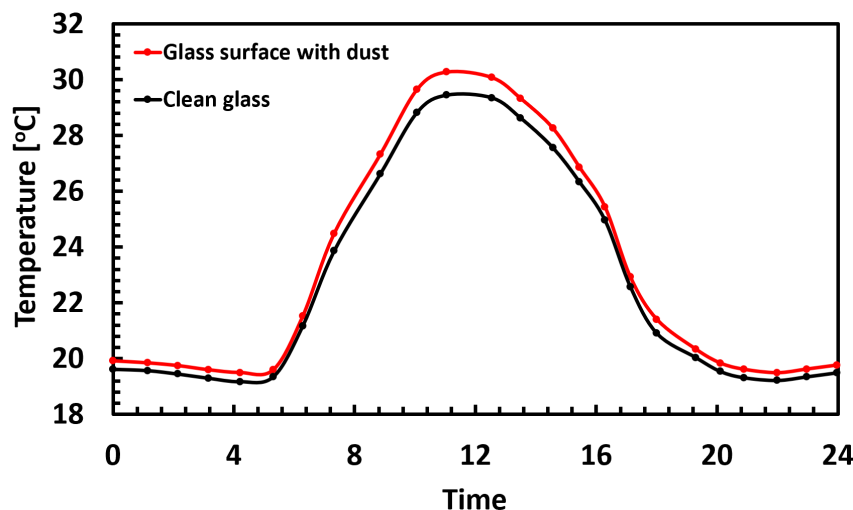


**Figure 4.8:** Simulated PV/T surface temperature for soiled and clean glass.

In the present study, the effect of the soiling glass on the condensation will be later experimentally investigated.

### Effect of the Ground Temperature

The effect of the ground soil temperature on the PV/T-GSHEX performance is an important parameter that thoroughly needs to be investigated. The model was run for different ground temperatures to predict the annual number of hours, when the occurrence of condensation ( $T_{PV/T} < T_{dew}$ ) or overheating ( $T_{PV/T} > T_{PV}$ ) is likely. Figure 4.9 shows the number of condensation and overheating hours on the PV/T surface for different ground temperatures at the location of Qatar.

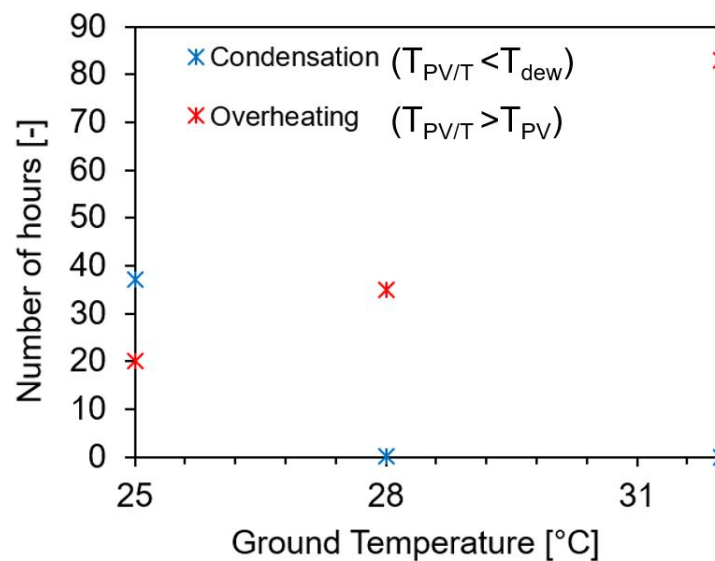


**Figure 4.9:** Number of condensation/overheating hours for the annually simulated PV/T surface temperature.

It can be shown that increasing the soil temperature is decreasing the number of hours for the condensation phenomena and vice versa for the overheating phenomena. However, for the two locations (Qatar and Malaysia) this was just a few hours over the whole year, which occurred at times that are not characterized by dusty winds.

### Effect of Different Depths

Soil temperature close to the ground surface is more susceptible to weather conditions. Soil temperature is fluctuating seasonally and daily due to solar radiation energy changes and other weather conditions on the ground surface. In Qatar, when the GSHEX system is placed at a depth of 1 m, the temperature difference between the water entering the GSHEX and the soil is less than the temperature difference between the soil and the same GSHEX placed at a depth of 4 m (far from the external weather influences). Therefore, the heat exchange between the PV panel and the water will be less at 1 m.

Figure 4.10 shows the annual average temperature of the traditional PV panel in comparison to the PV/T surface temperature integrated into a GSHEX at 1 m and 4 m.

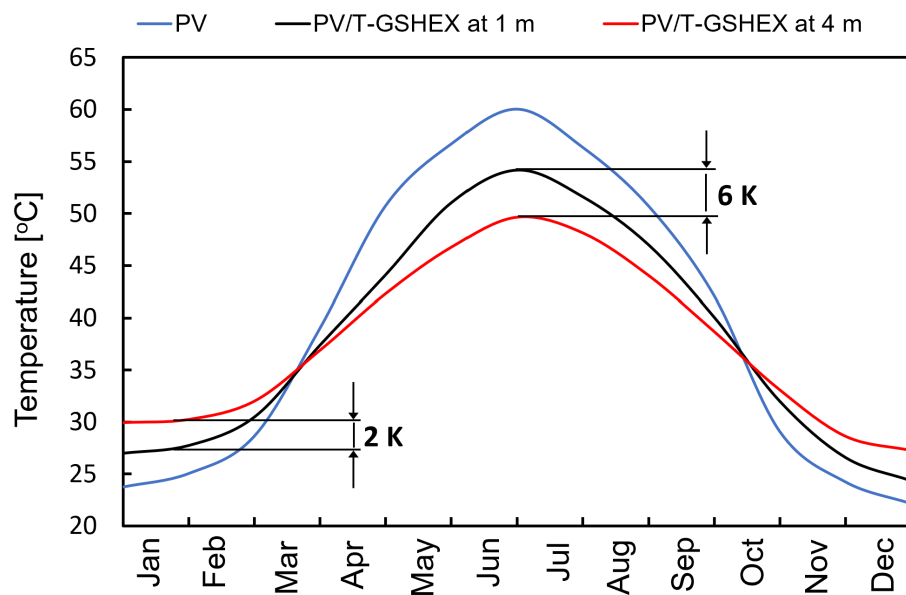


**Figure 4.10:** Annual PV and PV/T-GSHEX average surface temperatures at 1 m and 4 m depth for Qatar.

The results show an increase in the surface temperature of the PV/T-GSHEX system at a depth of 1 m (around 6 K) in comparison to a depth of 4 m during the periods which are characterized by high air temperatures. On the contrary, it decreases around 2 K during the cold periods when the PV panels are more

susceptible to the condensation phenomenon.

Although the cooling and heating processes are better at a depth of 4 m, 1 m is sufficient to mitigate diurnal overheating and nocturnal condensation according to the application required. Therefore, placing the GSHEX at 1 m depth will be economically preferable in order to reduce the cost of the installation process.

## **4.5 Summary**

The PV/T-GSHEX model was built up in a Matlab/Simulink environment to simulate the PV cell temperatures in the novel PV/T-GSHEX system compared to cell temperatures in a conventional PV panel. The model results were in good agreement with experiments. The results show that the PV/T-GSHEX system can significantly reduce the overheating and the condensation problems in the two chosen locations (Qatar and Malaysia), which enhances the performance by around 10 % - 11 %. The meteorological parameter analysis shows that the soil temperature and the radiation are dominant parameters for the system performance. The cooling and heating process were less at a depth close to ground surface (1 m) compared to a depth of 4 m. However, if the PV/T-GSHEX is used for an application which doesn't require a high cooling and heating load, installing the system at a lower depth is economically preferable due to the low installation costs.

To evaluate the assumption of clean PV glass in the mathematical model of the PV/T-GSHEX system, the effect of the dust layer on the onset time of condensation will be studied in the next chapter. The results will indicate whether the dust will accelerate the onset of condensation or the clean glass assumption is the worst case.

## **5 Experimental and Theoretical Investigations on Condensation**

The onset of condensation is a critical parameter affected by the heat transfer process between the GSHEX and the PV/T panel. The results of the PV/T-GSHEX model were obtained under the assumption that the surface of the PV glass is clean. In order to make the model more realistic, the worst case of PV glass covered with a layer of soil dust should be considered. In the present chapter, an experimental and mathematical study is presented to study the effect of environmental parameters such as the air velocity and the presence of a micro-dust layer on the onset of condensation. The purpose of the present work is to investigate how the dust layer influences the onset time of condensation and the droplet growth on the glass surface. The first case (clean glass) will indicate if the assumption of clean glass, which was applied in the PV/T-GSHEX model, is the worst case or if dust layers will accelerate the onset of condensation.

### **5.1 Experimental Investigation**

The aim of the experiments was to quantify the condensate droplet growth under various PV glass surface conditions, which were artificially created in a laboratory facility at University Technology Petronas (UTP). These conditions comprised clean solar glass substrate, and solar glass substrate covered with different thicknesses of dust layer. The glass was subjected to different conditions (air velocity and dust layer thickness) to study the time-dependent development of droplets. The condensed droplets and the mud layer on the glass were visualized using optical microscopy connected to a high-speed camera (HSC) with adjustable lenses.

## Experimental Setup

A schematic set-up of the system is shown in Figure 5.1. Air was supplied through a rectangular polycarbonate duct (110 mm × 110 mm) by a fan. The fan was adjusted to provide different air-flow velocities in the air duct. The duct was designed to enable ideal measurement accessibility, defined air flow velocity, and an adjustable surface temperature of the glass surface.

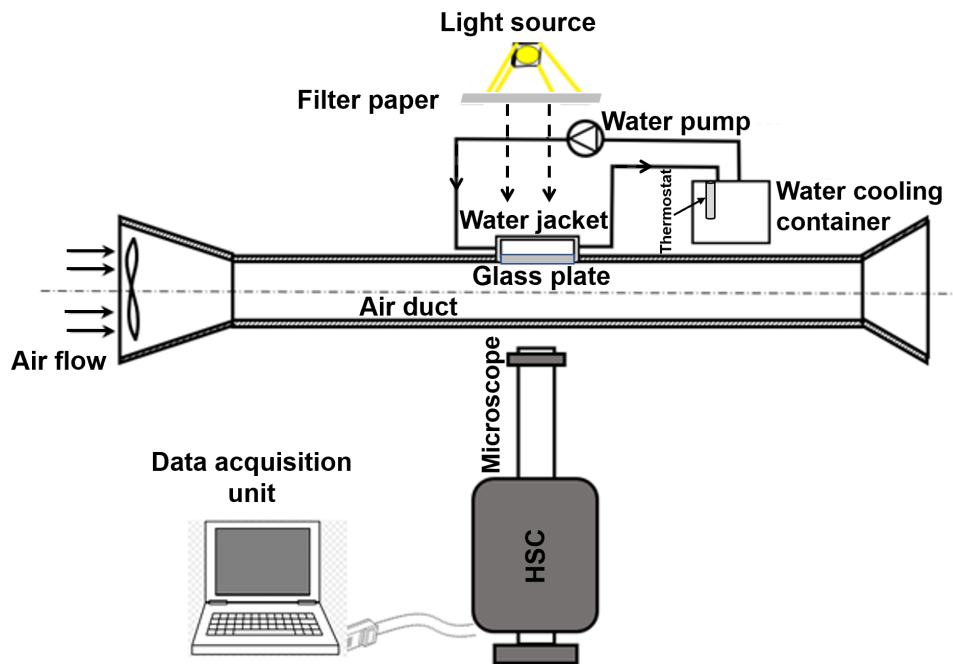


**Figure 5.1:** Schematic of the test rig and data acquisition system.

A test glass plate (60 mm × 60 mm × 2 mm) is embedded into the wall of the duct. To achieve condensation, it is cooled to temperatures lower than the dew point temperature of the air in the duct. Cooling of the glass plate is achieved using a cooling container filled with water as a coolant. The water temperature was controlled by a thermostat and circulated by a water pump through pipes to the glass plate's rear water jacket. This way, the temperature of the glass plate is kept constant during the condensation test phase. The minimum temperature was 4°C, which was applied for the condensation phase. A maximum temperature of 18°C was applied to dry the glass plate after every test.

The whole system was located in a controlled climate chamber to ensure a constant environmental temperature and humidity.

### **High Speed Camera (HSC)**

The High Speed Camera (HSC, Fast Cam Phantom Miro Digital Camera M310) with frame rates of 80-160 fps was used in the experiment to obtain information on the time-dependent droplet diameter and the dynamic droplet growth. The camera was mounted to a rail, to allow a precise variation of the camera distance. A zoom option was provided by a Sony S58 lens. The condensed droplets and mud layers on the glass were visualized using a long-distance microscope (type K2 DistaMax) connected to the HSC with adjustable lenses. The system produced a two-dimensional image of the water droplet. Images were acquired at 150 fps with a resolution of  $1280 \times 720$  dpi. A PALLITE-VIII industrial floodlight was used to provide lighting of the test specimen. It was placed behind the glass plate. The camera and the light source were positioned on the same axis.

### **Digital Image Processing**

Digital image processing techniques have been widely used in the study of condensation phenomena. Their main purpose is the detection of droplet boundaries particularly from the edges of the droplets, which are difficult to observe due to a low contrast ratio. In the present investigation, an image processing tool, Motic Image Plus 2.0 ML was used to analyze the images and to acquire the droplet number and equivalent droplet diameter  $d_{eq}$ . In order to determine the equivalent droplet diameter  $d_{eq}$  with acceptable accuracy, the droplet diameter was measured in four directions and the average was considered.

## Data Acquisition

The values of air velocity were chosen as  $\sim 0$  m/s (near-free-convection), 1.63 m/s, and 8.58 m/s, while the thickness of the micro-dust layer was chosen as 0  $\mu\text{m}$ , 30  $\mu\text{m}$  and 56  $\mu\text{m}$ . In the first set of experiments, a HSC was used to record a video for the droplets produced on the substrate for various air velocities. For each air flow condition, video acquisition started after setting the substrate and air temperatures, and both air velocity and temperatures had reached a steady state. This process was repeated for different air flow velocities and dust layer thicknesses. The dust layer was applied by adding sand dust to a 60 mm  $\times$  60 mm glass plate. This was done by sieving an amount of soil with a very fine sieve from a distance perpendicular to the glass plate. The dust layer thickness was determined from the weighted dust quantity assuming constant dust layer thickness. The statistical nature of the overall process, involving the multiple generation of droplets on the substrate at different stages, is clearly visible under the camera. A time series for this droplet pattern is illustrated for each average dust layer thickness and air velocity. The boundary conditions for the experiments are given in Table 5.1.

**Table 5.1:** Selected boundary conditions for the experimental investigations.

Air velocity [m/s]	0	1.63	2.76	8.58
Dust layer thickness [ $\mu\text{m}$ ]	0	30	56	
Air Temperature [ $^{\circ}\text{C}$ ]	22.4			
Humidity [%]	57.3			
Substrate Temperature [ $^{\circ}\text{C}$ ]	11.8			
Dew point temperature [ $^{\circ}\text{C}$ ]	12.7			

Conventional measurement instruments were used (the same measurement devices used in the experiments mentioned in chapter two) to capture the ambient air temperature ( $T_\infty$ ), humidity (RH) and velocity ( $u_\infty$ ) as well as the substrate temperature ( $T_s$ ). All air conditions were measured at the outlet of the duct.

## 5.2 Mathematical Analysis

The mathematical model is based on individual droplet growth governed by convection and diffusion, therefore it can estimate droplet growth prior to coalescence. The model will be applied as a parametric study tool to estimate the time to the onset of condensation and the droplet growth rate for different air flow conditions.

### 5.2.1 Droplet Growth Under Free Convection

In this case, the PV panels run under free convection conditions, where the airflow rate is assumed to be negligible. To simulate this condition, the experiment was performed in the duct with no airflow, further considered as free convection environment. In such conditions, the droplet grows due to diffusion of water vapor from the ambient air to the droplet at saturation vapor pressure [132-136]. The water vapor diffusion rate from the air to the droplet can be expressed as

$$\frac{dm}{dt} = 4\pi r D(\rho_\infty - \rho_{\text{sat}}), \quad (5.1)$$

where  $D$  is the mass diffusion coefficient from the air to the droplet and  $\rho_\infty$ ,  $\rho_{\text{sat}}$  are the ambient air density and saturated air density respectively.

Here, the air velocity is almost zero, and the convection heat transfer rate from droplet to ambient air is negligible. In such a case, heat transfer between the droplet surface and the ambient is dominated by conduction [157], and the heat flow can be written as

$$\frac{dQ}{dt} = -4\pi r k (T_{\infty} - T_{\text{sat}}) . \quad (5.2)$$

The amount of heat released by the condensation rate of water vapor in the air has to be dissipated by heat conduction from the droplet. Compared to the latent heat of condensation, the heat capacity of the droplet is much smaller, and it can be ignored [37,38]. Thus, the power balance equation is:

$$L_c \frac{dm}{dt} = \frac{dQ}{dt} . \quad (5.3)$$

From equations (5.1)-(5.3), equation (5.4) can be obtained,

$$L_c D(\rho_{\infty} - \rho_{\text{sat}}) = k(T_{\infty} - T_{\text{sat}}) , \quad (5.4)$$

where  $k$  and  $L_c$  are the thermal conductivity and the latent heat of condensation respectively. Here, the vapor temperature  $T_{\text{sat}}$  and density  $\rho_{\text{sat}}$  are unknown. However, in equation (5.4),  $(T_{\infty} - T_{\text{sat}})$  can be assumed small, as the temperature of the growing droplet is in proximity to the ambient temperature [138]. The vapor density at saturation relates to the saturation vapor pressure  $p_{\text{sat}}$  over a droplet and can be described by:

$$\rho_{\text{sat}} = \frac{p_{\text{sat}}(r)}{RT_{\text{sat}}(r)} , \quad (5.5)$$

where  $R$  is the ideal gas constant. However, the saturation vapor pressure over a droplet can be obtained from the Clausius-Clapeyron equation

$$\frac{d \ln(p_{\text{sat}})}{dT} = \frac{L_c}{RT^2} . \quad (5.6)$$

Expanding the exponential term of  $p_{\text{sat}}$  in equation (5.6), and using equations (5.1) to (5.5), the expression for the droplet growth  $\frac{dm}{dt}$  can be obtained as:

$$\frac{dm}{dt} = \frac{4\pi r(S-1)}{\frac{L_c^2}{k R T_\infty^2 f_T} + \frac{1}{\rho_{\text{sat}} D f_\rho}} . \quad (5.7)$$

Here,  $S$  is the ambient saturation ratio and can be defined as  $S = \frac{p_\infty}{p_{\text{sat}}}$ , where  $p_\infty$  is the ambient pressure.  $f_T$  and  $f_\rho$  are normalization factors for temperature difference and density difference respectively [157].

The Maxwell diffusion equation can also be used, leading to

$$\frac{dm}{dt} = \rho_0 4\pi r^2 \frac{dr}{dt} . \quad (5.8)$$

The growth rate can be derived as shown by Fukuta and Walter [157]

$$r \frac{dr}{dt} = \frac{S - (1+B)^{-1} A}{\frac{L_c^2 \rho_0}{k R T_\infty^2 f_T} (1+B)^{-1} A + \frac{\rho_0 R T_\infty}{\rho_0 D f_\rho}} , \quad (5.9)$$

where  $\rho_0$  is the density of the liquid phase,  $\beta$  is the condensation coefficient and parameters  $A$  and  $B$  are constants [157].

As the droplet grows into a relatively large size due to more condensation, equation (5.9) can be simplified to [157]

$$r \frac{dr}{dt} = \frac{S-1}{\frac{L_c^2 \rho_0}{R T_\infty^2 k} - \frac{L_c \rho_0}{k T_\infty} + \frac{\rho_0 R T_\infty}{D h(T)}} . \quad (5.10)$$

This equation can be solved analytically to obtain the time-dependent droplet growth  $\frac{dr}{dt}$  .

### 5.2.2 Droplet Growth Under Forced Convection

Droplet growth under forced convective flow conditions is governed by advection-diffusion factors, as shown in Figure 5.2. The diffusion of water vapor towards the droplet would increase the droplet size. However, mass transfer towards the environment can also take place due to the flow itself, which can inhibit the droplet growth [136].

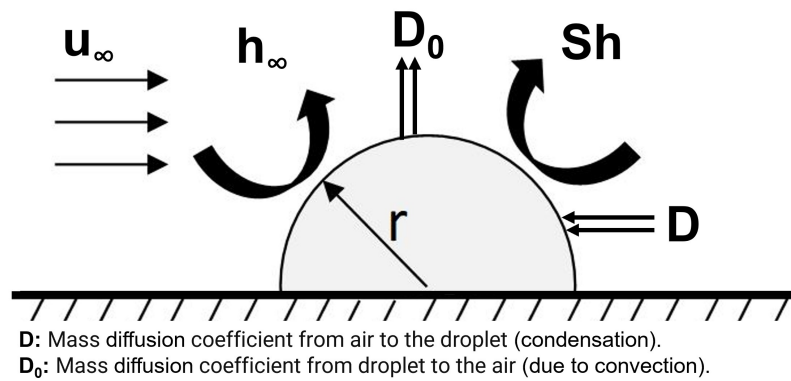


**Figure 5.2:** The condensate droplet under airflow conditions subjected to convective heat and mass transfer.

The mass transfer correlation is governed by the Sherwood number,

$$Sh = (h_m r) / D_0 \quad (5.11)$$

where  $D_0$  is the mass diffusion coefficient from the droplet to the air and  $h_m$  is the convective mass transfer coefficient. In this case, equation (5.1) can be rewritten as

$$\begin{aligned} \frac{dm}{dt} &= 4\pi r D (\rho_\infty - \rho_s) - 4\pi r D_0 (\rho_\infty - \rho_s) \\ &= 4\pi r (D - D_0) (\rho_\infty - \rho_s). \end{aligned} \quad (5.12)$$

Therefore, in comparison to equation (5.1) the droplet growth is smaller under convective flow conditions.

The equation for the Sherwood number of a single droplet can also be expressed by [148]:

$$\text{Sh} = 2 + 0.552 \text{Re}^{0.5} \text{Sc}^{0.33} . \quad (5.13)$$

Then,  $D_0$  can be obtained from the equations (5.11) and (5.13). Here, the Reynolds number is [148]

$$\text{Re} = (\rho u_\infty L) / \mu , \quad (5.14)$$

and the Schmidt number is

$$\text{Sc} = \mu / (\rho D_0) . \quad (5.15)$$

Under free convection conditions, the latent heat of vaporization is transferred by conduction. Under forced convection, the latent heat of vaporization is transferred by both conduction and convection as can be shown in the following expression:

$$\begin{aligned} \frac{dQ}{dt} &= 4\pi r^2 h_\infty (T_r - T_\infty) - 4\pi r k (T_r - T_\infty) \\ &= 4\pi r (r h_\infty - k) (T_r - T_\infty) . \end{aligned} \quad (5.16)$$

The heat release  $dQ/dt$  in equation (5.16) is equivalent to the latent heat of vaporization. Therefore,

$$\begin{aligned} \frac{dQ}{dt} &= L_c \frac{dm}{dt} , \\ 4\pi r (r h_\infty - k) (T_r - T_\infty) &= L_c 4\pi r (D - D_0) (\rho_\infty - \rho_{\text{sat}}) , \end{aligned} \quad (5.17)$$

$$\frac{(\rho_\infty - \rho_{\text{sat}})}{(T_r - T_\infty)} = \frac{(r h_\infty - k)}{L_c (D - D_0)} .$$

The equilibrium pressure over a droplet can be written as

$$p_{\text{sat}}(r) = \rho_{\text{sat}} R T_{\text{sat}}(r) \cdot \quad (5.18)$$

Accordingly, the droplet growth can be obtained from the following equation [157]:

$$r \frac{dr}{dt} = \frac{S-1}{\frac{L_c^2 \rho_0}{RT_\infty^2 k} - \frac{L_c \rho_0}{(r h_\infty - k) T_\infty} + \frac{\rho_0 R T_\infty}{(D - D_0) h(T)}} \cdot \quad (5.19)$$

Generally, at an early stage of condensation, the droplet radii are very small ( $r \approx 0$ ), therefore,  $r h_\infty \ll k$ . Thus, equation (5.19) can be reduced to

$$r \frac{dr}{dt} = \frac{S-1}{\frac{L_c^2 \rho_0}{RT_\infty^2 k} + \frac{L_c \rho_0}{k T_\infty} + \frac{\rho_0 R T_\infty}{(D - D_0) h(T)}} \cdot \quad (5.20)$$

Here, the value of  $D_0$  is updated at each time step. The initial value of  $D_0$  is obtained from the Sherwood number and equation (5.11).

To solve equation (5.20) the following boundary conditions can be applied:

$$t \rightarrow t_0, r \rightarrow 0 \quad \text{and} \quad t \rightarrow t_1, r \rightarrow r_1 \cdot$$

By applying the above mentioned conditions, equation (5.19) can be integrated to obtain an estimation of the onset time of condensation

$$t_0 = t_1 - \frac{r_1^2}{2C_1} \cdot \quad (5.21)$$

Here,  $C_1$  at  $t \rightarrow t_1$  is

$$C_1 = \frac{S - 1}{\frac{L_c^2 \rho_0}{RT_\infty^2 k} + \frac{L_c \rho_0}{kT_\infty} + \frac{\rho_0 RT_\infty}{(D - D_0)h(T)}}. \quad (5.22)$$

### 5.3 Results and Discussion

The equivalent droplet diameter  $d_{eq}$  was assumed to be a critical indicator of droplet growth. The high-speed camera captured real-time images of the droplet's geometric shapes as can be seen in Figure 5.3. Images were prepared for the next step where these parameters were quantified by a statistical analysis, such as the droplet-filled area  $A$  and the equivalent diameter  $d_{eq}$ . Here, the number of droplets and the  $d_{eq}$  were obtained by using the Motic Image Plus 2.0 ML software. The original size of the image obtained from the video camera is  $1280 \times 720$  pixels. The visualization area is reduced to  $1013 \times 635$  pixels or  $12 \text{ mm} \times 6 \text{ mm}$  to avoid any unwanted influence of temperature gradients on the edges of the substrate. A range of different droplet patterns and diameters was observed as can be seen in Figure 5.3.

The equivalent droplet diameter ( $d_{eq}$ ) followed a statistical variation. The observed range of  $d_{eq} = 0.098 \text{ mm} - 3.178 \text{ mm}$  is due to droplet coalescence. Coalescence eventually leads to film formation on the surface. However, at the initial stage of condensation, the coalescence rate is very low. As the focus was on the determination of the onset of condensation, in the mathematical model, coalescence was neglected.

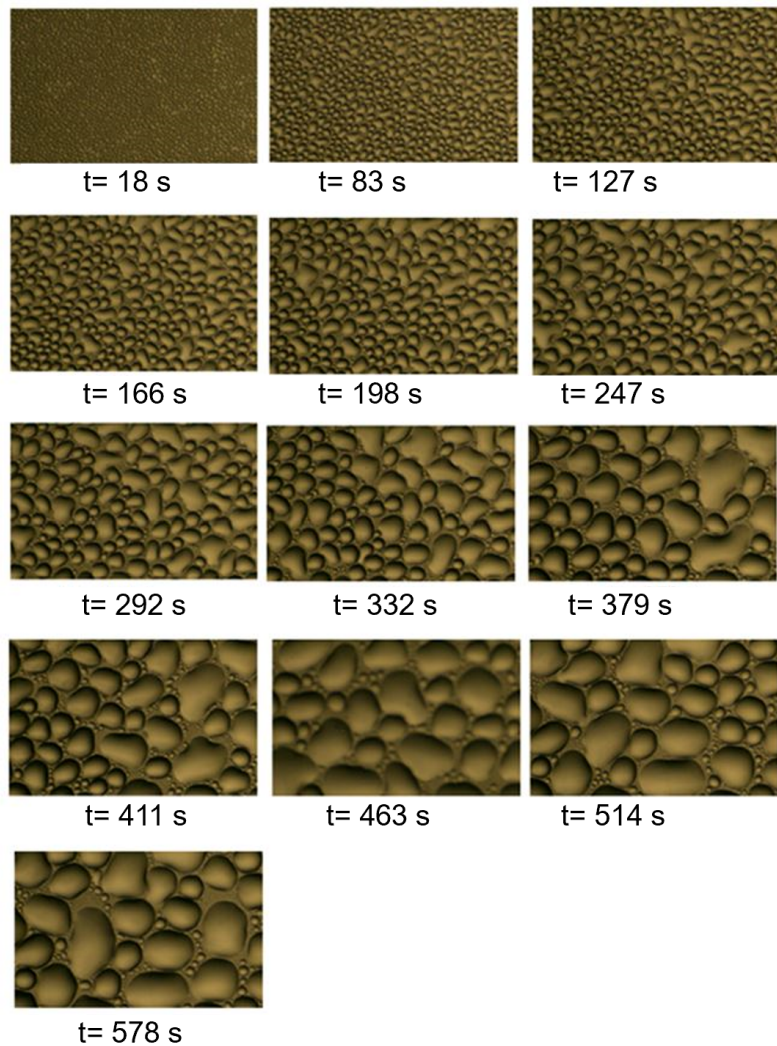


**Figure 5.3:** Microscopic condensation images for clean glass ( $\delta = 0 \mu\text{m}$ ) and free convection ( $u_\infty = 0 \text{ m/s}$ ).

The model requires an initial approximation of the droplet diameter, therefore it is difficult to accurately predict the onset time of condensation. As a reference diameter for the onset of condensation,  $d_{\text{eq}} \approx 0.19 \text{ mm}$  was defined. This droplet radius is the lowest diameter that can be measured by the equipment used in the experiment. A series of microscopic images of droplet growth for different micro-dust layers and under different air velocities are shown in Figures 5.3 - 5.6.

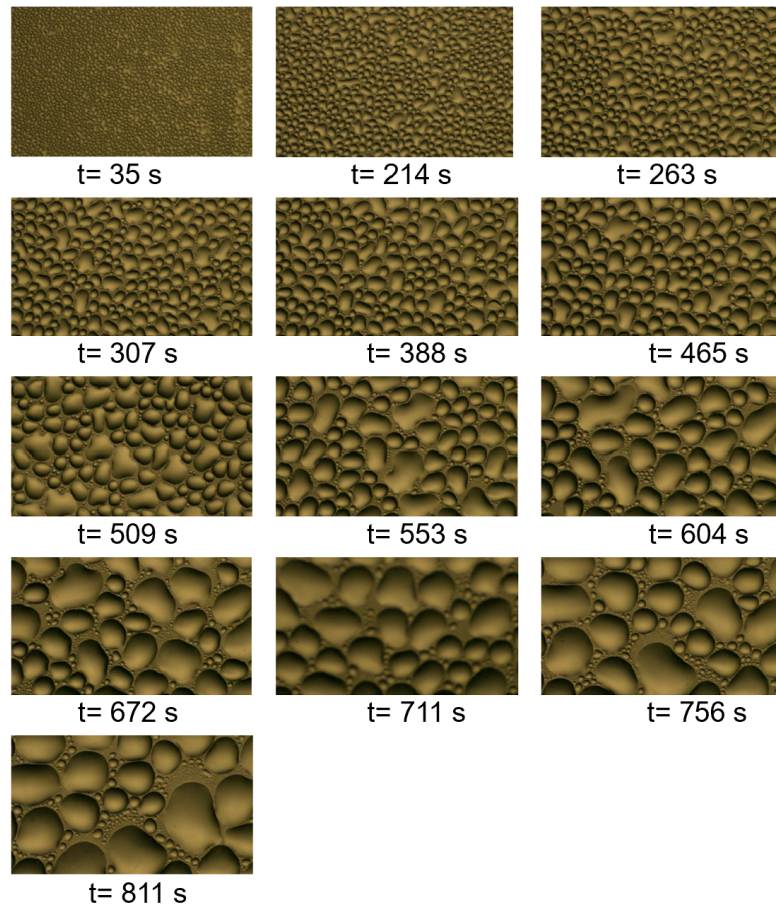


**Figure 5.4:** Microscopic condensation images for clean glass ( $\delta = 0 \mu\text{m}$ ) and forced convection ( $u_\infty = 8.58 \text{ m/s}$ ).

In Figures 5.3 and 5.4 the microscopic images of the droplet growth under natural convection and forced convection ( $u_\infty = 8.58 \text{ m/s}$ ) on a clean glass surface (dust layer  $\delta = 0$ ) are presented as a baseline case. In comparison to that, Figures 5.5 and 5.6 show droplet growth phenomena for an airflow velocity of  $u_\infty = 8.58 \text{ m/s}$  and two different average thicknesses of dust-layer ( $\delta = 30 \mu\text{m}$  and  $56 \mu\text{m}$ ). During the early stage in every test, the droplet grows by mass diffusion from the environment and with minor coalescence. Without external disturbances or any impurity content, on a clean surface, the profile of the droplet growth can clearly be captured, see Figure 5.3. This observation is consistent with literature [137].

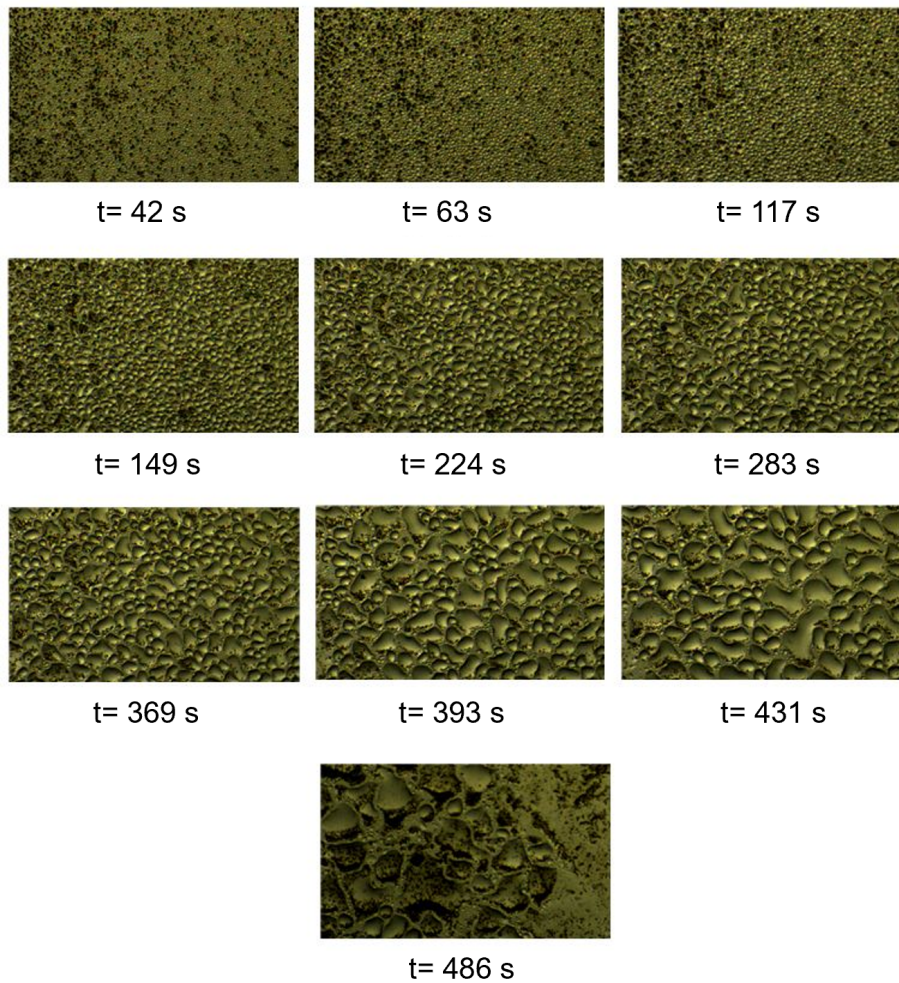


**Figure 5.5:** Microscopic condensation images for glass with dust layer thickness ( $\delta = 30 \mu\text{m}$ ) under forced convection ( $u_\infty = 8.58 \text{ m/s}$ ).

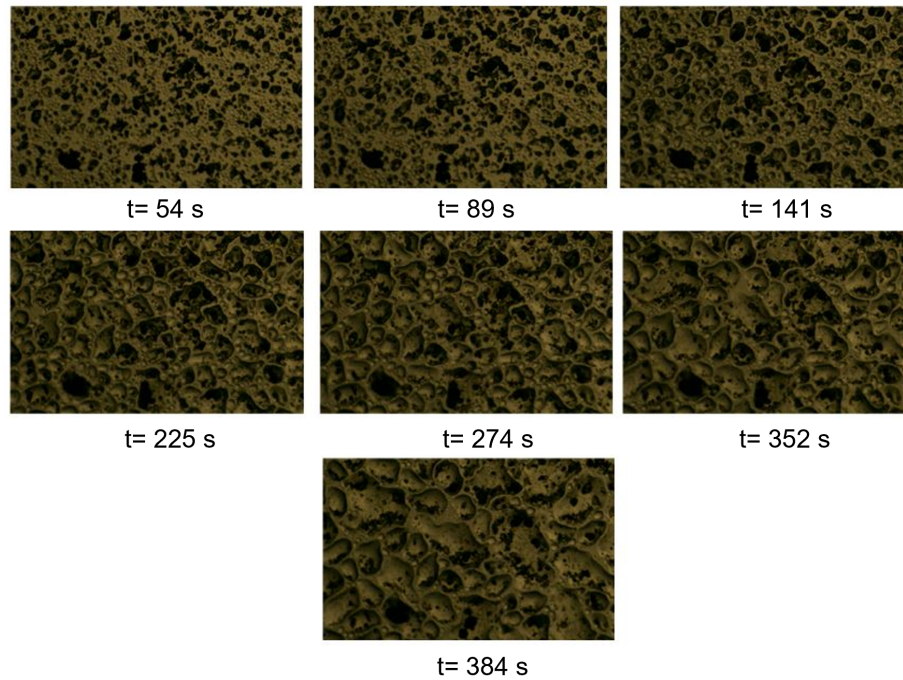


**Figure 5.6:** Microscopic condensation images for glass with dust layer thickness ( $\delta = 56 \mu\text{m}$ ) under forced convection ( $u_\infty = 8.58 \text{ m/s}$ ).

Under the present laboratory conditions, the presence of a micro-dust layer acts as a thermal resistance between the solid surface and the air. This affects the droplet's morphological and growth properties [130,131]. The micro-dust layer can slightly increase the surface temperature as was observed during the conducted condensation experiments and the previous results of the mathematical model of the PV/T-GSHEX system.

Under real-life conditions in an outdoor PV/T-GSHEX system, a dust layer can also cause elevated surface temperatures on the PV/T modules. In contrast to the lab case, this is not due to thermal resistance but due to a reduction in the long wave emissivity of sand ( $\epsilon_{\text{LWrad}} \approx 0.76$ ) and soil ( $\epsilon_{\text{LWrad}} \approx 0.9$ ) compared to the long wave emissivity of clean glass surface ( $\epsilon_{\text{LWrad}} \approx 0.94$ ). In addition, the surface roughness changes will result in a change in the structure of the droplet and its growth properties [141,142].

The presence of dust also alters the conditions affecting the onset of condensation [128-139] and tends to promote mud clots, which are visible under the microscope, see Figure 5.6. Such mud clots inhibit droplet growth and make the structure of the droplet more inhomogeneous, thus making it difficult to attribute a reasonable droplet diameter.

Under the same airflow rate (8.58 m/s), as the thickness of the micro-dust layer increases (30  $\mu\text{m}$  to 56  $\mu\text{m}$ ), more mud-clot formation can be observed in the microscope image, as can be seen in Figures 5.5 and 5.6. It is evident from the microscopic images that the micro-dust layer promotes droplet coalescence in a radial direction. However, both dust and airflow significantly retard the onset of condensation. It is also evident that in the observation area the droplet growth is not uniform and droplets grow in different sizes and profiles at the same instance under different airflow velocities. However,  $d_{\text{eq}}$  follows a statistical distribution with a maximum frequency (number of droplets within the same  $d_{\text{eq}}$  range) as is shown in Figure 5.7. Therefore, the total average droplet diameter can be approximated by the diameters at maximum droplet frequency.

Initially, the droplets are small and homogeneous in size, starting at the onset of condensation. Then droplet diameters start to grow non-linearly with time. After 18 s, the droplet diameters are ranging from 0.098 mm to 0.167 mm with a maximum occurrence at 0.098 mm. However, at 198 s, the distribution frequency ( $\sim 10$ ) of the droplet diameters is evenly distributed in a range of 0.145 mm  $\sim$  0.838 mm. The variation in droplet size distribution over time is due to the droplets coalescence, see Figure 5.7. Coalescence increases significantly after 379 s. As time progresses, the droplets grow bigger and the frequency of coalescence with an adjacent droplet increases significantly, creating a water film. After 578 s, the droplets begin to disappear due to water film formation. Hence, it is difficult to quantify the droplet size experimentally after a longer time.

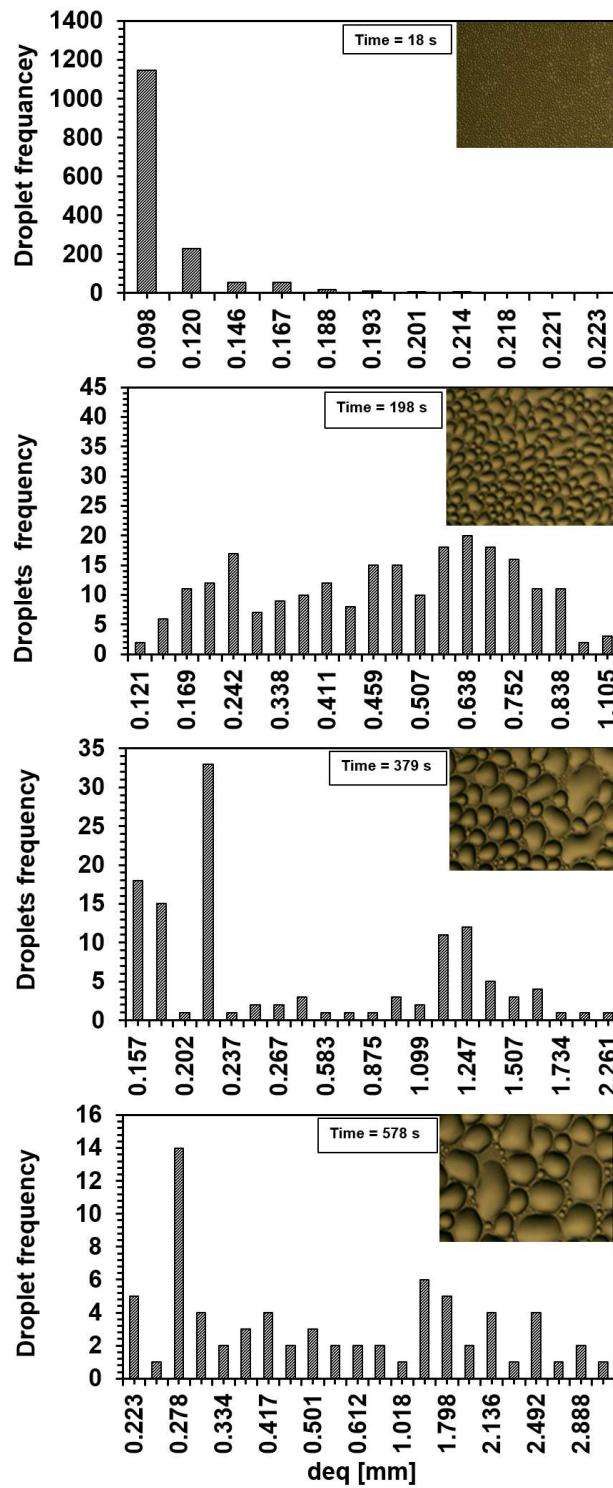


**Figure 5.7:** Visual and statistical profile of the experimentally determined droplet distribution patterns and corresponding histograms of droplet frequency at different times for clean glass ( $\delta = 0 \mu\text{m}$ ) and free convection ( $u_\infty = 0 \text{ m/s}$ ).

Figures 5.8a and 5.8b show the effect of different dust layer thicknesses and different airflow velocities more clearly by determining the time to the onset of condensation. The presence of dust particles ( $30\ \mu\text{m}$ ) contributes to delaying the onset of condensation by about 9 s in comparison to the clean surface, see Figure 5.8a. This delay in the onset of condensation in the presence of dust particles can be attributed to the increase in the surface temperature in the laboratory environment due to the thermal insulation effect. Under real conditions, this delay can be due to the lower emission from the PV surface to the sky, where dust particles' emissivity is lower than the glass's emissivity, see also [19, 35]. It can be concluded that the higher the dust layer thickness, the higher the delay in the onset of condensation. For higher airflow rates, the onset of the condensation process is delayed, as it inhibits both the mass diffusion process, and possibly the droplet growth process due to advection, as shown in Figure 5.8b. At 0 m/s, the onset of condensation was observed at 18 s, whereas it was delayed to 34 s and 131 s for air velocities of 1.63 m/s and 8.58 m/s, respectively.

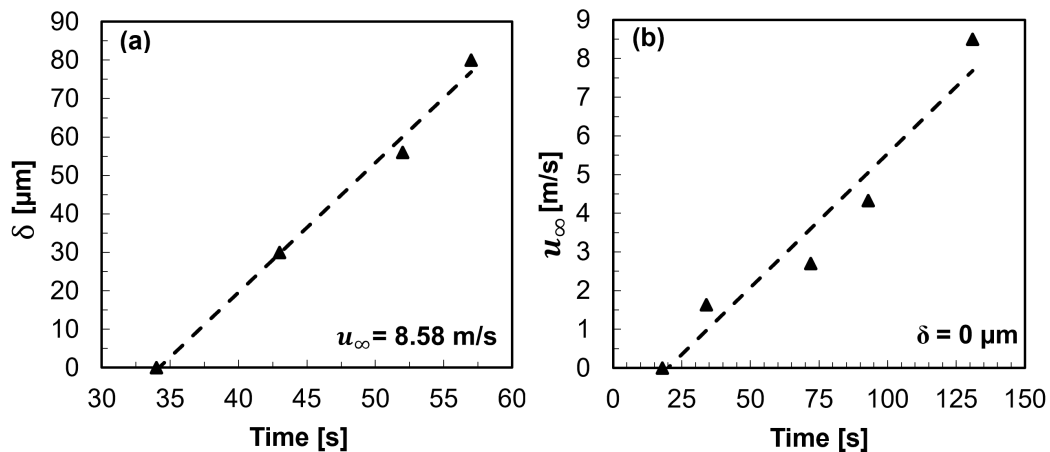


**Figure 5.8:** Time to detect condensation as a function of (a)  $\delta = (0, 30, 56, 80)\ \mu\text{m}$  and (b)  $u_\infty = (0, 1.63, 2.76, 8.58)\ \text{m/s}$ .

Under forced convection conditions (where the saturated boundary layer of the air around the droplet is disturbed due to higher flow velocities), two phenomena can occur on the droplet.

Firstly, the mass transfer to the environment takes place due to advection, which slows down the droplet growth and can be defined by the Sherwood number [140,150]. Secondly, the heat transfer rate can increase due to forced convection [150,151]. Figure 5.9 shows a comparison between the analytical and the experimental results.

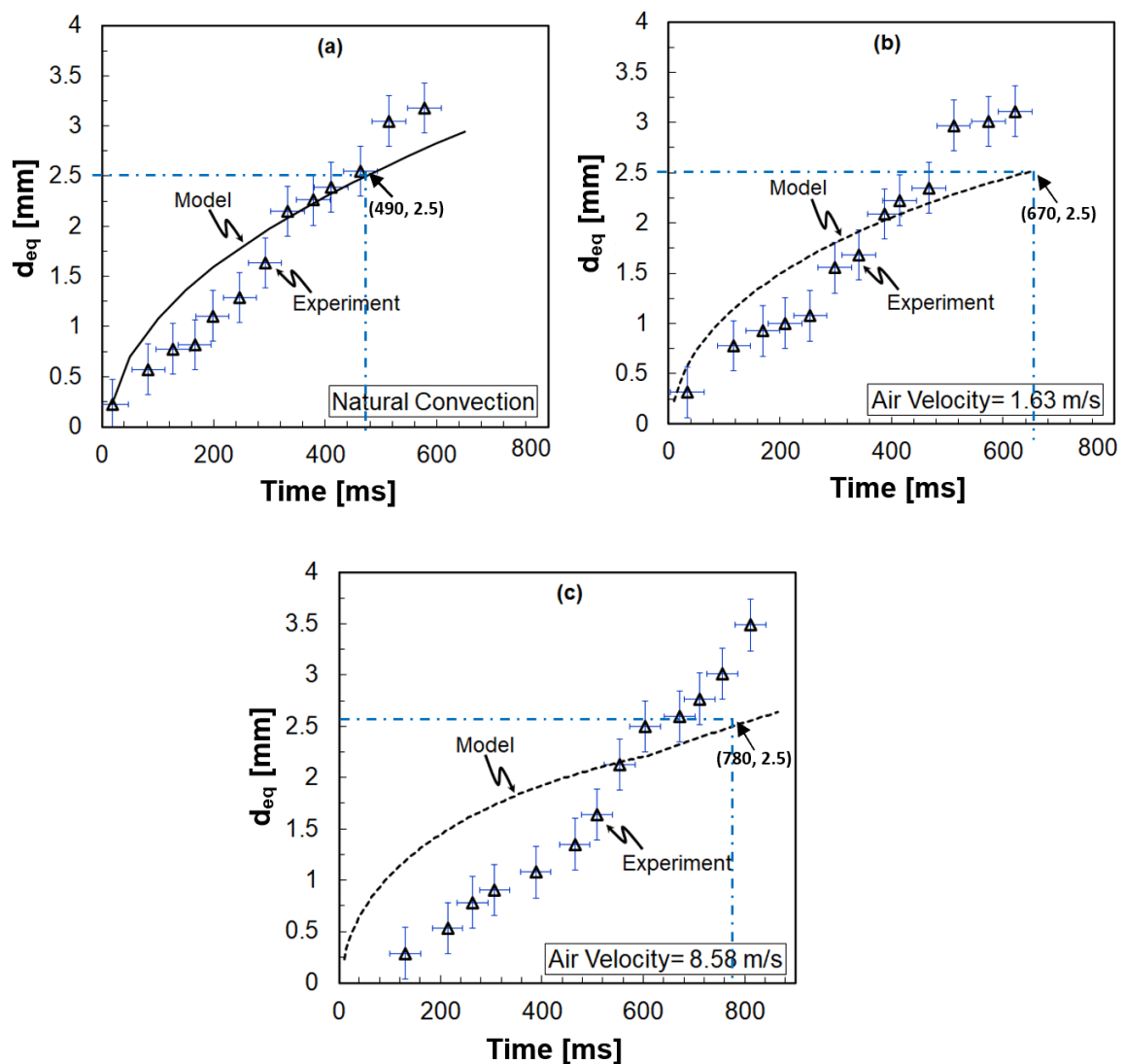


**Figure 5.9:** Comparison of the experiment results and the model for droplet growth at air velocities (a) 0 m/s, (b) 1.63 m/s and (c) 8.58 m/s.

Under a confined environment and in the absence of any natural disturbances (clean glass under natural convection), droplet growth can be maximized. This finding matches with the model before coalescence effects start at 500 ms, as can be seen in Figure 5.9a. For free and forced convection at low velocity, a reasonable agreement between the model and the experiment can be seen. However, for higher airflow velocities and at a later time, as the coalescence rate increases and becomes the primary mechanism of droplet growth. This can be observed by the deviation between the experiment and the model results was observed, see Figures 5.9b and 5.9c. At a flow velocity of 1.63 m/s, coalescence becomes the primary mechanical process after 600 ms. However, coalescence at a flow velocity of 8.48 m/s needs more time to be started (800 ms). Hence, droplets need a longer time to be detectable under higher airflow velocities.

At relatively low velocities it can be seen that in terms of the droplet diameter the model shows good agreement with the experimentally determined droplet growth rate. Comparing experimental and model results leads to average errors of 1 % at 0 m/s and 4 % at 1.63 m/s. However, at airflow velocities of 0 m/s, 1.63 m/s, and 8.5 m/s, the maximum errors of the model were estimated as 12.9 %, 16.6 %, and 70 % respectively. It should be noted that these are maximum errors. The reason for that can be attributed to a number of factors, e.g. the empirical correlation to calculate the convection heat transfer coefficient as a function of the airflow velocity is more accurate at lower velocities [160]. Besides, the measured equivalent diameter depends on the average statistical diameter, which leads to a lower level of accuracy at some points.

In Figure 5.10, the effect of the environmental Relative Humidity (RH) on the droplet growth rate is presented. A significant increment of condensation droplet growth can be observed in an environment with higher relative humidity. In order to clarify the delay in the time to the onset of condensation, Figure 5.10 shows also a zoomed view of the early stage of condensation. This time is increasing under forced convection conditions, as it initially inhibits the mass diffusion process and droplet growth due to advection.

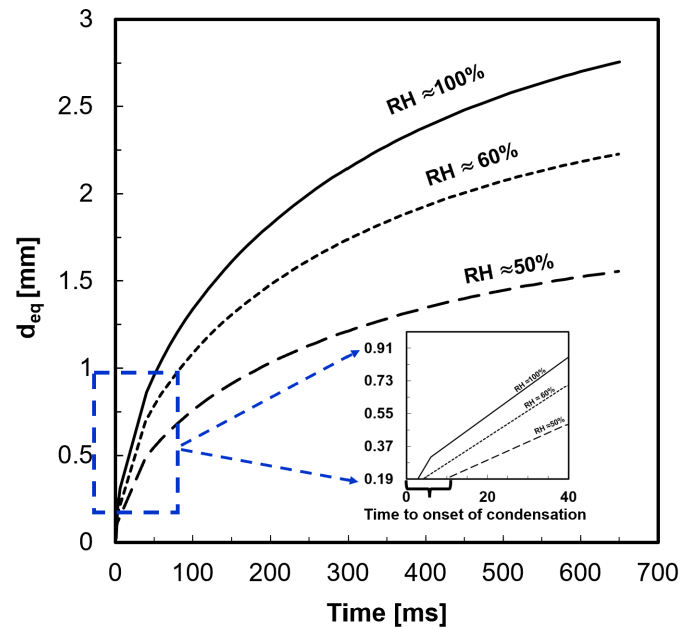


**Figure 5.10:** Effect of relative humidity on the onset of condensation and droplet growth at airflow velocity 1.6 m/s.

The case with higher relative humidity reaches the reference diameter at an earlier time, as can be seen in the same figure. Therefore, it is possible to conclude that the onset time of condensation will be longer for a lower relative humidity. The results shown in Figure 5.10 are based on the solution of a first order ordinary differential equation, the initial diameter was assumed at an initial time. For example, at a time,  $t = 0$ , the droplet diameter was assumed as,  $d_{eq} = 0$ . Hence, depending on the growth rate and slope, it would be possible to extrapolate the onset of condensation. For example, the curve which reaches a reference minimum value first (0.19 mm here) has the lowest time needed for the onset of condensation.

The effects of the micro-dust layer on the condensation process are shown in Figures 5.11a and 5.11b for airflow velocities of 1.6 m/s and 8.58 m/s, respectively. Coalescence is represented by the area right of the blue dashed line in Figure 5.11b.

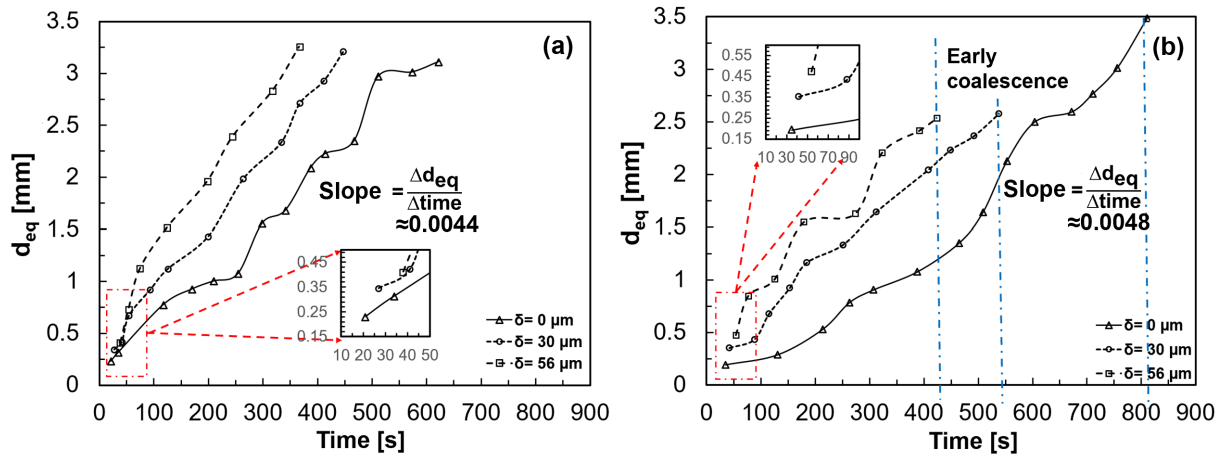


**Figure 5.11:** Experimental data of droplet growth rate for different microdust layer thicknesses on the substrate surface, at airflow velocity (a) 1.6 m/s and (b) 8.58 m/s.

It was observed that the droplet coalescence increases with the microdust layer thickness. In the presence of a  $56 \mu\text{m}$  dust layer, the droplet coalesces earlier and can only be detected for a timespan of up to 366 ms, compared with almost 622 ms for a clean surface. The higher coalescence rate also created an early condensation film.

The droplet growth rates (slopes of the curves in Figures 5.11a and 5.11b) for clean glass are  $0.0048 \text{ mm/s}$  and  $0.0044 \text{ mm/s}$  at air flow velocities of  $1.63 \text{ m/s}$  and  $8.58 \text{ m/s}$ , respectively. At a lower airflow velocity, there was a slight difference in the onset of condensation time for different microdust layer thicknesses. Micro-dust particles promote condensation droplet growth due to early coalescence. At the same time, they delay the onset of condensation due to the higher temperature or the lower emission of the surface as mentioned before [19, 35]. The onset of condensation is prolonged by 6 s for a dust layer of  $30 \mu\text{m}$  and 25 s for a dust layer of  $56 \mu\text{m}$ . The delay in droplet formation can also be attributed to the absorption of water by the dust particles. On the other hand, the droplets attract dust particles due to the surface static charge, thus enhance the droplet coalescence [19, 35]. As a result, a water film and subsequently a mud layer is forming on the surface of the substrate.

## 5.4 Summary

A mathematical model and experiments were performed to investigate the effects of airflow and micro-dust layers on dew formation and droplet growth. The results show that increasing external flow inhibits both the onset of condensation and the droplet growth rate. In addition to that, the presence of micro-dust layers also impedes the onset of the condensation process. At the same time, it augments the droplet coalescence due to its particle static charge and absorption properties [124-127]. Droplets coalescence due to dust particles can eventually form a layer of water and mud on an exposed glass surface. It is therefore of utmost importance to impede the onset of condensation as far as possible.

However, it can be concluded that the PV/T-GSHEX system can still effectively work under the effects of a soiled glass surface and under different airflow velocities, as both effects impede condensation phenomena. Thus, the clean PV glass assumption in the PV/T-GSHEX model can be considered to be the worst case scenario and is valid as a basis for the further investigations.

# 6 Conclusions and Outlook

## 6.1 Conclusions

Overheating of photovoltaic (PV) cells during daytime as well as nocturnal dew and resulting mud formation on the PV panels are major efficiency barriers for the operation of PV in harsh desert climates. Mitigating these two problems requires cooling of the PV cells during daytime and heating them above the dew point at night. The main objective of the present study was to propose and prove a suitable method to mitigate these two barriers with a single technical solution. The method was based on integrating the PV modules with a thermal control system (Hybrid PV/Thermal solar collector, PV/T) and a ground soil heat exchanger (GSHEX). Excess heat from diurnal cooling is charged to the ground soil and discharged to provide heating power during the night. The method was named PV/T-GSHEX and was studied with both experimental and numerical methods. Further investigations were carried out to explore the effect of the PV surface state on the dew formation phenomena. The findings are summarized in the following subsections.

### 6.1.1 Experimental Studies

- An outdoor experimental setup was developed. The novel system was set up with a PV/T module and an integrated GSHEX. A conventional PV module was used for comparative measurements. Compared to the conventional PV module, the experimental results showed a significant benefit of the novel PV/T-GSHEX system. It was possible to substantially cool the PV cells during daytime. The difference between the PV and the PV/T surface temperature was in the range of 8 K - 10 K due to active cooling using the GSHEX.

- In addition, the proposed PV/T-GSHEX system prevented nocturnal condensation and mud formation by transferring the heat from the ground to the PV/T. This process provided enough heat to mitigate dew formation during nighttime and in the early morning hours.
- It was shown that the PV electrical efficiency can be improved by 10 %. Up to 35 % losses in the PV glass transmittance due to eventual mud formation can be prevented. Thus, the proposed thermal control system has a high potential of economic viability.
- The experimental results showed that soil with high thermal conductivity is a more suitable storage material for the task of shifting heat from diurnal to nocturnal operation.

### 6.1.2 Theoretical Modeling of the Soil Temperature Distribution

- A one-dimensional analytical model to determine the soil temperature was developed using the Green's Function (GF) method. The model can estimate the daily and annual variation of the soil temperature at different depths as a function of real-time weather data. The model was validated with measurements and showed an accuracy of up to 96 %.
- A significant advantage of the presented analytical method is the low computational cost, which is one hundred times less than that of state-of-the-art numerical models.
- It was found that under tropical weather conditions (e.g. Malaysia) stable soil temperature can be found closer to the surface than under fluctuating weather locations (e.g. Qatar).
- The results show that the higher the thermal conductivity of the soil, the higher the soil temperature fluctuation and vice versa. This is more obvious at low depths close to the surface. In turn, a higher thermal conductivity enhances heat flux near the ground surface and dampens variations at higher depths.

### 6.1.3 Numerical Simulation

- A numerical simulation model of the PV/T-GSHEX system was developed in a MATLAB/Simulink environment. The model was validated using the experimental data.
- Simulation results for the long-term operation of the proposed PV/T-GSHEX system have been obtained for the locations of Qatar and Malaysia, which have two different and extreme kinds of weather. A good performance was achieved for Malaysia, where tropical weather conditions are prevailing.
- The results were also satisfying for Qatar. However, the GSHEX will need to be placed at a greater depth.
- The PV cells were protected from overheating by reducing the noontime PV surface temperature by around 10 K for Malaysia and 12 K for Qatar on average over the whole year.
- The annual temperature of the solar panel was higher than the dew point temperature by 2 K in average in Malaysia and by 5 K in Qatar, which is sufficient to mitigate dew formation.

### 6.1.4 Parameters Influencing Dew Formation

- Experimental and numerical studies were performed to investigate the parameters influencing the condensation of air humidity on the solar glass surface. This included mainly the airflow conditions and the presence of dust particles on the glass surface. The numerically predicted droplet growth was close to the experimental data with a good agreement for relatively low velocities (99 % at 0 m/s and 96 % at 1.63 m/s). However, the error was up to 70 % at high airflow velocities (8.5 m/s and higher).
- The onset time of condensation is clearly delayed by the presence of a dust layer. Therefore, the assumption of a clear surface represents the worst case in modeling the novel PV/T-GSHEX system.

- The droplet growth increased (mainly due to coalescence) by almost 200 %, when the micro-dust layer increased from 0 to 56  $\mu\text{m}$  on the substrate surface. Subsequently, mud formation was enhanced. Therefore, the micro-dust layer's presence creates a significant efficiency barrier to any potential application (e.g. PV panels or solar thermal collectors). It is essential to prevent condensation and thus, mud formation, which was proven to be possible with the present system.

Thus, it can be concluded that the proposed PV/T-GSHEX system can be applied in harsh climatic regions. The PV/T-GSHEX system has a high potential to overcome diurnal overheating and nocturnal condensation (mud formation) issues. The system was successfully proven to operate effectively under a wide variety of weather conditions, dust loading and soil properties. In all cases, the diurnal PV cell temperature could be decreased efficiently and nocturnal dew formation could be prevented.

## 6.2 Outlook

Some experiments and numerical studies of high future interest couldn't be performed in the framework of the present project. Future work concerns a deeper analysis of different mechanisms, and a better understanding of an optimized thermal storage operation for the PV/T-GSHEX. Future interesting tasks can be summarized as follows:

- Outdoor experimental tests on the condensation phenomena for different types and ages of PV panels.
- Experimental investigation of the onset of condensation should be applied to real PV panel glass samples taken from a solar site with different operational ages. Such investigations could improve the current study to a more realistic level.
- More experiments on condensation and mud formation phenomena should be carried out to obtain a higher amount of experimental results.

These results could be used to obtain an empirical correlation for dew and mud formation, which could be included to develop a more comprehensive model of the proposed system.

- A controllable circulation pump with optimized control should be considered to further enhance the performance of the PV/T-GSHEX system. This would contribute to fully discharging the thermal storage in the night hours to provide colder storage temperatures for diurnal cooling and vice versa.
- An economic feasibility analysis of the PV/T-GSHEX system is of interest as a future study for system development.

# Bibliography

- [1] Dash, P. K.; Gupta, N.C. (2015). Effect of temperature on power output from different commercially available photovoltaic modules. *International Journal of Engineering Research and Applications*, 5(1), 148-151.
- [2] Komoto, K.; Ehara, T.; Xu, H.; Lv, F.; Wang, S.; Sinha, P.; Bogdanov, D. (2015). Energy from the desert: Very large scale PV power plants for shifting to renewable energy future. International Energy Agency, Paris, France.
- [3] Fouad, M. M.; Shihata, L. A.; Morgan, E. I. (2017). An integrated review of factors influencing the performance of photovoltaic panels. *Renewable and Sustainable Energy Reviews*, 80, 1499-1511.
- [4] Mustafa, R. J.; Gomaa, M. R.; Al-Dhaifallah, M.; Rezk, H. (2020). Environmental impacts on the performance of solar photovoltaic systems. *Sustainability*, 12(2), 608.
- [5] Eitner, U.; Kajari-Schröder, S.; Köntges, M.; Altenbach, H. (2011). Thermal stress and strain of solar cells in photovoltaic modules. In *Shell-like Structures*. Springer, Berlin, Heidelberg.
- [6] Cao, M.; Butler, S.; Benoit, J.T.; Jiang, Y.; Radhakrishnan, R.; Chen, Y. (2008). Thermal stress analysis/life prediction of concentrating photovoltaic module. *Journal of Solar Energy Engineering*, 130(2).
- [7] Heithorst, B.; Bauer, G.; Rauscher, B.; Irrgang, L.; Spinnler, M.; Sattelmayer, T. (2018). Experimental comparison of scroll and swash-plate compressors for PV driven compression chillers and heat pumps. In

- 12th International Conference on Solar Energy for Buildings and Industry.
- [8] <https://www.qnrf.org/en-us/>. Accessed 4<sup>th</sup> March 2017.
- [9] <https://www.noaa.gov/>. Accessed 5<sup>th</sup> November 2018.
- [10] Mittag, M.; Vogt, L.; Herzog, C.; Neuhaus, H. (2019). Thermal modelling of photovoltaic modules in operation and production. In 36th European Photovoltaic Solar Energy Conference and Exhibition (EUPVSEC).
- [11] Zaraket, J.; Khalil, T.; Aillerie, M.; Vokas, G. A.; Salame, C. (2017). The effect of electrical stress under temperature in the characteristics of PV solar modules. *Energy Procedia*, 119, 579-601.
- [12] Mostefaoui, M.; Ziane, A.; Bouraiou, A.; Khelifi, S. (2019). Effect of sand dust accumulation on photovoltaic performance in the Saharan environment: southern Algeria (Adrar). *Environmental Science and Pollution Research*, 26(1), 259-268.
- [13] Semaoui, S.; Arab, A. H.; Boudjelthia, E. K.; Bacha, S.; Zeraia, H. (2015). Dust effect on optical transmittance of photovoltaic module glazing in a desert region. *Energy Procedia*, 74, 1347-1357.
- [14] Wiesinger, F.; Sutter, F.; Fernández-García, A.; Wette, J.; Wolfertstetter, F.; Hanrieder, N.; Pitz-Paal, R. (2020). Sandstorm erosion on solar reflectors: Highly realistic modeling of artificial aging tests based on advanced site assessment. *Applied Energy*, 268, 114925.
- [15] Aïssa, B.; Isaifan, R. J.; Madhavan, V. E.; Abdallah, A. A. (2016). Structural and physical properties of the dust particles in Qatar and their influence on the PV panel performance. *Scientific Reports*, 6(1), 1-12.
- [16] Amelia, A. R.; Irwan, Y. M.; Leow, W. Z.; Irwanto, M.; Safwati, I.; Zhafarina, M. (2016). Investigation of the effect temperature on photovoltaic (PV) panel output performance. *International Journal on Advanced Science Engineering Information Technology*, 6(5), 682-688.
- [17] Ahmad, I.; Al-Hamadani, N.; Ibrahim, K. (1983). Solar radiation maps for Iraq. *Solar Energy*, 31(1), 29-44.

- [18] Sulaiman, S.; Hussain, H.; Leh, N.; Razali, M. S. (2011). Effects of dust on the performance of PV panels. *World Academy of Science, Engineering and Technology*, 58, 588-593.
- [19] Mani, M.; Pillai, R. (2010). Impact of dust on solar photovoltaic (PV) performance: Research status, challenges and recommendations. *Renewable and Sustainable Energy Reviews*, 14(9), 3124-3131.
- [20] Elminir, H.; Ghitas, A.; Hamid, R.; El-Hussainy, F.; Beheary, M.; Abdel-Moneim, K. (2006). Effect of dust on the transparent cover of solar collectors. *Energy Conversion and Management*, 47(18-19), 3192-3203.
- [21] Malizia, A.; Poggi, L.; Ciparisse, J.; Rossi, R.; Bellecci, C.; Gaudio, P. (2016). A review of dangerous dust in fusion reactors: from its creation to its resuspension in case of LOCA and LOVA. *Energies*, 9(8), 578.
- [22] Mekhilef, S.; Saidur, R.; Kamalisarvestani, M. (2012). Effect of dust, humidity and air velocity on efficiency of photovoltaic cells. *Renewable and Sustainable Energy Reviews*, 16(5), 2920-2925.
- [23] Goossens, D.; Van Kerschaever, E. (1999). Aeolian dust deposition on photovoltaic solar cells: The effects of wind velocity and airborne dust concentration on cell performance. *Solar Energy*, 66(4), 277-289.
- [24] Hegazy, A. A. (2001). Effect of dust accumulation on solar transmittance through glass covers of plate-type collectors. *Renewable Energy*, 22(4), 525-540.
- [25] Paudyal, B. R.; Shakya, S. R. (2016). Dust accumulation effects on efficiency of solar PV modules for off grid purpose: A case study of Kathmandu. *Solar Energy*, 135, 103-110.
- [26] Karmouch, R.; Hor, H. E. L. (2017). Solar cells performance reduction under the effect of dust in Jazan region. *Journal of Sustainable Energy*, 7(2), 1-4.
- [27] Maghami, M. R.; Hizam, H.; Gomes, C.; Radzi, M.; Rezadad, M.; Hajjhorbani, S. (2016). Power loss due to soiling on solar panel: A review. *Renewable and Sustainable Energy Reviews*, 59, 1307-1316.

- [28] Yilbas, B. S.; Ali, H.; Khaled, M.; Al-Aqeeli, N.; Abu-Dheir, N.; Varanasi, K. K. (2015). Influence of dust and mud on the optical, chemical and mechanical properties of a PV protective glass. *Scientific Reports*, 5(1), 1-12.
- [29] Hassan, G.; Yilbas, B.; Said, S.; Al-Aqeeli, N.; Matin, A. (2016). Chemo-mechanical characteristics of mud formed from environmental dust particles in humid ambient air. *Scientific Reports*, 6(1), 1-14.
- [30] Yilbas, B. S.; Hassan, G.; Ali, H.; Al-Aqeeli, N. (2017). Environmental dust effects on aluminum surfaces in humid air ambient. *Scientific Reports*, 7(1), 1-12.
- [31] Natarajan, S. K.; Mallick, T. K.; Katz, M.; Weingaertner, S. (2011). Numerical investigations of solar cell temperature for photovoltaic concentrator system with and without passive cooling arrangements. *International Journal of Thermal Sciences*, 50(12), 2514-2521.
- [32] Duffie, J. A.; Beckman, W. A.; Blair, N. (2020). *Solar engineering of thermal processes, photovoltaics and wind*. John Wiley and Sons.
- [33] Kalogirou, S. A. (2013). *Solar energy engineering: Processes and systems*. Academic press.
- [34] Moradi, K.; Ebadian, M. A.; Lin, C. X. (2013). A review of PV/T technologies: Effects of control parameters. *International Journal of Heat and Mass Transfer*, 64, 483-500.
- [35] Geoola, F.; Peiper, U. M. (1994). Outdoor testing of the condensation characteristics of plastic film covering materials using a model greenhouse. *Journal of Agricultural Engineering Research*, 57(3), 167-172.
- [36] El-Shobokshy, M. S.; Hussein, F. M. (1993). Effect of dust with different physical properties on the performance of photovoltaic cells. *Solar Energy*, 51(6), 505-511.
- [37] Guo, B.; Javed, W.; Figgis, B. W.; Mirza, T. (2015). Effect of dust and weather conditions on photovoltaic performance in Doha, Qatar. In

- 2015 First Workshop on Smart Grid and Renewable Energy (SGRE), IEEE, 1-6.
- [38] Figgis, B.; Nouviaire, A.; Wubulikasimu, Y.; Javed, W.; Guo, B.; Ait-Mokhtar, A.(2018). Investigation of factors affecting condensation on soiled PV modules. *Solar Energy*, 159, 488-500.
- [39] Dhimish, M.; Alrashidi, A. (2020). Photovoltaic degradation rate affected by different weather conditions: A case study based on PV systems in the UK and Australia. *Electronics*, 9(4), 650.
- [40] Dorobanțu, L.; Popescu, M. O.; Popescu, C. L.; Crăciunescu, A. (2013). Experimental assessment of PV panels front water cooling strategy. In *International Conference on Renewable Energies and Power Quality (ICREPQ'13) Bilbao (Spain)*, 20th to 22th March, 2172-038.
- [41] Bahaidarah, H.; Subhan, A.; Gandhidasan, P.; Rehman, S. (2013). Performance evaluation of a PV (photovoltaic) module by back surface water cooling for hot climatic conditions. *Energy*, 59, 445-453.
- [42] Courtesy of Winklmeier, J. [johannes.winklmaier@tum.de](mailto:johannes.winklmaier@tum.de).
- [43] Krauter, S. (2004). Increased electrical yield via water flow over the front of photovoltaic panels. *Solar Energy Materials and Solar Cells*, 82(1-2), 131-137.
- [44] Odeh, S.; Behnia, M. (2009). Improving photovoltaic module efficiency using water cooling. *Heat Transfer Engineering*, 30(6), 499-505.
- [45] Hosseini, R.; Hosseini, N.; Khorasanizadeh, H. (2011). An experimental study of combining a photovoltaic system with a heating system. In *World Renewable Energy Congress-Sweden Linköping (Sweden)*, (057), 2993-3000. Linköping University Electronic Press.
- [46] Abdolzadeh, M.; Ameri, M. (2009). Improving the effectiveness of a photovoltaic water pumping system by spraying water over the front of photovoltaic cells. *Renewable Energy*, 34(1), 91-96.

- [47] Moharram, K.; Abd-Elhady, M.; Kandil, H.; El-Sherif, H. (2013). Enhancing the performance of photovoltaic panels by water cooling. *Ain Shams Engineering Journal*, 4(4), 869-877.
- [48] Chen, H.; Chen, X.; Li, S.; Ding, H. (2014). Comparative study on the performance improvement of photovoltaic panel with passive cooling under natural ventilation. *International Journal of Smart Grid and Clean Energy*, 3(4), 374-379.
- [49] Maheshwari, G. P.; Mulla Ali, A. A. (2004). Comparative study between air-cooled and water-cooled condensers of the air-conditioning systems. *Energy Systems Laboratory*.
- [50] Bakker, M.; Zondag, H. A.; Elswijk, M. J.; Strootman, K. J.; Jong, M. J. M. (2005). Performance and costs of a roof-sized PV/thermal array combined with a ground coupled heat pump. *Solar Energy*, 78(2), 331-339.
- [51] Bakker, M.; Zondag, H. A.; Van Helden, W. G. J. (2002). Design of a dual flow photovoltaic/thermal combi panel. *Stan Ackermans Institute, IST World*, 617-620.
- [52] Cristofari, C.; Notton, G.; Canaletti, J. L. (2009). Thermal behavior of a copolymer PV/Th solar system in low flow rate conditions. *Solar Energy*, 83(8), 1123-1138.
- [53] Kroiß, A.; Spinnler, M.; Sattelmayer, T. (2010). Analysis of hybrid photovoltaic/thermal (PV/T) solar systems for small scale reverse osmosis desalination plants. In *25th European Photovoltaic Solar Energy Conference and Exhibition (PVSEC)*.
- [54] Sandnes, B.; Rekstad, J. (2002). A photovoltaic/thermal (PV/T) collector with a polymer absorber plate. Experimental study and analytical model. *Solar Energy*, 72(1), 63-73.
- [55] Tiwari, A.; Sodha, M. S. (2006). Performance evaluation of hybrid PV/thermal water/air heating system: A parametric study. *Renewable Energy*, 31(15), 2460-2474.

- [56] Kroiß, A.; Präbst, A.; Hamberger, S.; Spinnler, M.; Tripanagnostopoulos, Y.; Sattelmayer, T. (2014). Development of a seawater-proof hybrid photovoltaic/thermal (PV/T) solar collector. *Energy Procedia*, 52, 93-103.
- [57] Vokas, G.; Christandonis, N.; Skittides, F. (2006). Hybrid photovoltaic–thermal systems for domestic heating and cooling—a theoretical approach. *Solar Energy*, 80(5), 607-615.
- [58] Pieters, J. G.; Deltour, J. M.; Debruyckere, M. J. (1997). Light transmission through condensation on glass and polyethylene. *Agricultural and Forest Meteorology*, 85(1-2), 51-62.
- [59] Alonso-Abella, M.; Chenlo, F.; Nofuentes, G.; Torres-Ramírez, M. (2014). Analysis of spectral effects on the energy yield of different PV (photovoltaic) technologies: The case of four specific sites. *Energy*, 67, 435-443.
- [60] Graefe, J.; Sandmann, M. (2015). Shortwave radiation transfer through a plant canopy covered by single and double layers of plastic. *Agricultural and Forest Meteorology*, 201, 196-208.
- [61] Cemek, B.; Demir, Y. (2005). Testing of the condensation characteristics and light transmissions of different plastic film covering materials. *Polymer Testing*, 24(3), 284-289.
- [62] Pollet, I. V.; Pieters, J. G. (2000). Condensation and radiation transmittance of greenhouse cladding materials, part 3: Results for glass plates and plastic films. *Journal of Agricultural Engineering Research*, 77(4), 419-428.
- [63] Hegazy, A. A. (2001). Effect of dust accumulation on solar transmittance through glass covers of plate-type collectors. *Renewable Energy*, 22(4), 525-540.
- [64] Pollet, I. V.; Pieters, J. G. (2002). PAR transmittances of dry and condensate covered glass and plastic greenhouse cladding. *Agricultural and Forest Meteorology*, 110(4), 285-298.

- [65] Adinoyi, M. J.; Said, S. A. (2013). Effect of dust accumulation on the power outputs of solar photovoltaic modules. *Renewable Energy*, 60, 633-636.
- [66] Chen, J.; Pan, G.; Ouyang, J.; Ma, J.; Fu, L.; Zhang, L. (2020). Study on impacts of dust accumulation and rainfall on PV power reduction in East China. *Energy*, 194, 116915.
- [67] Ghosh, A. (2020). Soiling losses: A barrier for India's energy security dependency from photovoltaic power. *Challenges*, 11(1), 9.
- [68] Syafiq, A.; Pandey, A. K.; Adzman, N. N.; Abd Rahim, N. (2018). Advances in approaches and methods for self-cleaning of solar photovoltaic panels. *Solar Energy*, 162, 597-619.
- [69] Sarkın, A. S.; Ekren, N.; Sağlam, Ş. (2020). A review of anti-reflection and self-cleaning coatings on photovoltaic panels. *Solar Energy*, 199, 63-73.
- [70] Ferretti, N. (2016). PV module cleaning-market overview and basics. PI Photovoltaic-Institute Berlin AG.
- [71] Tiwari, S.; Rani, P.; Patel, R. N. (2019). Examining the economic viability of a solar panel dust cleaning. *International Conference on Electrical, Computer and Communication Technologies (ICECCT)*, IEEE, 1-9.
- [72] Kawamoto, H.; Kato, M. (2018). Electrostatic cleaning equipment for dust removal from solar panels of mega solar power generation plants. In *2018 IEEE 7th World Conference on Photovoltaic Energy Conversion (WCPEC)(A Joint Conference of 45th IEEE PVSC, 28th PVSEC 34th EU PVSEC)*, 3648-3652.
- [73] Kawamoto, H. (2019). Electrostatic cleaning equipment for dust removal from soiled solar panels. *Journal of Electrostatics*, 98, 11-16.
- [74] Alshehri, A.; Parrott, B.; Outa, A.; Amer, A. Abdellatif, F.; Trigui, H.; Taie, I. (2014). Dust mitigation in the desert: Cleaning mechanisms for solar panels in arid regions. In *2014 Saudi Arabia Smart Grid Conference (SASG)*, IEEE, 1-6.

- [75] Ferretti, N.; Ilse, K.; Sönmez, A.; Hagendorf, C.; Berghold, J. (2016). Investigation on the impact of module cleaning on the antireflection coating. 32nd European Photovoltaic Solar Energy Conference and Exhibition EU-PVSEC, 1697-1700.
- [76] Costa, S. C.; Diniz, A. S. A.; Kazmerski, L. L. (2018). Solar energy dust and soiling RD progress: Literature review update for 2016. *Renewable and Sustainable Energy Reviews*, 82, 2504-2536.
- [77] Vasiljev, P.; Borodinas, S.; Bareikis, R.; Struckas, A. (2013). Ultrasonic system for solar panel cleaning. *Sensors and Actuators A: Physical*, 200, 74-78.
- [78] He, G.; Zhou, C.; Li, Z. (2011). Review of self-cleaning method for solar cell array. *Procedia Engineering*, 16, 640-645.
- [79] Ahmed, S.; Li, Z.; Javed, M. S.; Ma, T. (2021). A review on the integration of radiative cooling and solar energy harvesting. *Materials Today Energy*, 21, 100776.
- [80] Sun, X.; Sun, Y.; Zhou, Z.; Alam, M. A.; Bermel, P. (2017). Radiative sky cooling: Fundamental physics, materials, structures, and applications. *Nanophotonics*, 6(5), 997-1015.
- [81] Hu, M.; Zhao, B.; Ao, X.; Ren, X.; Cao, J.; Wang, Q.; Pei, G. (2020). Performance assessment of a trifunctional system integrating solar PV, solar thermal, and radiative sky cooling. *Applied Energy*, 260, 114167.
- [82] Sun, X.; Silverman, T. J.; Zhou, Z.; Khan, M. R.; Bermel, P.; Alam, M. A. (2017). Optics-based approach to thermal management of photovoltaics: Selective-spectral and radiative cooling. *IEEE Journal of Photovoltaics*, 7(2), 566-574.
- [83] Paraskevadaki, E.; Papathanassiou, S.; Vokas, G. (2011). Effects of partial shading on the PV module characteristic curves. In *Materials Science Forum*, Trans Tech Publications Ltd, 670, 391-398.

- [84] Taylor, R. A.; Shoraka, Y.; Tehrani, S. S. M.; Nashed, A. (2018). Thermal energy storage for buildings: A merit order review. *Annual Review of Heat Transfer*, 21.
- [85] Guadalfajara, M.; Lozano, M. A.; Serra, L. M. (2014). Analysis of large thermal energy storage for solar district heating. In *Proceedings of the Eurotherm Seminar*, (Vol. 99).
- [86] Enescu, D.; Chicco, G.; Porumb, R.; Seritan, G. (2020). Thermal energy storage for grid applications: Current status and emerging trends. *Energies*, 13(2), 340.
- [87] Cabeza, L. F.; Oró, E. (2016). Thermal energy storage for renewable heating and cooling systems. In *Renewable Heating and Cooling*, Woodhead Publishing, 139-179.
- [88] Drijver, B.; Bakema, G.; Oerlemans, P. (2019). State of the art of HT-ATES in the Netherlands. In *Proceedings of the European Geothermal Congress*, The Hague, The Netherlands, 11-14.
- [89] Sarbu, I.; Sebarchievici, C. (2018). A comprehensive review of thermal energy storage. *Sustainability*, 10(1), 191.
- [90] Skarphagen, H.; Banks, D.; Frengstad, B. S.; Gether, H. (2019). Design considerations for borehole thermal energy storage (BTES): A review with emphasis on convective heat transfer. *Geofluids*.
- [91] Novo, A. V.; Bayon, J. R.; Castro-Fresno, D.; Rodriguez-Hernandez, J. (2010). Review of seasonal heat storage in large basins: Water tanks and gravel–water pits. *Applied Energy*, 87(2), 390-397.
- [92] Abd Elatty, A. S.; El-Nahhas, F. M.; El-Mossallamy, Y. M.; El-Baz, A. M. (2012). Effect of surrounding soil thermal conductivity on the effective pipe-to-borehole thermal resistance in vertical ground heat exchangers. In *International Engineering Conference on Design and Innovation in Infrastructure*, Jordan.

- [93] Sharqawy, M. H.; Mokheimer, E. M.; Badr, H. M. (2009). Effective pipe-to-borehole thermal resistance for vertical ground heat exchangers. *Geothermics*, 38(2), 271-277.
- [94] Vella, C.; Borg, S. P.; Micallef, D. (2020). The effect of shank-space on the thermal performance of shallow vertical U-tube ground heat exchangers. *Energies*, 13(3), 602.
- [95] Bortoloni, M.; Bottarelli, M. (2015). On the sizing of a flat-panel ground heat exchanger. *International Journal of Energy and Environmental Engineering*, 6(1), 55-63.
- [96] Paksoy, H. Ö. (Ed.). (2007). *Thermal energy storage for sustainable energy consumption: Fundamentals, case studies and design* (Vol. 234). Springer Science Business Media.
- [97] Børresen, M. H.; Barnes, D. L.; Rike, A. G. (2007). Repeated freeze–thaw cycles and their effects on mineralization of hexadecane and phenanthrene in cold climate soils. *Cold Regions Science and Technology*, 49(3), 215-225.
- [98] Li, H. J.; Yan, J. X.; Yue, X. F.; Wang, M. B. (2008). Significance of soil temperature and moisture for soil respiration in a Chinese mountain area. *Agricultural and Forest Meteorology*, 148(3), 490-503.
- [99] Said, S. A. M.; Habib, M. A.; Mokheimer, E. M. A.; Al-Shayea, N.; Sharqawi, M.; Arabia, D. S. (2009). Horizontal ground heat exchanger design for ground-coupled heat pumps. In *International Conference and Exhibition of Ecologic Vehicles and Renewable Energies*, Monaco.
- [100] Reda, M. N.; Spinnler, M.; Al-Kayiem, H.; Sattelmayer, T. (2019). Experimental investigation of temperature and condensation control of photovoltaic panels. *International Conference on Electrical and Electronics Engineering (ICEEE)*, 312-316.
- [101] Reda, M. N.; Spinnler, M.; AL-Kayiem, H. H.; Sattelmayer, T. (2021). Assessment of condensation and thermal control in a photovoltaic panel by PV/T and ground heat exchanger. *Solar Energy*, 221, 502-511.

- [102] Reda, M. N.; Spinnler, M.; AL-Kayiem, H. H.; Sattelmayer, T. (2020). Analysis of ground thermal control systems for solar photovoltaic performance enhancement. *WIT Transactions on Ecology and the Environment*, 246, 41-50.
- [103] Reda, M. N.; Spinnler, M.; Mahamud, R.; Sattelmayer, T. (2020). Analytical model of the soil temperature distribution based on weather data. In *Heat Transfer Summer Conference*, American Society of Mechanical Engineers, 83709, V001T04A006.
- [104] Wu, X.; Yao, Z.; Brüggemann, N.; Shen, Z. Y.; Wolf, B.; Dannenmann, M.; Butterbach-Bahl, K. (2010). Effects of soil moisture and temperature on CO<sub>2</sub> and CH<sub>4</sub> soil-atmosphere exchange of various land use/cover types in a semi-arid grassland in Inner Mongolia, China. *Soil Biology and Biochemistry*, 42(5), 773-787.
- [105] Xing, L.; Li, L.; Gong, J.; Ren, C.; Liu, J.; Chen, H. (2018). Daily soil temperatures predictions for various climates in United States using data-driven model. *Energy*, 160, 430-440.
- [106] Park, K.; Yang, H.; Lee, B. Y.; Kim, D. (2018). Development of shallow-depth soil temperature estimation model based on thermal response in permafrost area. *Applied Sciences*, 8(10), 1886.
- [107] Araghi, A.; Mousavi-Baygi, M.; Adamowski, J.; Martinez, C.; van der Ploeg, M. (2017). Forecasting soil temperature based on surface air temperature using a wavelet artificial neural network. *Meteorological Applications*, 24(4), 603-611.
- [108] Barman, D.; Kundu, D. K.; Pal, S.; Chakraborty, A. K.; Jha, A. K.; Mazumdar, S. P.; Bhattacharyya, P. (2017). Soil temperature prediction from air temperature for alluvial soils in lower Indo-Gangetic plain. *International Agrophysics*, 31(1).
- [109] Yang, Z.; Zhang, J.; Wu, L. (2019). Spring soil temperature as a predictor of summer heatwaves over northwestern China. *Atmospheric Science Letters*, 20(3), 887.

- [110] Brown, S. E.; Pregitzer, K. S.; Reed, D. D.; Burton, A. J. (2000). Predicting daily mean soil temperature from daily mean air temperature in four northern hardwood forest stands. *Forest Science*, 46(2), 297-301.
- [111] Xing, L.; Spittler, J. D. (2017). Prediction of undisturbed ground temperature using analytical and numerical modeling. Part I: Model development and experimental validation. *Science and Technology for the Built Environment*, 23(5), 787-808.
- [112] Kjellander, K. (2015). Two simple soil temperature models: Applied and tested on sites in Sweden. Department of Earth Sciences, Uppsala University ([www.geo.uu.se](http://www.geo.uu.se)).
- [113] Sándor, R.; Fodor, N. (2012). Simulation of soil temperature dynamics with models using different concepts. *The Scientific World Journal*.
- [114] Lei, S.; Daniels, J. L.; Bian, Z.; Wainaina, N. (2011). Improved soil temperature modeling. *Environmental Earth Sciences*, 62(6), 1123-1130.
- [115] Halama, J. J.; Barnhart, B. L.; Kennedy, R. E.; McKane, R. B.; Graham, J. J.; Pettus, P. P.; Waschmann, R. S. (2018). Improved soil temperature modeling using spatially explicit solar energy drivers. *Water*, 10(10), 1398.
- [116] Nobel, P. S.; Geller, G. N. (1987). Temperature modelling of wet and dry desert soils. *The Journal of Ecology*, 247-258.
- [117] Zheng, D.; Hunt Jr, E. R.; Running, S. W. (1993). A daily soil temperature model based on air temperature and precipitation for continental applications. *Climate Research*, 2(3), 183-191.
- [118] Sattari, M. T.; Dodangeh, E.; Abraham, J. (2017). Estimation of daily soil temperature via data mining techniques in semi-arid climate conditions. *Earth Sciences Research Journal*, 21(2), 85-93.
- [119] Rykaczewski, K.; Paxson, A. T.; Staymates, M.; Walker, M. L.; Sun, X.; Anand, S.; Varanasi, K. K. (2014). Dropwise condensation of low surface tension fluids on omniphobic surfaces. *Scientific Reports*, 4(1), 1-8.

- 
- [120] Herich, H.; Tritscher, T.; Wiacek, A.; Gysel, M.; Weingartner, E.; Lohmann, U.; Cziczo, D. J. (2009). Water uptake of clay and desert dust aerosol particles at sub and supersaturated water vapor conditions. *Physical Chemistry Chemical Physics*, 11(36), 7804-7809.
- [121] Tang, J.; Busnaina, A. A. (2000). The effect of time and humidity on particle adhesion and removal. *The Journal of Adhesion*, 74(1-4), 411-419.
- [122] Arsalan, N.; Palayangoda, S. S.; Burnett, D. J.; Buiting, J. J.; Nguyen, Q. P. (2013). Surface energy characterization of sandstone rocks. *Journal of Physics and Chemistry of Solids*, 74(8), 1069-1077.
- [123] Sjögren, N. O. (2007). Hygroscopic properties of organic and inorganic aerosols. Doctoral dissertation, ETH Zürich.
- [124] Kaaden, N.; Massling, A.; Schladitz, A.; Müller, T.; Kandler, K.; Schütz, L.; Wiedensohler, A. (2009). State of mixing, shape factor, number size distribution, and hygroscopic growth of the Saharan anthropogenic and mineral dust aerosol at Tinfou, Morocco. *Tellus B: Chemical and Physical Meteorology*, 61(1), 51-63.
- [125] Zelenyuk, A.; Imre, D.; Cuadra-Rodriguez, L. A.; Ellison, B. (2007). Measurements and interpretation of the effect of a soluble organic surfactant on the density, shape and water uptake of hygroscopic particles. *Journal of Aerosol Science*, 38(9), 903-923.
- [126] Ma, Q.; He, H.; Liu, Y.; Liu, C.; Grassian, V. H. (2013). Heterogeneous and multiphase formation pathways of gypsum in the atmosphere. *Physical Chemistry Chemical Physics*, 15(44), 19196-19204.
- [127] Niu, D.; Tang, G. H. (2016). The effect of surface wettability on water vapor condensation in nanoscale. *Scientific Reports*, 6(1), 1-6.
- [128] Bhardwaj, R.; Ten Kortenaar, M. V.; Mudde, R. F. (2013). Influence of condensation surface on solar distillation. *Desalination*, 326, 37-45.
- [129] Yu, E.; Kim, S. C.; Lee, H. J.; Oh, K. H.; Moon, M. W. (2015). Extreme wettability of nanostructured glass fabricated by non-lithographic, anisotropic etching. *Scientific Reports*, 5(1), 1-6.

- [130] Bandyopadhyay, K. (2018). Effects of roughness and wettability on condensation in presence of noncondensable gases. 10th International Conference on Boiling and Condensation Heat Transfer, Japan.
- [131] Leriche, M.; Roessner, W.; Weigand, B. (2015). Modelling of the condensation/evaporation of water droplets on a glass surface: Application to defogging. ASME-ATI-UIT 2015 Conference on Thermal Energy Systems: Production, Storage, Utilization and the Environment, Italy.
- [132] Rykaczewski, K. (2012). Microdroplet growth mechanism during water condensation on superhydrophobic surfaces. *Langmuir*, 28(20), 7720-7729.
- [133] Wang, Q.; Xie, H.; Hu, Z.; Liu, C. (2019). The impact of the electric field on surface condensation of water vapor: Insight from molecular dynamics simulation. *Nanomaterials*, 9(1), 64.
- [134] Croce, G.; D'Agaro, P.; De Angelis, A.; Mattiello, F. (2007). Numerical simulation of windshield defogging process. *Proceedings of the Institution of Mechanical Engineers, Part D: Journal of Automobile Engineering*, 221(10), 1241-1250.
- [135] Niu, D.; Tang, G. H. (2014). Static and dynamic behavior of water droplet on solid surfaces with pillar-type nanostructures from molecular dynamics simulation. *International Journal of Heat and Mass Transfer*, 79, 647-654.
- [136] Sokuler, M.; Auernhammer, G. K.; Roth, M.; Liu, C.; Bonaccorso, E.; Butt, H. J. (2010). The softer the better: Fast condensation on soft surfaces. *Langmuir*, 26(3), 1544-1547.
- [137] Leach, R. N.; Stevens, F.; Langford, S. C.; Dickinson, J. T. (2006). Dropwise condensation: Experiments and simulations of nucleation and growth of water drops in a cooling system. *Langmuir*, 22(21), 8864-8872.
- [138] Yin, Y. L.; Wang, R. Z.; Zhai, X. Q.; Ishugah, T. F. (2014). Experimental investigation on the heat transfer performance and water condensation phenomenon of radiant cooling panels. *Building and Environment*, 71, 15-23.

- [139] Klemm, A. J.; Klemm, P.; Ibrahim, I. (2007). Assessment of surface roughness for the analysis of the water vapour condensation process. *WIT Transactions on Engineering Sciences*, 57, 10.
- [140] Quéré, D. (2008). Wetting and roughness. *Annual Review of Materials Research*, 38, 71-99.
- [141] Wier, K. A.; McCarthy, T. J. (2006). Condensation on ultrahydrophobic surfaces and its effect on droplet mobility: Ultrahydrophobic surfaces are not always water repellent. *Langmuir*, 22(6), 2433-2436.
- [142] Howarter, J. A.; Youngblood, J. P. (2008). Self-cleaning and next generation anti-fog surfaces and coatings. *Macromolecular Rapid Communications*, 29(6), 455-466.
- [143] Toxvaerd, S. (2002). Molecular dynamics simulation of heterogeneous nucleation at a structureless solid surface. *The Journal of Chemical Physics*, 117(22), 10303-10310.
- [144] Croce, G.; D'Agaro, P.; Della Mora, F. (2004). Numerical simulation of glass fogging and defogging. In *CHT-04-advances in computational heat transfer III. Proceedings of the Third International Symposium*. Begel House Inc.
- [145] Solarland SLP100-12U silver poly solar panel data sheet (2017).
- [146] Abu-Hamdeh, N. H. (2003). Thermal properties of soils as affected by density and water content. *Biosystems Engineering*, 86(1), 97-102.
- [147] Dukhan, N.; Özdemir, M.; Kavurmacioğlu, L. (2016). Experimental fully-developed thermal convection for non-darcy water flow in metal foam. *Journal of Thermal Engineering*, 2(2), 82-677.
- [148] Petukhov, B. S. (1970). Heat transfer and friction in turbulent pipe flow with variable physical properties. In *Advances in Heat Transfer*, 6, 503-564.
- [149] Gnielinski, V. (2013). On heat transfer in tubes. *International Journal of Heat and Mass Transfer*, 63, 134-140.

- [150] Li, M.; Lai, A. C. (2013). Thermodynamic optimization of ground heat exchangers with single U-tube by entropy generation minimization method. *Energy Conversion and Management*, 65, 133-139.
- [151] Kalogirou, S. A. (2014). *Solar energy engineering*. Academic Press, 257-321.
- [152] Huang, S.; Ma, Z.; Cooper, P. (2014). Optimal design of vertical ground heat exchangers by using entropy generation minimization method and genetic algorithms. *Energy Conversion and Management*, 87, 128-137.
- [153] Oğulata, R. T.; Doba, F.; Yilmaz, T. (2000). Irreversibility analysis of cross flow heat exchangers. *Energy Conversion and Management*, 41(15), 1585-1599.
- [154] Xu, M.; Guo, J.; Li, X. (2014). Thermodynamic analysis and optimization design of heat exchanger. In *Advances in Transport Phenomena*, 63-167.
- [155] Cole, K.; Beck, J.; Haji-Sheikh, A.; Litkouhi, B. (2010). *Heat conduction using Greens functions*. CRC Press.
- [156] Duffie, J. A.; Beckman, W. A.; Worek, W. M. (2013). *Solar engineering of thermal processes*. John Wiley & Sons.
- [157] Fukuta, N.; Walter, L. (1970). Kinetics of hydrometeor growth from a vapor-spherical model. *Journal of Atmospheric Sciences*, 27(8), 1160-1172.
- [158] Al-Kayiem, H. H.; Aurybi, M. A.; Gilani, S. I. (2019). Influence of canopy condensate film on the performance of solar chimney power plant. *Renewable Energy*, 136, 1012-1021.
- [159] Kumar, S.; Chourasia, B. K.; Mullick, S. C. (2005). Wind heat transfer coefficient in flat plate solar collectors. *SESI Journal: Journal of the Solar Energy Society of India*, 15(2), 29.
- [160] Mihalakakou, G.; Santamouris, M.; Asimakopoulos, D. (1994). Modelling the thermal performance of earth-to-air heat exchangers. *Solar Energy*, 53(3), 301-305.

- [161] Badache, M.; Eslami-Nejad, P.; Ouzzane, M.; Aidoun, Z.; Lamarche, L. (2016). A new modeling approach for improved ground temperature profile determination. *Renewable Energy*, 85, 436-444.
- [162] Larwa, B.; Kupiec, K. (2019). Study of temperature distribution in the ground. *Chemical and Process Engineering*, 40(1), 123-137.
- [163] Cannon, J. R. (1984). *The one-dimensional heat equation*. Cambridge University Press.
- [164] Hwang, I.; Cheon, S.; Park, W. (2020). Consideration factors in application of thermocouple sensors for RCS temperature instrumentation. In *EPJ Web of Conferences* 225(03005). EDP Sciences.
- [165] Spinnler, M.; Sattelmayer, T. (2014). *Solar engineering. Lecture Script*.

# A Appendix

## Laboratory Measurement of Soil Moisture Content

This method covers the laboratory determination of the moisture content of a soil as a percentage of its oven-dried weight. The method may be applied to fine, medium and coarse grained soils. The soil has been tested in the soil test Lab (UTP, see Figure A.1).

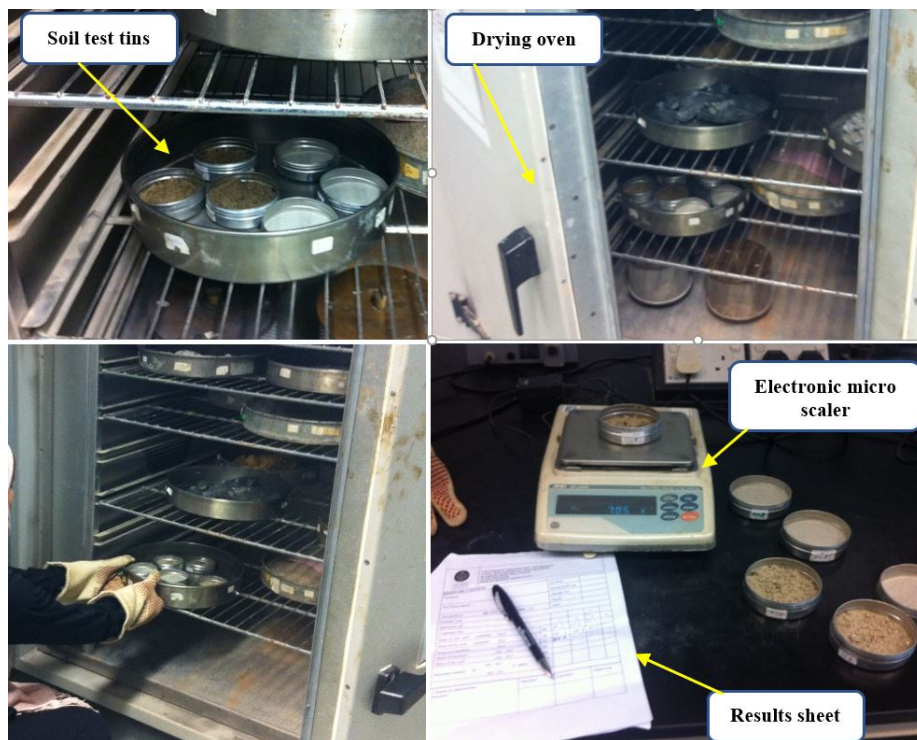


**Figure A.1:** Oven-drying method procedure in UTP/Civil engineering Lab.

The method is based on removing soil moisture by oven-drying a soil sample until the weight remains constant (110°C for a period of 24 hours).

The moisture content (%) is calculated from the sample weight before and after drying by using a micro gram scaler. The results are recorded in a sheet and then the moisture content ( $MC$ ) is calculated according to the following equation:

$$MC \% = \frac{W_2 - W_3}{W_3 - W_1} \times 100 \quad (\text{A.1})$$

Where:

$W_1$  = Weight of tin [g]

$W_2$  = Weight of moist soil + tin [g]

$W_3$  = Weight of dried soil + tin [g]

The physical properties recorded from the previous soil tests are shown in table 2.2.